Feasibility studies for accessing nucleon structure observables with the $\overline{\text{P}}$ANDA experiment at the future FAIR facility

Dissertation

zur Erlangung des Grades
"Doktor der Naturwissenschaften"

am Fachbereich Physik
der Johannes Gutenberg Universität
in Mainz

von
María Carmen Mora Espí
geboren in Valencia, Spanien

Mainz, October 2012

Abstract

The availability of a high-intensity antiproton beam with momentum up to 15 GeV/c at the future Facility for Antiproton and Ion Research (FAIR) will open a unique opportunity to investigate wide areas of nuclear physics with the $\overline{\text{P}}$ANDA (anti$\overline{\text{P}}$roton ANnihilations at DArmstadt) detector. Part of these investigations concern the electromagnetic form factors of the proton in the time-like region and the study of the transition distribution amplitudes, for which feasibility studies have been performed in this Thesis. Moreover, simulations to study the efficiency and the energy resolution of the backward endcap of the electromagnetic calorimeter of $\overline{\text{P}}$ANDA are presented. This detector is crucial especially for the reconstruction of processes like $\bar{p}p \to e^+e^-\pi^0$, investigated in this work. Different arrangements of dead material were studied. The results show that both, the efficiency and the energy resolution of the backward endcap of the electromagnetic calorimeter fullfill the requirements for the detection of backward particles, and that this detector is necessary for the reconstruction of the channels of interest.

The study of the annihilation channel $\bar{p}p \to e^+e^-$ will improve the knowledge of the electromagnetic form factors in the time-like region, and will help to understand their connection with the electromagnetic form factors in the space-like region. In this Thesis the feasibility of a measurement of the $\bar{p}p \to e^+e^-$ cross section with $\overline{\text{P}}$ANDA is studied using Monte-Carlo simulations. The major background channel $\bar{p}p \to \pi^+\pi^-$ is taken into account. The results show a 10^9 background suppression factor, which assure a sufficiently clean signal with less than 0.1% background contamination. The signal can be measured with an efficiency greater than 30% up to $s = 14\,(\text{GeV/c})^2$. The electromagnetic form factors are extracted from the reconstructed signal and corrected angular distribution. Above this s limit, the low cross section will not allow the direct extraction of the electromagnetic form factors. However, the total cross section can still be measured and an extraction of the electromagnetic form factors is possible considering certain assumptions on the ratio between the electric and magnetic contributions.

The transition distribution amplitudes are new non-perturbative objects describing the transition between a baryon and a meson. They are accessible in hard exclusive processes like $\bar{p}p \to e^+e^-\pi^0$. The study of this process with $\overline{\text{P}}$ANDA will test the transition distribution amplitudes approach. This work includes a feasibility study for measuring this channel with $\overline{\text{P}}$ANDA. The main background reaction is here $\bar{p}p \to \pi^+\pi^-\pi^0$. A background suppression factor of 10^8 has been achieved while keeping a signal efficiency above 20%.

Part of this work has been published in the European Physics Journal A 44, 373-384 (2010).

Zusammenfassung

Der hoch intensive Antiproton-Strahl mit einem Impuls von bis zu 15 GeV/c an der im Aufbau befindlichen Facility for Antiproton and Ion Research (FAIR), mit dem $\overline{\text{P}}$ANDA (anti$\overline{\text{P}}$roton ANnihilations at DArmstadt) Detektor, bietet eine einzigartige Möglichkeit weite Bereiche der Kernphysik zu studieren. Teil dieser Studien ist die Messung der elektromagnetischen Formfaktoren des Protons im zeitartigem Bereich sowie die der Transition-Distribution-Amplituden. Als Teil dieser Studien werden Simulationen präsentiert, mit denen die Effizienz und die Energieauflösung der Rückwärts-Endkappe des elektromagnetischen Kalorimeters von $\overline{\text{P}}$ANDA studiert werden. Dieser Detektor ist von großer Bedeutung bei der Rekonstruktion des Prozesses $\bar{p}p \rightarrow e^+e^-\pi^0$, der in dieser Arbeit untersucht wird. Es werden verschiedene Szenarien untersucht. Die Ergebnisse zeigen, dass die Eigenschaften der Rückwärts-Endkappe des elektromagnetischen Kalorimeters durch die zusätzliche Massenbelegung kaum leiden und Teilchen unter Rückwärtswinkeln gut detektiert werden können.

Die effiziente Messung des Prozesses $\bar{p}p \rightarrow e^+e^-$ wird dazu dienen, das Wissen über die elektromagnetischen Formfaktoren im zeitartigen Bereich empfindlich zu verbessern, und damit deren Verbindung zu den elektromagnetischen Formfaktoren im raumartigem Bereich besser zu verstehen. In dieser Arbeit wird, basierend auf Monte-Carlo Simulationen, die Durchführbarkeit der Messung $\bar{p}p \rightarrow e^+e^-$ mit $\overline{\text{P}}$ANDA untersucht. Hierbei wird der bei weitem schädlichste Untergrundprozess, $\bar{p}p \rightarrow \pi^+\pi^-$, berücksichtigt. Die Ergebnisse zeigen eine Unterdrückung des Untergrundes von der Ordnung 10^9. Damit kann ein sauberes Signal mit einer geringen Verunreinigung von weniger als 0.1% erreicht werden. Das Signal kann bis zu einen $s = 14$ (GeV/c)^2 mit einer Effizienz größer als 30% vom Untergrund sauber getrennt werden. Die elektromagnetischen Formfaktoren werden aus der rekonstruierten und korrigierten Winkelverteilung des Signals extrahiert. Oberhalb des genanten s-Bereichs wird die Anzahl der Ereignisse zu klein, um die elektromagnetischen Formfaktoren zu extrahieren. Sie können dennoch unter gewissen Annahmen über das Verhältnis zwischen elektrischen und magnetischen Beiträgen gemessen werden.

Die Transition-Distribution-Amplituden sind neue, nichtperturbative Objekte, welche zum Beispiel den Übergang von einem Baryon zu einem Meson beschreiben und hilfreich für die Berechnung von Wirkungsquerschnitten harter exklusiver Prozesse sind. Durch das Studium des Prozesses $\bar{p}p \rightarrow e^+e^-\pi^0$ mit $\overline{\text{P}}$ANDA wird die Anwendbarkeit des Transition-Distribution-Amplituden Ansatzes überprüft. Diese Arbeit enthält eine Durchführbarkeitsstudie zur Messung von $\bar{p}p \rightarrow e^+e^-\pi^0$ mit $\overline{\text{P}}$ANDA. Als gravierendster Untergrundsprozess wurde $\bar{p}p \rightarrow \pi^+\pi^-\pi^0$ untersucht. Eine Unterdrückung des Untergrundes von 10^8 sowie eine Signaleffizienz von 20% wurden erreicht.

Teile dieser Arbeit wurden in European Physics Journal A. 44, 373-384 (2010) veröffentlicht.

"Nous cojón el vaso así..."
¡Ay!, perdón, perdón, perdón,
pido humildemente perdón,
he dicho una barbaridad.
He dicho "así" y se dice "icí" o "com ça"

Tip y Coll, "Cómo llenar un vaso de agua"

Contents

1

Introduction

The present work has been developed in the framework of the $\overline{\mathsf{P}}$ANDA (anti$\overline{\mathsf{P}}$roton ANnihilations at DArmstadt) collaboration that will use the new research Facility for Antiproton and Ion Research (FAIR) facilities at GSI in Darmstadt.

The main object of study in this work is the proton. The proton is known to be a non-point-like particle formed by three quarks bound together by the strong force. The proton structure can be studied via different experiments giving access to different observables and nucleon structure quantities depending on the energy regime in which we are measuring. The present work combines detector performance studies with investigations on two of such nucleon structure observables: the electromagnetic form factors (EMFF) of the proton in the time-like domain of positive $4-$momentum transfer and the transition distribution amplitudes (TDA).

The EMFF in the space-like domain are directly correlated to the charge and magnetic distribution of the proton. They have been very useful in understanding the proton structure. On the other side, only few measurements in the time-like region have been done employing the processes $\bar{p}p \to e^+e^-$ or $e^+e^- \to \bar{p}p$ [1, 2]. The statistics reached in these experiments do not permit a separation of the EMFF. Therefore, the EMFF in the time-like region are not very well known. A better understanding of the EMFF in the time-like region is needed to understand their behavior in the space-like region.

The TDA describe the transition between a baryon and a meson. They are new non-perturbative objects that can be accessed in hard exclusive cross sections [3].

The $\overline{\text{P}}$ANDA experiment will be a modern, high energy physics detector with full angular coverage, very good energy resolution, efficiency and particle identification (PID) capabilities [4]. $\overline{\text{P}}$ANDA will allow the measurement of the proton EMFF in the time-like region with an unprecedented accuracy via the process $\bar{p}p \rightarrow e^+e^-$. The validity of the TDA approach will also be checked.

The backward endcap of the electromagnetic calorimeter (BWEMC) will be a very important sub-detector of $\overline{\text{P}}$ANDA for the measurement of low energy particles (mainly photons and electrons) emitted at backward angles. It will be crucial for the measurement of the reaction $\bar{p}p \rightarrow e^+e^-\pi^0$. The energy resolution and the efficiency of this detector are required to be sufficient for the identification and reconstruction of the reactions of interest.

In this Thesis the feasibility of the measurements $\bar{p}p \rightarrow e^+e^-$ and $\bar{p}p \rightarrow e^+e^-\pi^0$ has been studied. The energy resolution and efficiency of the BWEMC have also been studied due to their importance in the reconstruction of these channels.

After this short introduction, Chapter 2 gives the theoretical framework of this work. The EMFF are defined and different techniques to measure them are described. Existing data are also shown. A short introduction to the TDA is exposed and the way they will be confirmed with $\overline{\text{P}}$ANDA is explained.

Chapter 3 describes the $\overline{\text{P}}$ANDA detector. A short introduction of the FAIR facilities is presented together with an overview of the research that will be done with $\overline{\text{P}}$ANDA. Finally the whole experimental setup of the detector is laid out [4].

Chapter 4 gives an overview of the software used for the simulations and the main structure of the analysis procedures. The event generators have been developed with EvtGen including radiative corrections like emission of photons in the final state. The physics processes have been simulated using the GEANT4 transport code. The whole analysis and reconstruction software has been developed using C++ [4].

Chapter 5 shows the study of the energy resolution and efficiency of the BWEMC. These simulations show the influence of the dead material introduced by the mechanical support systems and cabling of other inner sub-detectors of $\overline{\text{P}}$ANDA on the BWEMC. The achieved results show that BWEMC will have an energy resolution and an efficiency sufficient for the reconstruction of the reactions of interest, and therefore the construction of this detector as a part of the whole $\overline{\text{P}}$ANDA setup is mandatory.

Chapter 6 presents the analysis of the simulations of the feasibility of measuring $\bar{p}p \rightarrow e^+e^-$ [5]. First of all the achieved background suppression factor is calculated and presented. The signal reconstruction efficiency has been calculated using high statistics simulations at different energies. These results have

been used for the correction of the reconstructed signal. Finally the EMFF ratio was extracted from a fit to the angular distribution.

Chapter 7 discusses the feasibility studies for the measurement of $\bar{p}p \to e^+e^-\pi^0$. Expected rates are calculated and the assumptions for the simulation of the background are presented. Later the background contamination fraction is calculated and the method to extract the signal from our measured events sample is explicated. The cross section is calculated from the number of corrected events.

Finally, Chapter 8 summarizes the results, the conclusion, and the outlook.

2

Theoretical framework

2.1 The building blocks of matter

The building blocks of matter as it surrounds us, are the nucleons (protons and neutrons in the atomic nuclei) and electrons (around them). The electrons are postulated as point-like particles, and no experiment so far is inconsistent with this theoretical axiom. However, the experiments have shown that the nucleons are not point-like particles, they have a structure. The discovery of the existence of quarks as elementary particles and underlying building blocks forming the nucleon and the knowledge of the forces of nature (electromagnetic, strong and weak) gave rise to the development of the Standard Model. The Standard Model describes the interaction among the fundamental particles. According to this, matter is composed of quarks (up, down, strange, charm, bottom and top) and leptons (electrons, muons, taus and their corresponding neutrinos ν_e, ν_μ and ν_τ), classified in three families. The quarks can interact via the strong, the electromagnetic and the weak forces. All of them are part of the Standard Model. The electrons, muons and taus can feel both the electromagnetic and the weak forces but the neutrinos can only interact via the weak force. The three forces are carried via the gauge bosons. The strong force is carried by eight gluons, the electromagnetic force is carried by the photon and the weak force is carried by the $W^\pm$ and Z^0 bosons. These particles complete the set of particles in the Standard Model. Quantum electrodinamics (QED), describing the electromagnetic force, and the theory of the weak interaction are well understood and are applied in all energy ranges. Quantum chromodynamics (QCD) as the relativistic quantum field theory of strong interaction can at present not be used in the low energy regime. The strong coupling constant increases at low energies giving rise to problems in the calculations: perturbation theory doesn't work for these
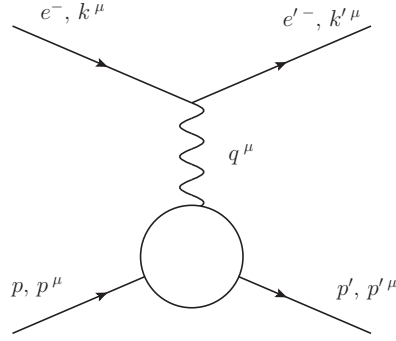
Figure 2.1: Lowest-order electron-proton elastic scattering diagram.

energies. The understanding of the strong force at low energies on the other hand can be tested by measurements of hadron structure observables. The stable hadrons in nature are the proton and also the neutron when it is part of an atomic nucleus. Understanding the nucleon structure in the low energy regime has been, and it is still, a main topic in nuclear physics experiments. The $\overline{\text{P}}$ANDA detector and its dedicated physics program will contribute to extend the knowledge of the nucleon structure and of the strong force in the time-like region.

2.2 Electromagnetic form factors in the space-like region

The proton's anomalous magnetic moment was first measured by Stern and collaborators in 1933 [6], who found a value about 2.8 times larger than what was expected for a spin$-\frac{1}{2}$ Dirac particle. The proton, therefore could not be point-like.

Today, a common way to study the proton structure is through the reactions $e^- p \to e^- p$, $e^+ e^- \to \bar{p}p$ and $\bar{p}p \to e^+ e^-$.

The electron scattering reaction is described in Figure 2.1. There the $4-$momenta of the initial and final electrons are represented by k^μ and k'^μ respectively, the $4-$momenta of the initial and final protons are p^μ and p'^μ, and the transferred momentum between both particles is $q^\mu = (k'^\mu - k^\mu)$.

In the space-like region, defined by the interchange of a photon with negative $4-$momentum squared, $q^2 < 0$, the elastic proton structure can be disentangled using electron scattering experiments off protons. We can redefine q^2 as $Q^2 = -q^2$ so that in space-like region $Q^2 > 0$. The cross section of the scattering process

$$e^- p \to e^- p \tag{2.1}$$

can be measured and compared to the well-known cross section for scattering of spin $\frac{1}{2}$-particles without structure.

The electron vertex can be described exactly using QED in leading order perturbation theory. The interaction occurs through the exchange of one virtual photon $\gamma^\star$ with $4-$momentum squared q^2. The unknown nucleon structure is contained in the proton vertex. In this approximation, called the Born approximation, a simple formalism relates the cross section with the electromagnetic form factors (EMFF).

The cross section for Reaction (2.1) can be calculated from the Feynman diagram in Figure 2.1. The electron vertex can be exactly described using QED as

$$j^\mu = -e\,\bar{u}(k'^{\,\mu})\,\gamma^\mu\,u(k^\mu)e^{i(k'^{\,\mu}-k^\mu)\cdot x^\mu}. \tag{2.2}$$

The unknown nucleon structure is contained in the hadron vertex

$$J^\mu = e\,\bar{u}(p'^{\,\mu})\,\Gamma^\mu\,u(p^\mu)e^{i(p'^{\,\mu}-p^\mu)\cdot x^\mu}. \tag{2.3}$$

In Formulas (2.2) and (2.3), j^μ is the lepton current density, J^μ is the hadronic current density, u and $\bar{u}$ are the column and row spinors describing the incoming and outgoing electrons of momenta k^μ and $k'^{\,\mu}$, and the initial and final protons of momenta p^μ and $p'^{\,\mu}$, γ^μ is the Dirac matrix and the Γ^μ matrix represents the hadron structure. The most general Lorentz-invariant form for Γ^μ includes a Dirac-γ^μ and a Pauli-$\sigma^{\mu\nu}q_\nu$ term

$$\Gamma^\mu = \left[F_1(Q^2)\,\gamma^\mu + \frac{1}{2M_p}F_2(Q^2)\,i\sigma^{\mu\nu}q_\nu\right]. \tag{2.4}$$

Here F_1 and F_2 represent the Pauli and Dirac EMFF respectively and M_p is the proton mass. The Formula (2.4) together with Equation (2.3) relate the hadron current with the EMFF. There F_1 and F_2. F_1 and F_2 are two independent real functions of Q^2.

2.2.1 Pauli and Dirac form factors

In their first experimental papers [7–9] Hofstadter and coworkers used the following expression of the unpolarized cross section in the laboratory system in terms of F_1 and F_2

$$\left.\frac{d\sigma}{d\Omega}\right|_{lab} = \left(\frac{\alpha^2}{4E^2\sin^4\frac{\theta}{2}}\right)\frac{E'}{E}\quad\left[\left(F_1^2 - \frac{q^2}{4M_p^2}F_2^2\right)\cos^2\frac{\theta}{2}\right.$$
$$\left. - \frac{q^2}{2M_p^2}\left(F_1 + F_2\right)^2\sin^2\frac{\theta}{2}\right], \tag{2.5}$$

in which α is the electromagnetic coupling constant, θ is the electron scattering angle, and E and E' are the initial and final electron energies.

They generalized the concept of "effective" charge and magnetic moment by associating F_1 and F_2 with the deviation from a point-like charge (Dirac form factor) and the deviation from a point-like magnetic moment (Pauli form factor) respectively.

The Pauli and Dirac form factors, F_1 and F_2, are already defined at the level of the hadronic current. Therefore they can be calculated by any models which describe nucleon structure. On the other hand they appear in the expression of the cross section and therefore they can be directly measured.

2.2.2 Sachs form factors

Later on, Sachs introduced the electric G_E and the magnetic G_M form factors [10] which are linear combinations of the Pauli and Dirac form factors

$$G_E = F_1 - \tau F_2, \text{ and } G_M = F_1 + F_2. \tag{2.6}$$

where $\tau = \frac{Q^2}{4M_p^2}$ is a kinematic parameter depending only on Q^2. Using the Sachs form factors, the cross section in Equation (2.5) can be rewritten in a simpler form, without an interference term

$$\frac{d\sigma}{d\Omega_{lab}} = \sigma_M \left[2\tau G_M^2 \tan^2 \frac{\theta}{2} + \frac{G_E^2 + \tau G_M^2}{1 + \tau} \right]. \tag{2.7}$$

The term

$$\sigma_M = \frac{4\alpha^2}{(Q^2)^2} \frac{E'^3}{E} \cos^2 \frac{\theta}{2} \tag{2.8}$$

is the Mott cross section for relativistic scattering of electrons on point-like hadrons.

The Sachs form factors parametrize the internal charge and magnetization currents in the proton. Non-relativistically and also relativistically in the Breit reference frame, they can be interpreted as the Fourier transforms of the spatial distributions of the charge and magnetic moment densities, ρ_{ch} and ρ_{mag} respectively, [11]

$$G_E(q^2) = \int \rho_{ch}(\vec{r}) e^{-i\vec{q}\vec{r}} d^3\vec{r}, \tag{2.9}$$

$$G_M(q^2) = \mu_{(p,n)} \int \rho_{mag}(\vec{r}) e^{-i\vec{q}\vec{r}} d^3\vec{r} \tag{2.10}$$

At $Q^2 = 0$, the form factors take the values of the static charge and static magnetic moment of the proton (neutron), $G_E = 1 (0)$ and $G_M = \mu_p = 2.79$ ($\mu_n = -1.91$).

2.2.3 Rosenbluth separation experiments

The Rosenbluth separation technique [12], described in the following, is a method that allows one to measure G_E and G_M independently.

One can rewrite Equation (2.7) as

$$\frac{d\sigma}{d\Omega} = \left(\frac{d\sigma}{d\Omega}\right)_{Mott} \times \frac{1}{1+\tau}\left[G_E^2 + \frac{\tau}{\varepsilon}G_M^2\right], \tag{2.11}$$

where $\varepsilon = \left[1 + 2\left(1+\tau\right)\tan^2\frac{\theta}{2}\right]^{-1}$ is the virtual photon polarization. By measuring the cross section at different scattering angles but fixed Q^2 one can access the electric and magnetic form factors using electron scattering.

To disentangle G_E and G_M one defines the reduced cross section as

$$\left(\frac{d\sigma}{d\Omega}\right)_{red} = \frac{\frac{\varepsilon(1+\tau)}{\tau}\left(\frac{d\sigma}{d\Omega}\right)_{exp}}{\left(\frac{d\sigma}{d\Omega}\right)_{Mott}} = G_M^2 + \frac{\varepsilon}{\tau}G_E^2. \tag{2.12}$$

This allows one to extract the form factors, taking advantage of the linear dependence on ε. A linear fit to the reduced cross section, at the same Q^2 but for a range of different ε-values, *i.e.* different scattering angles, gives $\frac{1}{\tau}G_E^2$ as the slope and G_M^2 as the intercept.

Since the very first measurements of the EMFF, their dependence on Q^2 suggested a dipole structure of the form

$$G_D(Q^2) = \frac{1}{(1 + \frac{Q^2}{\Lambda_D^2})^2}, \tag{2.13}$$

with $\Lambda_D = 0.84\,\text{GeV}$ being a universal parameter. This corresponds to an exponential charge distribution. The dipole behavior is consistent with measurements for both G_E and G_M at the 10% level for $Q^2 \leq 2\,(\text{GeV/c})^2$ [28].

Assuming the dipole model, we have

$$G_E = G_D, \; G_M = \mu G_D, \; \text{and} \; G_M = \mu G_E \tag{2.14}$$

and therefore, the ratio $\mathcal{R} = 1$.

In Figure 2.2 one can see the results of various measurements of the EMFF in the space-like region using the Rosenbluth separation method. Both, G_E and G_M are shown normalized to the dipole form factor in order to get rid of the steep Q^2 dependence.

2.2.4 Polarization transfer experiments

The polarization method was suggested in 1967 by A. I. Akhiezer and M. P. Rekalo [29, 30]. Using a longitudinally polarized electron beam, the ratio
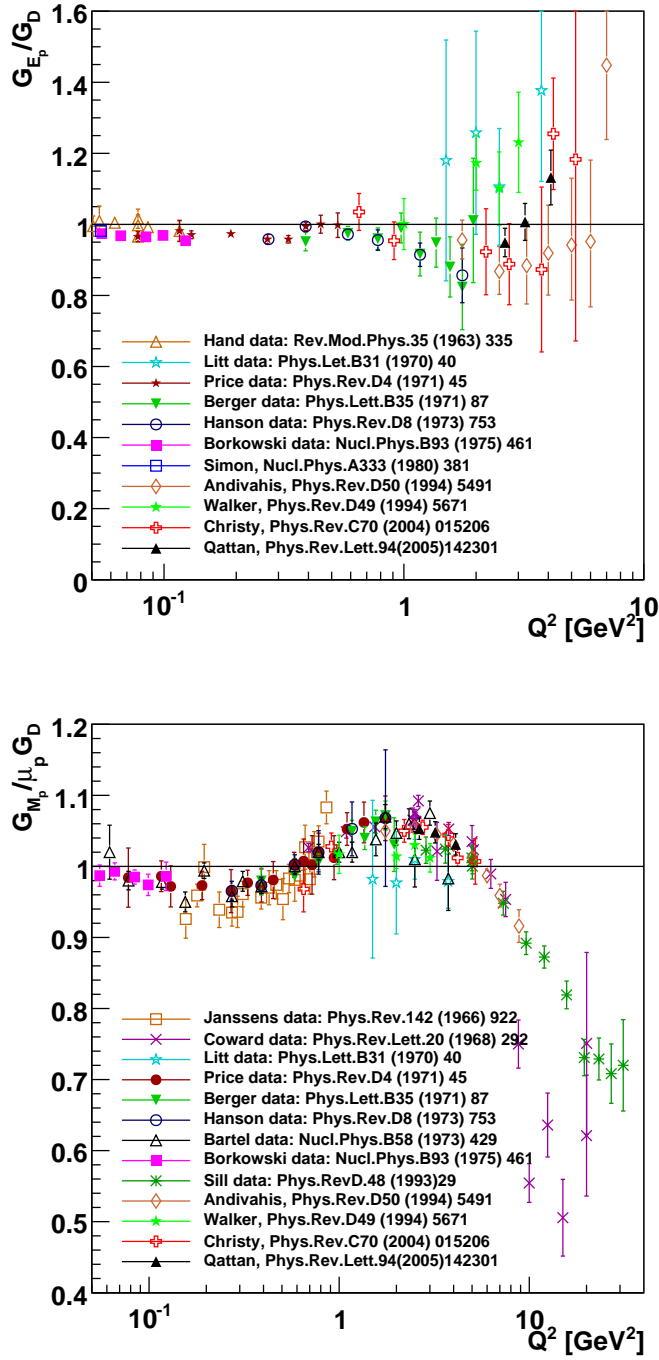
Figure 2.2: Results for G_E and G_M obtained by the Rosenbluth separation method. The values are normalized to the dipole form. The data have been taken from References [13–27] and replotted all together.

between the longitudinal, P_L, and transverse, P_T, polarization of the outgoing proton with respect to the momentum transfer direction is proportional to the ratio between G_E and G_M,

$$\frac{P_L}{P_T} \propto \frac{G_E}{G_M}.$$ (2.15)

This type of experiment could be realized only recently because it was necessary to have a highly polarized electron beam with high intensity and high energy, and to be able to measure the polarization of a proton with momentum in the GeV range. By measuring a ratio, one expects higher precision because some systematic errors cancel. The surprising result was a significant deviation of the ratio $\mathcal{R}$ from unity. Figure 2.3 shows data obtained at JLab using the polarization transfer method [31, 32] in comparison with results from the Rosenbluth separation method [26, 27, 33]. The discrepancy between the results of both methods can be clearly observed in the plot.

A possible explanation for the discrepancy between the results extracted from Rosenbluth separation and the recoil polarization measurements is connected with the exchange of two photons during the interaction [34]. The first calculations of the effects of the two photon exchange are shown in References [35, 36] , and later in References [37, 38]. Among the two photon exchange effect, also missing higher order radiative corrections to the unpolarized cross section have been advocated, but this corrections cancel to first order in the polarization ratios [39].

2.3 Electromagnetic form factors in the time-like region

Figure 2.4 shows the Feynman diagram for the annihilation of protons into electrons, which is intimately correlated by crossing symmetry with the diagram in Figure 2.1. Here the transferred momentum q^2 corresponds to the total energy available in the center of mass reference frame, s. In the space-like region, the transferred momentum is defined as

$$q^2 = (k^\mu - k'^\mu)^2 = (p^\mu - p'^\mu)^2.$$ (2.16)

By crossing symmetry the values of the $4-$momenta in the space-like region would be

$$\begin{aligned}
p, \, p^\mu &\rightarrow \, p, \, p_p^\mu, & (2.17) \\
p', p'^\mu &\rightarrow \, \bar{p}, \, -p_{\bar{p}}^\mu, & (2.18) \\
e'^-, \, k'^\mu &\rightarrow \, e^-, \, k_{e^-}^\mu, & (2.19) \\
e^-, \, k^\mu &\rightarrow \, e^+, \, -k_{e^+}^\mu, & (2.20)
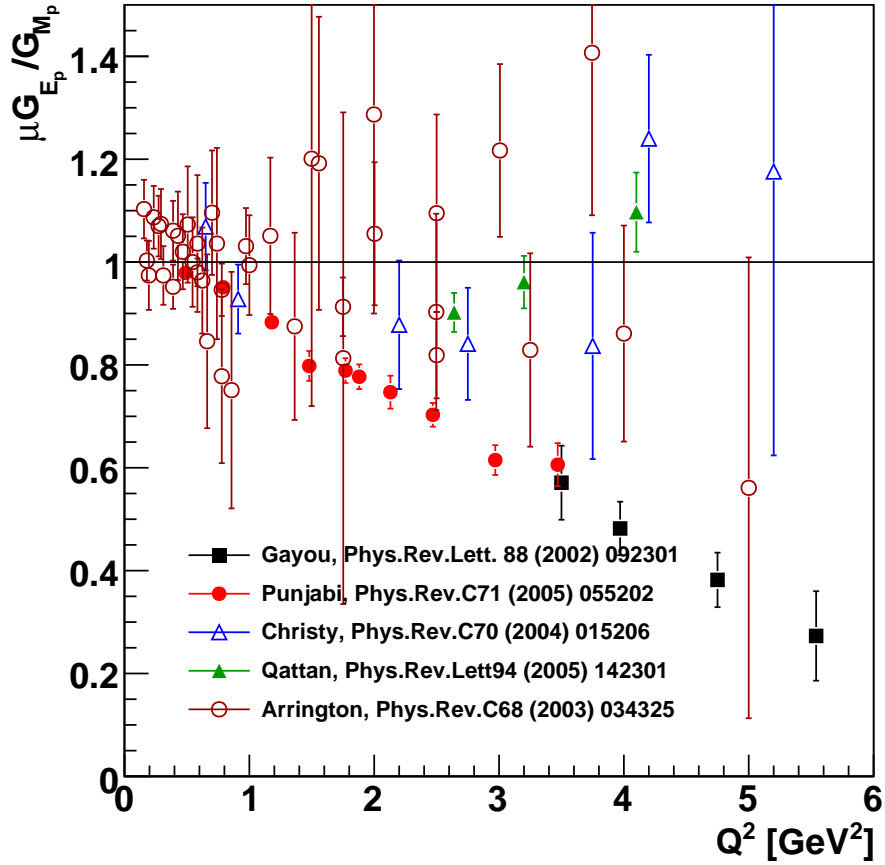\end{aligned}$$

Figure 2.3: Ratio between G_E and G_M using polarization transfer experiments (full circles and squares) [31, 32], compared with the results from Rosenbluth separation experiments. Open and full triangles are JLab Rosenbluth results [26, 27] and the rest of open symbols are other world date compiled in Reference [33]. The data have been taken from the original papers and replotted.
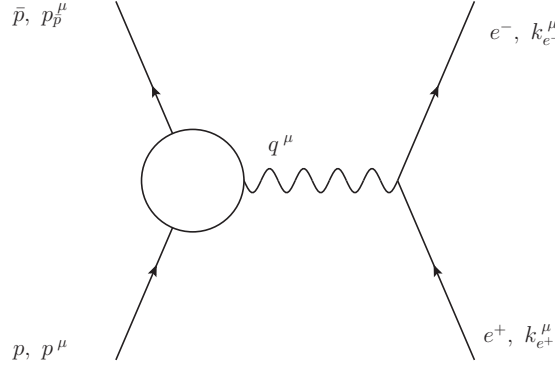
Figure 2.4: Annihilation of protons into an electron-positron pair. It corresponds to the crossed symmetry process of electron-proton elastic scattering

and therefore

$$s = q^2 = (p_p^\mu + p_{\bar{p}}^\mu)^2.$$ (2.21)

The value of q^2 in the time-like region will be always positive.

The matrix element for the annihilation process is

$$\Gamma^\mu = \left[F_1(Q^2)\gamma^\mu - \frac{1}{2M_p}F_2(Q^2)\,i\sigma^{\mu\nu}q_\nu \right].$$ (2.22)

The definitions of the Sachs form factors also hold in the time-like region. Here the EMFF are complex functions of q^2 and their correlation with the charge and magnetic densities inside the nucleon is not straight-forward. Nevertheless, the unpolarized cross section, and assuming one photon exchange depends only on the absolute values of G_E and G_M,

$$\frac{d\sigma}{d\cos\theta} = \frac{\pi\alpha^2}{8M^2\tau\sqrt{\tau(\tau-1)}}\left[\tau|G_M|^2(1+\cos^2\theta) + |G_E|^2\sin^2\theta\right],$$ (2.23)

where θ is the electron production angle in the center of mass system with respect to the direction of the $\bar{p}p$ pair (see Figure 2.5).

The EMFF in the time-like region ($q^2 > 0$) have been measured with poor statistics above $q^2 = 5\,\mathrm{GeV}^2$. They can be accessed via annihilation processes like

$$e^+e^- \to \bar{p}p$$ (2.24)

or

$$\bar{p}p \to e^+e^-$$ (2.25)

However, they can not be accessed for values of the $q^2 < 4\cdot M_p^2$, due to the energy threshold fixed by the proton mass, M_p. In Figure 2.6 one can see
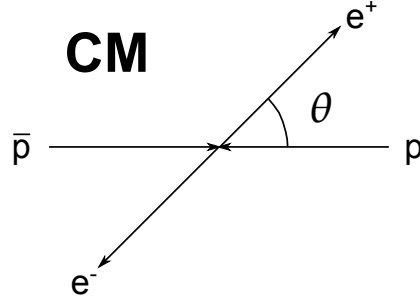
Figure 2.5: Definition of θ angle in $\bar{p}p \to e^+e^-$ annihilation process.

a summary of the definitions of the space-like and time-like regions and which parts of them are accessible with electron scattering or annihilation experiments.

This differential cross section was first obtained by Zichichi and collaborators in 1962 [40].

In the time-like region the separation of G_E and G_M is from the experimental point of view less sensitive to the normalization than in the space-like region, because they can be extracted directly by fitting an angular distribution to the differential cross section at fixed total energy squared $s = q^2$. In the space-like region at least two measurements at different angles but fixed q^2 are required for the traditional Rosenbluth separation. For this both the beam energy and the detection angle have to be changed in the experimental setup.

The cross section in Equation (2.23) is intimately related to the Rosenbluth formula by crossing symmetry. The even dependence on $\cos^2\theta$ is a consequence of the one-photon exchange formalism [41].

2.3.1 Polarization observables

The availability of polarized beams and targets permits also the access to the phase between the electric and magnetic form factors. The first expression including polarization observables in terms of the EMFF was given in Reference [42]. In this paper, they propose the measurement of the integral asymmetries $A_{0;\perp}(\vartheta, \phi)$ and $A_{\perp;\parallel}(\vartheta, \phi)$, defined as

$$A_{0;\perp} = \frac{\frac{4M}{\pi\sqrt{q^2}}|G_E||G_M|\sin\chi}{2|G_M|^2 + \frac{4M^2}{q^2}|G_E|^2}, \tag{2.26}$$
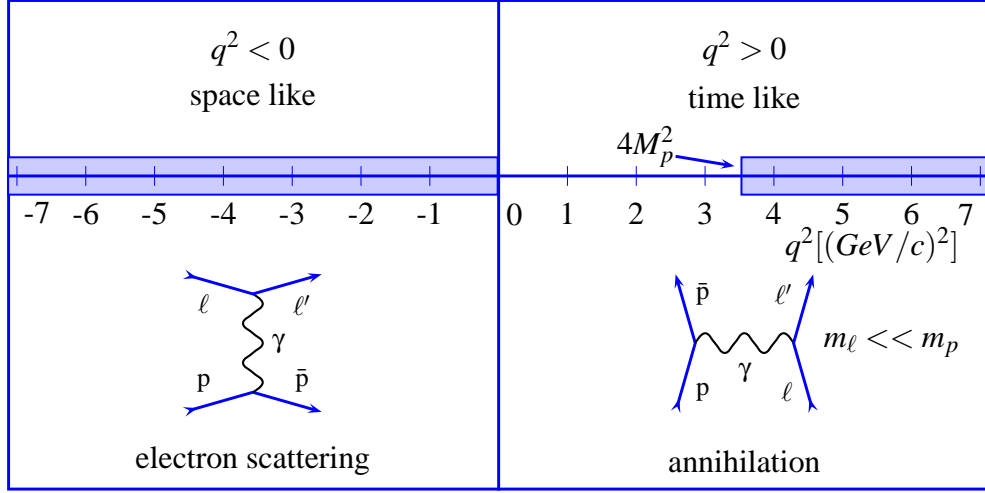
Figure 2.6: Space-like and time-like regions. The space-like region is defined for values of $q^2 < 0$, and the EMFF can be accessed via electron scattering experiments. The time-like region is defined for values of $q^2 > 0$, and the EMFF can be accessed via annihilation experiments starting from the threshold $q^2 = 4M_p^2$. The region between $q^2 = 0$ and $q^2 < 4M_p^2$ is called unphysical region and can be accessed via reactions like $\bar{p}p \to e^+e^-\pi^0$.

measurable with an unpolarized antiproton beam and a transversely polarized proton target, and

$$A_{\perp;\parallel} = \frac{\frac{4M}{\pi\sqrt{q^2}}|G_E||G_M|\cos\chi}{2|G_M|^2 + \frac{4M^2}{q^2}|G_E|^2}, \qquad (2.27)$$

measurable with a perpendicularly polarized antiproton beam and a longitudinally polarized proton target. The phase difference between the form factors, $\chi = \chi_M - \chi_E$, is then directly correlated with the integral asymmetries by

$$\tan\chi = -\frac{A_{0;\perp}}{A_{\perp;\parallel}}. \qquad (2.28)$$

In the framework of two-photon exchange all expressions of the observables for $\bar{p}p \to e^+e^-$ were derived in Reference [43] and for $e^+e^- \to \bar{p}p$ in Reference [44].

2.3.2 Necessity of a luminosity measurement

The measurement of the luminosity is crucial to connect the angular distribution with the cross section via

$$\frac{d\sigma}{d\cos\theta} = \frac{1}{\mathcal{L}}\frac{d^2N}{dtd\cos\theta}, \qquad (2.29)$$

and therefore important for the separation of the EMFF in the time-like region. In the cases in which a luminosity measurement is not possible the extraction of the ratio, $\mathcal{R} = \frac{|G_E|}{|G_M|}$, between the EMFF is still possible fitting the angular distribution to

$$N(\cos\theta) = A\left[\tau(1+\cos^2\theta) + \mathcal{R}^2\sin^2\theta\right], \tag{2.30}$$

where A is a normalization parameter related to the luminosity.

Due to low statistics, the unpolarized data available so far in time-like region do not permit the separation of the electric and the magnetic form factors with a fit to the cross sections of Reactions (2.24) and (2.25). In these cases the EMFF have been extracted under the assumptions $|G_E| = |G_M|$ or $|G_E| = 0$ from the measurement of the integrated cross section. The second assumption is completely arbitrary and the first one is strictly valid only at threshold ($q^2 = 4M_p^2$). There are no theoretical constraints why the first assumption should hold for $q^2 > 4M_p^2$. The difficulty of availability of polarized antiproton beams has also limited the measurement of polarized observables. The knowledge of the EMFF in the time-like region is currently very poor and the measured relative errors are about the 50% level while for the the space-like region the amount of available data is greater and the errors are of the order of 4-5%.

Figure 2.7 shows the extracted magnetic form factor $|G_M|$ in the time-like region as a function of the transferred momentum q^2. The data points have been extracted under the assumption of $|G_E| = |G_M|$.

In Chapter 6 in this Thesis it is shown using simulations for the determination of the EMFF that $\overline{\text{P}}$ANDA will allow to extend the EMFF data set with high precision measurements up to $q^2 \lesssim 14\,\text{GeV/c}^2$.

2.3.3 Differential cross section and counting rate for the simulation of the process $\bar{p}p \to e^+e^-$

The differential cross section for the annihilation process

$$\bar{p}p \to e^+e^-, \tag{2.31}$$

is given by Equation (2.23)

The total cross section is:

$$\sigma = \frac{\pi\alpha_e^2}{6M^2\tau\sqrt{\tau(\tau-1)}}\left(2\tau|G_M|^2 + |G_E|^2\right). \tag{2.32}$$

Evaluations of cross sections and counting rates require a knowledge of the EMFF. For the numerical estimates below, we use a parametrization of $|G_M|$
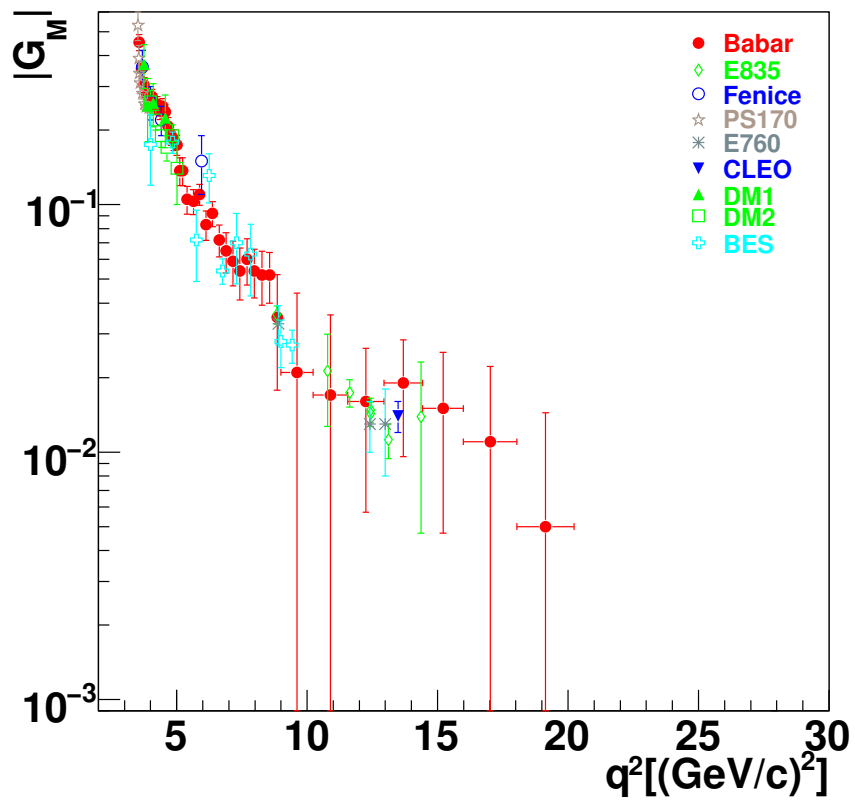
Figure 2.7: World data on the $|G_M|$ form factor, as extracted from the measured integrated annihilation cross section assuming $|G_E| = |G_M|$ [5].
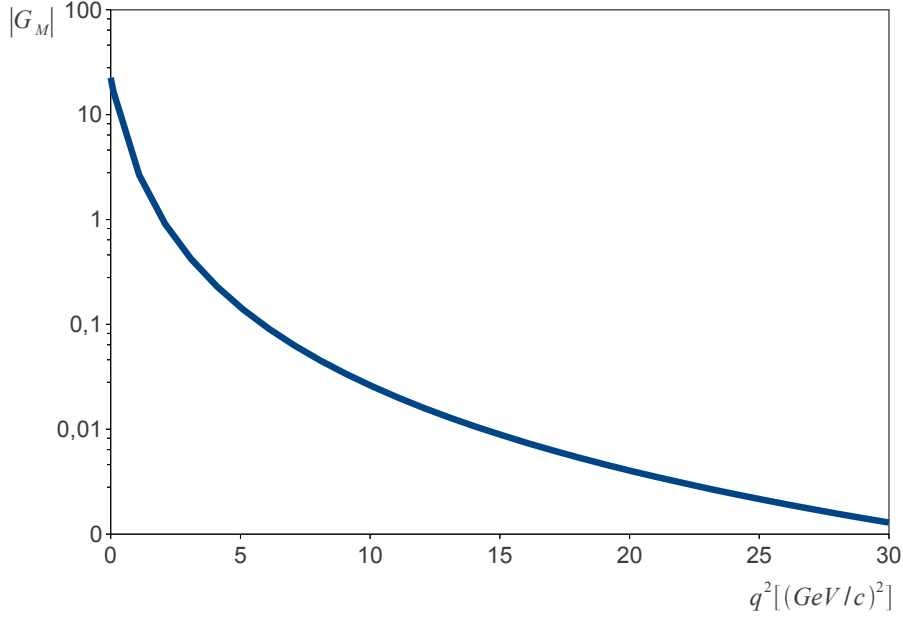
Figure 2.8: Parametrization of $|G_M|$: plot of Formula (2.33).

from [45],

$$|G_M| = 22.5 \left(1 + \frac{q^2}{0.71 \left[(\text{GeV/c})^2 \right]} \right)^{-2} \left(1 + \frac{q^2}{3.6 \left[(\text{GeV/c})^2 \right]} \right)^{-1}, \quad (2.33)$$

where the numerators are constants fitted on time-like data. Equation (2.33) gives a conservative estimate of the yield at large q^2. Figure 2.8 shows a plot of this parametrization of $|G_E|$.

As the time-like $|G_M|$ values have been extracted from cross section measurements assuming $|G_E| = |G_M|$, the same hypothesis is taken for counting rate estimates using Equation (2.32). Evaluations of cross sections and counting rates have also been performed using a QCD inspired parametrization based on an analytical extension of the dipole formula of Equation (2.13) to the time-like region, where Q^2 is replaced by q^2. Corrections based on dispersion relations have been suggested in Reference [46],

$$|G_{E,M}^{QCD}| = \frac{\mathcal{D}}{s^2 \left[\log^2(s/\Lambda^2) + \pi^2 \right]}, \quad \mathcal{D} = 89.45 \, [\text{GeV/c}]^4. \quad (2.34)$$

In Equation (2.34), $\mathcal{D}$ is obtained fitting the experimental data and $\Lambda = 0.3$ GeV is the QCD scale parameter. The calculated cross sections $\sigma(\sigma_{QCD})$ and number of counts $N(N_{QCD})$ are given in Table 2.1, assuming an integrated luminosity of

$\mathcal{L} = 2\,\text{fb}^{-1}$, which is expected for each data point in four months of data taking, with 100% efficiency and full acceptance[1]. It is assumed that $|G_E| = |G_M|$. The numbers are calculated from Equations (2.33) and (2.34), respectively.

s [GeV/c]^2	p [GeV/c]	σ [pb]	N	σ_{QCD} [pb]	N_{QCD}
5.40	1.7	538	$1.1 \cdot 10^6$	481	$9.6 \cdot 10^5$
7.27	2.8	72	$1.4 \cdot 10^5$	69	$1.4 \cdot 10^5$
8.21	3.3	32	$6.4 \cdot 10^4$	33	$6.5 \cdot 10^4$
11.0	4.9	4.52	$9.1 \cdot 10^3$	5.48	$1.1 \cdot 10^4$
12.9	5.9	1.60	$3.2 \cdot 10^3$	2.00	$4.3 \cdot 10^3$
13.8	6.4	1.00	$2.0 \cdot 10^3$	1.40	$2.8 \cdot 10^3$
16.7	7.9	0.29	580	0.49	979
22.3	10.9	0.04	81	0.09	183
27.9	13.4	0.01	18	0.03	51

Table 2.1: Cross section σ (σ_{QCD}) and number of counts, N (N_{QCD}) from Equation (2.33) (Equation (2.34)) corresponding to an integrated luminosity of $\mathcal{L} = 2\,\text{fb}^{-1}$, for different values of $q^2 = s$ and of the antiproton momentum, p.

2.3.3.1 Event generator for $\bar{p}p \to e^+e^-$

The event generator for the reaction in Equation (2.31) is based on the angular distributions from Equation (2.23), using Equation (2.33) for $|G_M|$.

Three different hypotheses were taken for $|G_E|$. Besides the case $|G_E| = |G_M|$, ($\mathcal{R} = 1$), which is strictly valid only at threshold, the case $\mathcal{R} = 0$ and the case $\mathcal{R} = 3$ (as suggested in Reference [47]), were also considered. The corresponding angular distributions were built keeping the same total cross section at the same q^2. These distributions are shown in Figure 2.9, for $q^2 = 5.4, 8.2, 13.8\,(\text{GeV/c})^2$. The reported error bars are statistical only. The sensitivity to $\mathcal{R}$ decreases with increasing q^2, due to the falling cross section and the relative weight of the magnetic term, which grows with q^2 as indicated in Figure 2.10. This Figure shows the calculated total cross section (blue solid line) under the assumption $|G_E| = |G_M|$. One can easily see that the contribution of the magnetic term to the total cross section (blue dotted-line) is much bigger than the electric contribution (red dash-dotted-line). The contribution of the second decreases strongly with q^2.

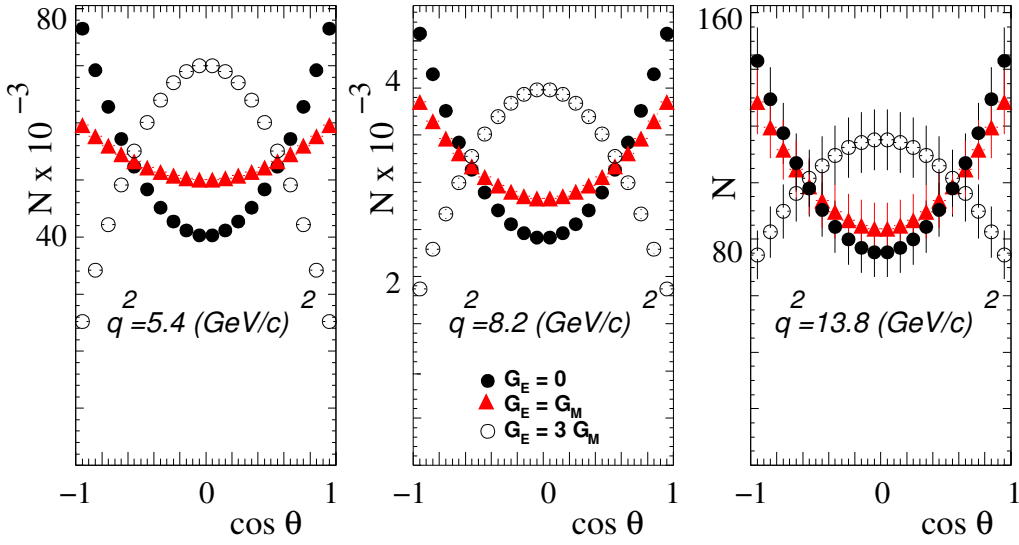[1]This value will be always used below, except when explicitly indicated.

Figure 2.9: Angular distributions in center of mass from the $\bar{p}p \to e^+e^-$ event generator, at $q^2 = 5.4$, 8.2, and 13.8 $(\text{GeV/c})^2$, and three different hypothesis: $\mathcal{R} = 0$ (black solid circles), $\mathcal{R} = 1$ (red triangles), and $\mathcal{R} = 3$ (black open circles), keeping the same value of the total cross section.

First order radiative corrections were taken into account in the simulations by using the package PHOTOS [51].

2.3.4 Study of background channels to $\bar{p}p \to e^+e^-$

Reactions involving two or more hadrons in the final state constitute an important background to the measurement of lepton pairs.

Due to the compactness, the good angular coverage and the good tracking resolution of the $\overline{\text{P}}$ANDA detector (see Chapter 3) channels with three or more hadrons in the final state will be very efficiently identified. The cross section for channels involving three pions is known to be at most one order of magnitude larger than two pion production. A reasonable cut on the missing mass in events with two observed particles should give a rejection factor of at least a factor of hundred for 3π final states.

The larger background is then expected to come from $\bar{p}p \to \pi^0\pi^0$, $\bar{p}p \to \pi^+\pi^-$ or $\bar{p}p \to K^+K^-$. The cross section for the neutral (charged) hadron pair production is about five (six) orders of magnitude larger than for the reaction in Equation (2.31). For $\pi^0\pi^0$ production, e^+e^- pairs are produced from π^0 decay photons, in particular in the beam pipe before the tracking system. In addition Dalitz decay, $\pi^0 \to e^+e^-\gamma$, with a probability of 10^{-2} can also produce e^+e^- pairs.
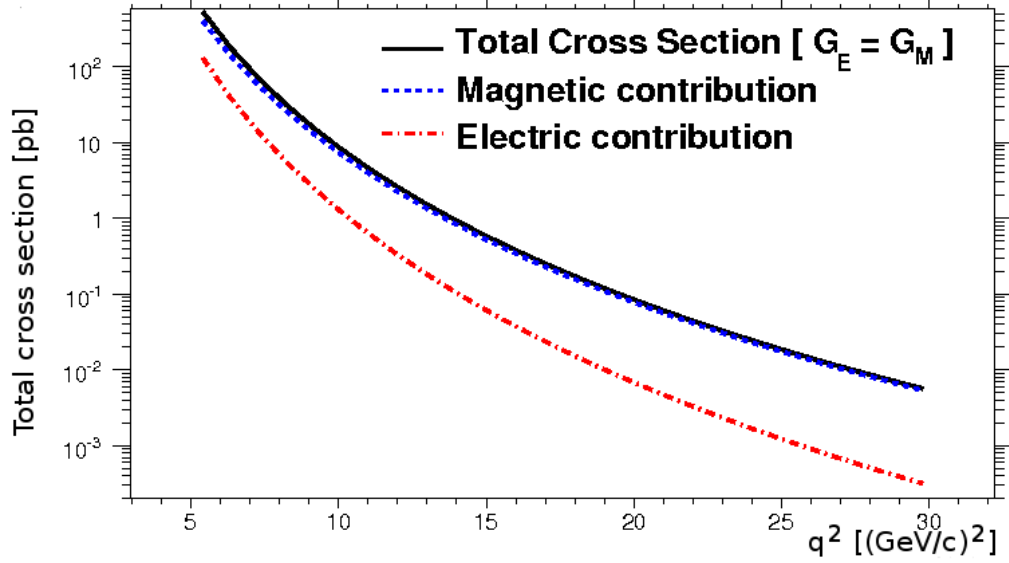
Figure 2.10: Contribution of G_E and G_M terms to the $\bar{p}p \to e^+e^-$ total cross section as a function of q^2 based on Equation (2.32).

For charged hadron pair production, both hadrons can be misidentified as leptons. For kaon production, the probability of misidentification is lower and the kinematic constraints are more efficient, due to the larger kaon mass. Therefore, this channel has not been considered for simulation and analysis.

The largest background to the reaction in Equation (2.31) comes then from $\bar{p}p$ annihilation into two charged or neutral pions. Detailed simulations have been dedicated to the two-pion case.

2.3.4.1 Simulations of $\bar{p}p \to \pi^+\pi^-$ and $\bar{p}p \to \pi^0\pi^0$ reactions

The angular distributions for charged and neutral pion pair production were extrapolated from a parametrization of the data in References [48–50, 52–54]. For $s < 6\,(\mathrm{GeV/c})^2$, the existing data in References [48, 52, 53] were fitted by Legendre polynomials. For larger s the behavior of exclusive processes is driven by dimensional counting rules, thus the differential cross section of the $\bar{p}p \to \pi^+\pi^-$ process can be parametrized as [55, 56]

$$\frac{d\sigma}{dt} = Cs^{-8}f(\theta) \tag{2.35}$$

where θ is the center of mass angle of the π^-, t is the Mandelstam variable and the function $f(\theta)$ depends on the reaction mechanism. In the framework of the quark interchange dominance model [57],

$$f(\theta) = \frac{1}{2}(1-z^2)[2(1-z)^{-2} + (1+z)^{-2}]^2, \; z = \cos\theta. \tag{2.36}$$

21

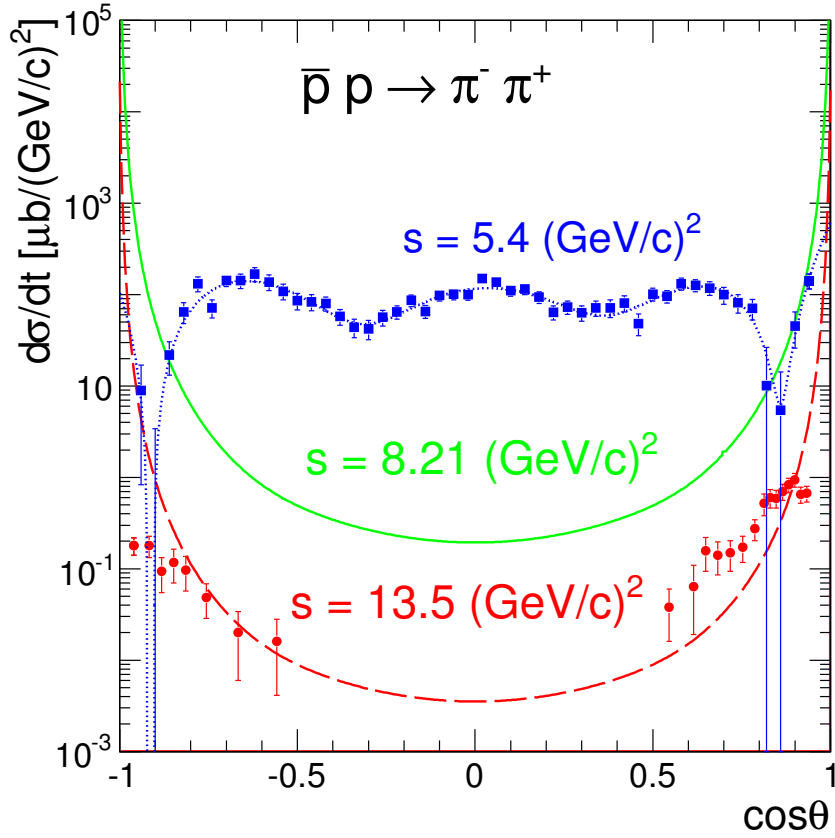**Figure 2.11:** Angular distributions in center of mass used to simulate the $\bar{p}p \to \pi^+\pi^-$ reaction for $s = 5.4\,(\text{GeV/c})^2$ (blue dotted line) for $s = 8.21\,(\text{GeV/c})^2$ (green solid line) and $s = 13.5\,(\text{GeV/c})^2$ (red dashed line) as a function of the cosine of the π^- production angle. Data are from Reference [48] (squares) and from References [49,50] (circles).
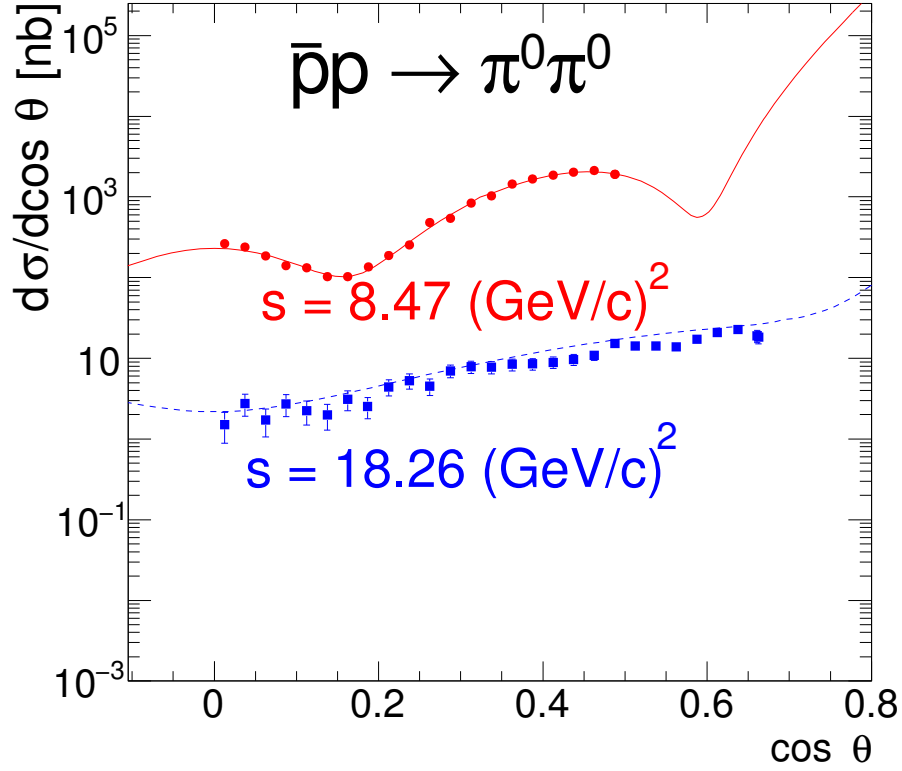
Figure 2.12: Angular distribution of pions produced in $\bar{p}p \to \pi^0\pi^0$ annihilation, for $s = 8.47\,(\text{GeV/c})^2$ (red circles) and $s = 18.26\,(\text{GeV/c})^2$ (blue squares). Data are from Reference [54].

$C = 440\,\text{mb}\,(\text{GeV/c})^{14}$ is a constant, which can not be currently predicted by QCD, and it is determined from $\pi^+ p$ elastic scattering at momentum $10\,\text{GeV/c}$ and $\cos\theta = 0$. The model predictions were symmetrized $(d\sigma(\theta)/dt \to [d\sigma(\theta)/dt + d\sigma(\pi - \theta)/dt]/2)$ and readjusted in the region around $90°$ at each s value to get a better agreement with the data. The results of the event generator are shown in Figure 2.11 for $s = 5.4\,(\text{GeV/c})^2$, $s = 8.21\,(\text{GeV/c})^2$ and $s = 13.5\,(\text{GeV/c})^2$ and compared to data obtained in References [48–50].

For exclusive $\pi^0\pi^0$ production at high energy the following parametrization was taken

$$\frac{d\sigma}{d\cos\theta} = \frac{f(s,\theta)}{s^6(\sqrt{tu}/s)^4}, \ f(s,\theta) = \sum_i a_i(s)P_i(\cos\theta) \qquad (2.37)$$

where $P_i(\cos\theta)$ are Legendre polynomials fitted to the data from the experiment E760 at Fermilab, in the kinematic range $(8.5 < s < 18.3)\,\text{GeV/c}$ [54], as shown in Figure 2.12. The quality of the fits can be seen in Figure 2.12, where two examples of differential cross sections for $\bar{p}p \to \pi^0\pi^0$ are shown.

For both reactions, the extrapolation to $|\cos\theta| = 1$ is affected by a large uncertainty, as no data exist at high energy. Therefore, in the following, only the angular region $|\cos\theta| \leq 0.8$ will be considered, in particular for the evaluation of statistical and systematic errors[2]. In this region, the ratio of $\pi^+\pi^-$ to e^+e^- cross sections varies from 10^5 at $|\cos\theta| = 0$ to $3 \cdot 10^6$ at $|\cos\theta| = 0.8$. On the basis of these numbers, the background rejection should be larger than $3 \cdot 10^9$ ($3 \cdot 10^8$) for $\pi^+\pi^-$ ($\pi^0\pi^0$) in this angular range to limit the background to the 0.1% level.

2.4 Transition distribution amplitudes: the reaction $\bar{p}p \rightarrow e^+e^-\pi^0$

The transition distribution amplitudes (TDA) [3] are new universal non-perturbative objects describing the transition between two different particles. They are an extension of the concept of general parton distributions (GPD) [58], which contain information about nucleon structure. The proton-to-meson TDA are defined from the Fourier transform of a matrix element of a three-quark-light-cone local operator [59]

$$\hat{O}_{\rho\tau\chi}^{\alpha\beta\gamma}(z_1, z_2, z_3) = \varepsilon_{c_1 c_2 c_3} \left. \Psi_\rho^{c_1 \alpha}(z_1)\Psi_\tau^{c_2 \beta}(z_2)\Psi_\chi^{c_3 \gamma}(z_3)\right|_{z_i^2 = 0}, \qquad (2.38)$$

between a proton and a meson state. Here α, β, and γ stand for quark flavor indices, ρ, τ, and χ denote the Dirac indices and $c_{1,2,3}$ are indices of the color group.

The TDA can be used to calculate the cross section of hard exclusive processes. Leading-twist amplitudes can be factorized in a perturbatively calculable process at quark level convoluted with the non-perturbative object which are the TDA.

Due to this non-perturbative character, the TDA can not yet be calculated ab initio. Therefore models had to be constructed. There exist models that describe baryonic TDA [60] in terms of spectral functions known as quadruple distributions, using chiral symmetry and the extension of soft pion theorems for πN TDA as a boundary condition. One may also construct a simple resonance exchange model for πN TDA considering N and $\Delta(1232)$ exchange contributions. A reasonable two-component model [61] contains both a factorized ansatz for quadruple distributions with input from the soft pion theorem and a contribution from the nucleon exchange in the u-channel of the reaction.

The experimental way of testing the validity of the TDA approach is to measure the cross section for hard exclusive processes and compare the exper-

---

[2]Note that the electron identification efficiency also becomes very low above $|\cos\theta| = 0.8$.

imental results with the values given by the calculations done using the TDA model.

2.4.1 Cross section of $\bar{p}p \to e^+e^-\pi^0$ at small momentum transfer

The cross section for $\bar{p}p \to e^+e^-\pi^0$ has been calculated in [62] using the TDA approach for small values of the momentum transfer t and large total energy W, which corresponds to a center-of-mass angle of the pion $\theta^*_{\pi^0}$ close to zero.

Figure 2.13 shows the factorization of the process $\bar{p}p \to \gamma^\star\pi$ into antiproton distribution amplitudes (DA), the hard sub-process amplitude (M_h) and the $p \to \pi$ TDA.
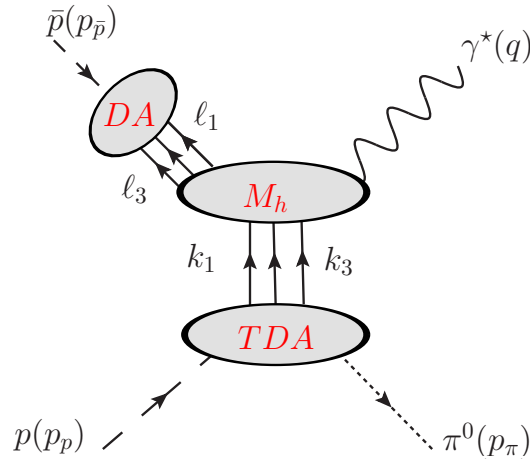

Figure 2.13: Factorization of $\bar{p}p \to \pi^0\gamma^\star \to \pi^0 e^+e^-$ using the TDA approach.

All the calculations have been done for $\Delta_{T_{\pi^0}} = 0$ (see Figure 2.14), $M_p \ll W$ and $m_\pi = 0$, where $\Delta_{T_{\pi^0}}$ is the transverse momentum of the π^0 in the center of mass system, M_p is the proton mass and m_π is the pion mass.

The main Formulas in Reference [62] which needed to calculate the cross section of this process are

$$\frac{d\sigma}{dt\,dq^2\,d\cos\theta_\ell} = \frac{\int d\varphi_\ell \left|\overline{\mathcal{M}^{\bar{p}p\to\ell^+\ell^-\pi^0}}\right|^2}{64W^2(W^2-4M_p^2)(2\pi)^2}, \tag{2.39}$$
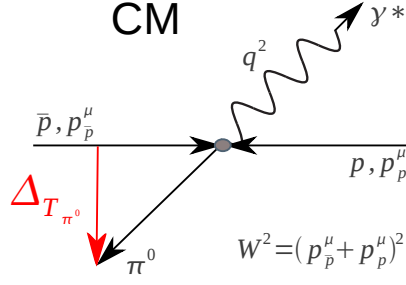
25

Figure 2.14: Definition of kinematic variables in the reaction $\bar{p}p \rightarrow e^+ e^- \pi^0$.

$$\int d\varphi_\ell \left| \overline{\mathcal{M}^{\bar{p}p \rightarrow \ell^+\ell^-\pi^0}} \right|^2 = \left| \overline{\mathcal{M}_T} \right|^2 \frac{2\pi e^2 (1 + \cos^2\theta_\ell)}{q^2}, \qquad (2.40)$$

and

$$\left| \overline{\mathcal{M}_T} \right|^2 = \frac{(4\pi\alpha_s)^4 (4\pi\alpha) f_N^4}{54^2 f_\pi^2} \frac{2(1+\xi)|I|^2}{\xi q^6}. \qquad (2.41)$$

with $\xi = \frac{q^2}{2W^2 - q^2}$.

Here φ_ℓ represents the polar coordinate of the leptonic decay, θ_ℓ is the azimuthal angle of the lepton pair, both defined in the center of mass system of the virtual photon, $\gamma^\star$, $f_N \sim 5.2 \cdot 10^{-3}\,\mathrm{GeV}^2$, $f_\pi = 131\,\mathrm{MeV}$ is the pion decay constant and $|I| = 1.28 \cdot 10^5$ is given by the TDA model [63, 64].

Combining the previous expressions we can obtain an explicit expression for the differential cross section at $\Delta_{T_{\pi^0}} = 0$:

$$\left. \frac{d\sigma}{dt\, dQ^2\, d\cos\theta_\ell} \right|_{\Delta_{T_{\pi^0}}=0} = K \frac{1}{W^2 - 4M^2} \frac{1}{(Q^2)^5} (1 + \cos^2\theta_\ell), \qquad (2.42)$$

where K is defined as:

$$K = \frac{(4\pi\alpha)^2 (4\pi\alpha_s)^4 f_N^4 |I|^2}{16 \cdot 54^2 (2\pi)^3 f_\pi^2}. \qquad (2.43)$$

In this Formula $\alpha_s = 0.3$ is the strong coupling constant.

Measurements of the cross section are necessarily done in physical regions of phase space with non-zero volume, *i.e.* the cross section has to be integrated over finite values of $\Delta_{T_{\pi^0}}$ and Q^2. Following Reference [62], the differential cross section in Equation (2.42) can be extrapolated up to a π^0 transverse momentum $\Delta_{T_{\pi^0}} < 0.5\,\mathrm{GeV/c}$, and integrated in the kinematic region defined by the $\Delta_{T_{\pi^0}}$ and Q^2 integration limits using

$$\Delta_t^2 = \frac{1-\xi}{1+\xi} \left(t - 2\xi \left[\frac{M_p^2}{1+\xi} - \frac{m_\pi^2}{1-\xi} \right] \right). \qquad (2.44)$$
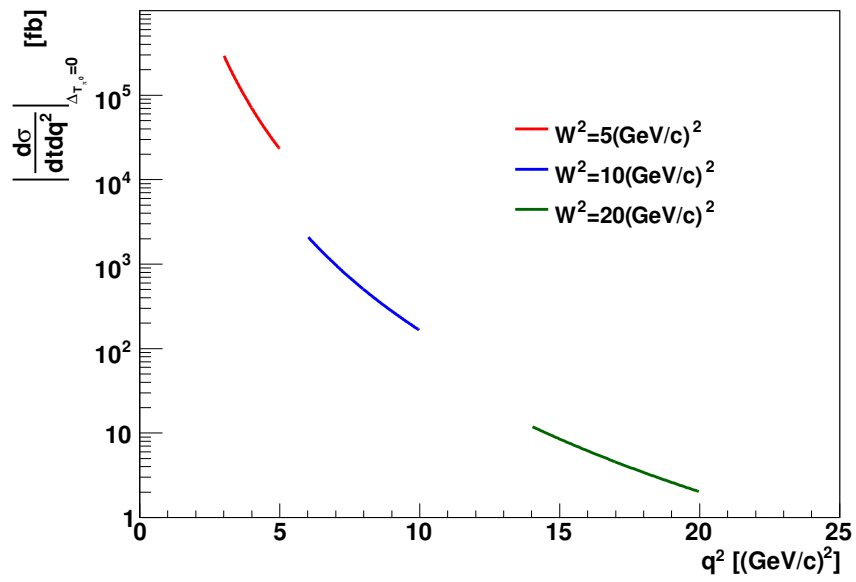
Figure 2.15: Cross section of $\bar{p}p \to e^+e^-\pi^0$ at $\Delta_{T_{\pi^0}} = 0$, for $W^2 = 5, 10,$ and $20\,(\text{GeV/c})^2$.

W^2	q^2_{min}	q^2_{max}	N_{events}
[(GeV/c)^2]	[(GeV/c)^2]	[(GeV/c)^2]	
5	3.61	4.41	150 000
10	5.76	9.18	6 000

Table 2.2: Number of expected signal events, $\bar{p}p \to e^+e^-\pi^0$, calculated from integration of the differential cross section (2.42) in the two-dimensional bin defined by $\Delta_{T_{\pi^0}} < 0.5\,\text{GeV/c}$ and the $q^2_{min} < q^2 < q^2_{max}$ for different values of center of mass energy squared, W^2, corresponding to an integrated luminosity of $\mathcal{L} = 2\,\text{fb}^{-1}$.

Figure 2.15 shows the cross section calculated in Formula 2.42 integrated over the lepton azimuthal angle for three values of W^2. This differential cross section serves as input for a newly created event generator for the simulation and is used to calculate the expected statistics for an integrated luminosity of $\mathcal{L} = 2\,\text{fb}^{-1}$. The experimental study of the feasibility of measurement of this cross section with $\overline{\text{P}}$ANDA is shown in Chapter 7 in this Thesis.

2.4.1.1 Signal event generator

The differential cross section given by the Equation (2.42) presented in Reference [62] has been used as a basis to develop an event generator for the process

$$\bar{p}p \to e^+e^-\pi^0. \tag{2.45}$$

This differential cross section has been calculated in the limit $\Delta_{T_{\pi^0}} = 0$, when the π^0 is emitted with zero transverse momentum (see Figure 2.14), *i.e.* either in forward or in backward direction. Therefore, the event generator only takes into account π^0 emitted forward or backward along the z-axis. To calculate the number of expected events corresponding to a given value of the integrated luminosity, this cross section has been extrapolated up to a π^0 transverse momentum $\Delta_{T_{\pi^0}} < 0.5\,\text{GeV/c}$ and integrated in a kinematic region between q^2_{min} and q^2_{max} for two different values of the center of mass energy squared, $W^2 = 5\,(\text{GeV/c})^2$ and $W^2 = 10\,(\text{GeV/c})^2$, respectively.

Table 2.2 shows the expected number of signal events, $\bar{p}p \to e^+e^-\pi^0$, in these two kinematic regions for an integrated luminosity of $\mathcal{L} = 2\,\text{fb}^{-1}$. These values of the integrated cross section and number of expected events are the ones used later for the analysis.

2.4.1.2 Background cross section and event generator

An important part of the analysis is the study of the reachable background suppression. The major background channel to (2.45) is 3-pion production,

$$\bar{p}p \to \pi^+\pi^-\pi^0. \tag{2.46}$$

Currently, there are so far no experimental measurements in the kinematic region of interest and neither a theoretical calculation of the cross section for the above process is available. Therefore, several assumptions have been taken in order to have a starting point for the simulations.

First, it has been assumed that the cross section of the background is up to 10^6 times higher than the cross section of the signal. There is no strict theoretical reason to do so, but this is the same signal to noise ratio as for the channel $\bar{p}p \to e^+e^-$ in the study of the Electromagnetic form factors of the proton in time-like region (Chapter 6).

Second, because the angular distribution of the background is also unknown, the most conservative ansatz has been chosen, namely the same angular distribution has been used to simulate signal and background. This represents the worst condition to separate signal from background, and is thus the best election for a starting point. If all the background is rejected in this case, we expect that with another angular distribution, the background rejection will be at least the same or better.

3

The $\overline{\text{P}}$ANDA experiment at FAIR

This Chapter is presented as a summary of the Conceptual Design Report developed in Reference [4], therefore most of the information is extracted directly from this Reference. The setup of $\overline{\text{P}}$ANDA and an overview of the complete physics program is explained. The characteristics of the Facility for Antiproton and Ion Research (FAIR) are also briefly introduced, and the main storage ring for the antiproton beam, the High Energy Storage Ring (HESR), is described.

3.1 FAIR **and the** HESR

The future Facility for Antiproton and Ion Research (FAIR) (Figure 3.1) that will be build at GSI (Helmholtzzentrum für Schwerionenforshung) in Darmstadt will be a facility for research with antiprotons and ions [65]. This project considers the use of the current accelerators available at GSI to be upgraded and used as injectors for the new installations. The main element of FAIR will be a double ring accelerator for antiprotons with a 1.1 km of perimeter. Connected to it there will be a complex of storage rings and experimental halls. $\overline{\text{P}}$ANDA is one of the major projects of FAIR. It will be located in the High Energy Storage Ring (HESR) to make use of the accumulated antiproton beam. The HESR will be dedicated to provide $\overline{\text{P}}$ANDA with high-quality antiproton beams with a momentum range between 1.5 to 15 GeV/c. Pre-cooled antiprotons will be injected with a momentum of 3.8 GeV/c. The HESR will work at the beginning as a slow synchrotron to bring the beam to the desired energy and then as a storage ring. Both, electron- and stochastic-cooling systems are necessary to assure the required beam quality. The HESR will have two operation modes. The high luminosity mode, with beam intensities up to 10^{11} antiprotons stored in the
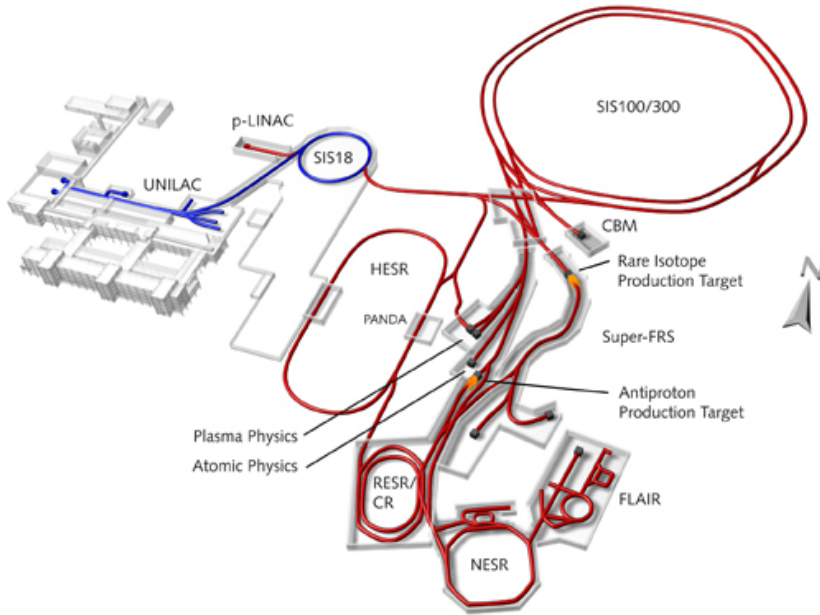
Figure 3.1: FAIR facility at GSI.

HESR and a momentum spread of $\frac{\Delta p}{p} \sim 10^{-4}$, will be used for experiments that require high statistics. The high resolution mode, with momentum spreads on the order of $\frac{\Delta p}{p} \sim 10^{-5}$ and beam intensities slightly lower ($\sim 10^{10}$), will be useful for high precision physics experiments. Together with the proton target foreseen for the $\overline{\text{P}}$ANDA experiment, the luminosities achieved in each mode are expected to be of $2 \cdot 10^{32}$ cm^{-2}s^{-1} for the high luminosity mode and $2 \cdot 10^{31}$ cm^{-2}s^{-1} for the high resolution mode.

3.2   Physics program of $\overline{\text{P}}$ANDA

The $\overline{\text{P}}$ANDA experiment will use the antiproton beam from the HESR hitting an internal proton target, and a general purpose spectrometer to carry out a rich and diversified hadron physics program. The experiment is designed to fully exploit the extraordinary physics potential arising from the availability of high-intensity, cooled antiproton beams. The aim of the rich experimental program is to improve our knowledge of the strong interaction and of hadron structure. Significant progress beyond the present understanding of the field is expected thanks to improvements in statistics and precision of the data.

Many experiments are foreseen in $\overline{\text{P}}$ANDA. The most important fields of research are exposed very briefly in the following.

3.2.1 Electromagnetic processes

Electromagnetic processes are the processes studied in this Thesis. They summarize a class of processes in which a photon (real or virtual) couples to the electromagnetic current of a proton or an antiproton, thus being sensitive to nucleon structure observables. The measurement of the process $\bar{p}p \to e^+e^-$ for example will allow the determination of the electromagnetic form factors (EMFF) of the proton in the time-like region over an extended q^2 range with unprecedented accuracy. Also the study of the transition distribution amplitudes (TDA) via the channel $\bar{p}p \to e^+e^-\pi^0$ will open a new way to study how the transition between baryons occurs. Feasibility studies for the measurement of the channels $\bar{p}p \to e^+e^-$ and $\bar{p}p \to e^+e^-\pi^0$ are presented in this Thesis (Chapters 6 and 7). The main problem in the reconstruction of these channels is the large hadronic background, 10^6 times higher in average only for pions. Good tracking and momentum reconstruction capabilities, and very good particle identification are required for a clean identification of the signal channels.

3.2.2 QCD bound states

The study of bound states of quarks and gluons in the charmonium region is fundamental for a better and quantitative understanding of the theory. Using non-relativistic potential models, effective field theories and Lattice QCD different particle spectra can be computed. To be able to distinguish between the different theoretical approaches and to identify the relevant degrees of freedom, precision measurements are needed. The search for other exotic states as gluonic hadrons (hybrids and glueballs), multiquarks and molecular states will be also an important point in this field. Due to the high resolution mode of the HESR precision scan of the line width of recently observed exotic resonances (so called $X, Y, Z-$states) can reveal their nature.

3.2.3 Non-perturbative QCD dynamics

Using the quark picture, the pair production of hyperons either involves the creation of a quark-antiquark pair or the ejection of such pairs out of the nucleon quark-see. By measuring reactions of the type $\bar{p}p \to \bar{Y}Y$, Y denoting a hyperon, the quark-antiquark creation mechanism can be studied. The OZI rule, which explains why certain decay modes appear less frequently than expected, and its possible violation can be tested for different levels of disconnected quark-line diagrams by comparing several reactions involving different quark flavors.

3.2.4 Study of hadrons in nuclear matter

The study of medium modifications of hadrons embedded in hadronic matter is directed to understand the origin of hadron masses in the context of spontaneous chiral symmetry breaking in QCD and its partial restoration in a hadronic environment. So far experiments have been focused on the light-quark sector. The high-intensity $\bar{p}$ beam of up to 15 GeV/c will allow an extension of this program to the charm sector for hadrons with hidden and open charm. The in-medium masses of these states are expected to be affected primarily by the gluon condensate. The extremely narrow states in the charm sector, like for example the J/ψ, will increase the sensitivity for such medium modifications enormously.

3.2.5 Hypernuclear physics

Hypernuclei are systems in which an up or down quark in a nucleon is replaced by a strange quark, thus yielding bound states of nucleons and hyperons. In this way a new quantum number, strangeness, is introduced into the nucleus and allows for the study of nucleon-hyperon interactions. Single and double Λ-hypernuclei were discovered many decades ago but only 6 double Λ-hypernuclei are currently known. The availability of antiproton beams at FAIR will allow efficient production of hypernuclei with more than one strange hadron, making P̄ANDA competitive with experiments planned at J-Park. The presence of a strange quark in the nucleon, not subjected to the Pauli principle like the other nucleons, opens perspectives for nuclear structure spectroscopy. In addition the forces between hyperons and nucleons can be studied in these experiments.

3.2.6 Electroweak physics

The high-intensity $\bar{p}$ beam available at the HESR allows the possibility of observing rare weak decays due to the high cross section for D-meson production. This would be useful to test predictions of the Standard Model and search for new physics. For example for testing CP violation via hyperon decays of the order of 10^{10} reconstructed decay events are required. This statistics would be reachable within a year of measurement with P̄ANDA under ideal conditions: good vertex reconstruction and excellent particle identification in forward and backward directions.

A more detailed description of the P̄ANDA physics program and its implications can be found in Reference [4].
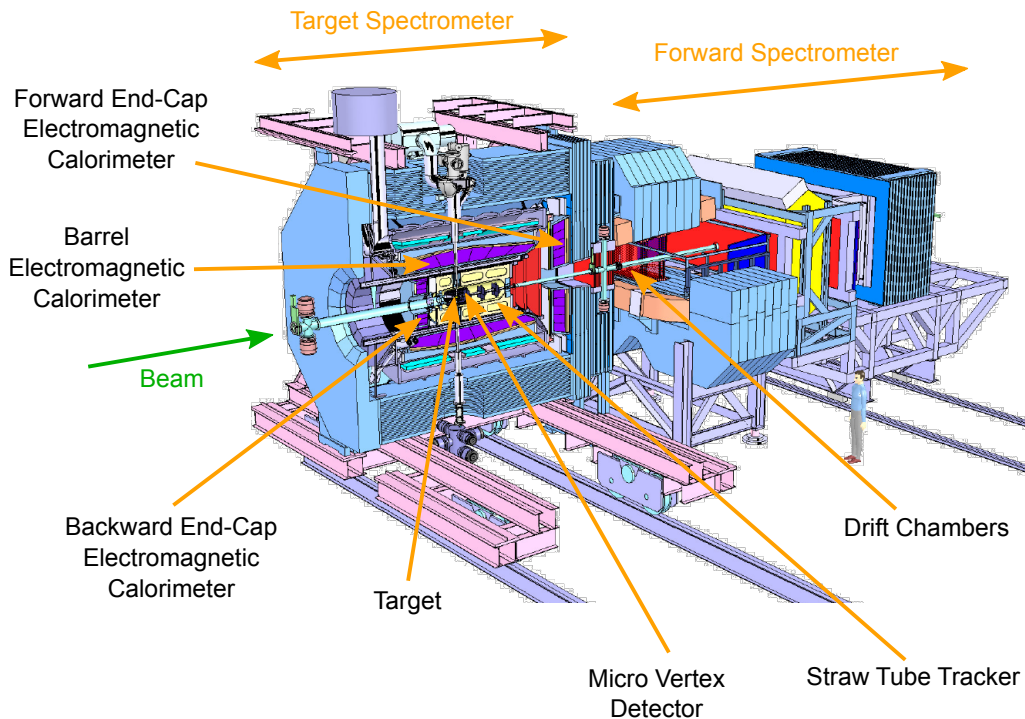
3.3   Detector overview

Figure 3.2: Artistic view of the $\overline{\text{P}}$ANDA detector [66].

To fulfill the ambitious physics program, the $\overline{\text{P}}$ANDA detector needs to have certain characteristics. The experiment uses a fixed-target, with the consequence of the boost due to the center of mass motion. One of the main objectives of the detector is to achieve 4π acceptance and high resolution for tracking and momentum reconstruction. Therefore an arrangement that uses a target spectrometer surrounding the target region and a forward spectrometer covering small angle tracks is foreseen. Good particle identification (PID), calorimetry and high rate capability are also required. Detectors to fulfill these requirements have been developed for both parts of the spectrometer. In this Section an overview of the $\overline{\text{P}}$ANDA detector described in Reference [4] is shown. In Figure 3.2 one can see an artistic view of the $\overline{\text{P}}$ANDA detector setup. In the following the components of all detector subsystems are briefly described.

3.3.1   Target spectrometer

The target spectrometer consists of different detectors arranged in various layers. They are placed inside a solenoid magnet which will provide a highly homogeneous magnetic field in the region of the target and tracking detectors.

All the subdetectors will be arranged in three different sections. A forward end-cap to cover forward angles up to 5° in the vertical direction and up to 10° in the horizontal direction, a barrel part covering angles between 22° and 140° and a backward end-cap region covering angles between 145° to 170°. Part of this work has been the study of the backward endcap of the electromagnetic calorimeter (BWEMC), placed in the backward region (Chapter 5). A cut through the target spectrometer is shown in Figure 3.3.
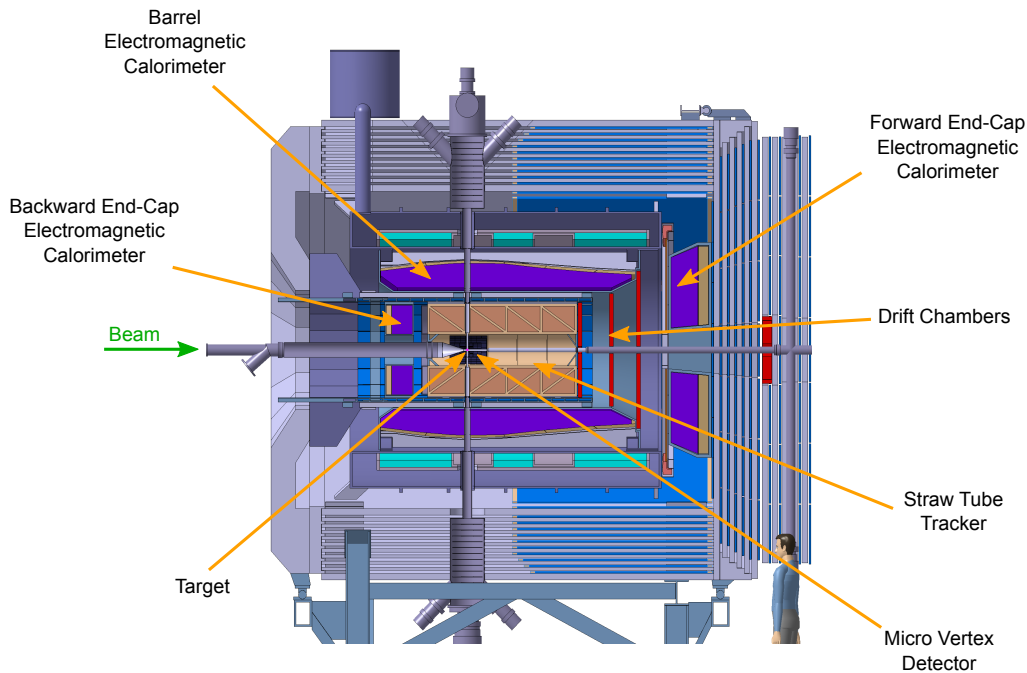

Figure 3.3: Cut through the target spectrometer [66].

The beam pipe will be intersected by a vertical conduit required for the injection of the target material of frozen hydrogen pellets. In the barrel part, surrounding the target region, the tracking detectors will be placed at the innermost layer. The micro vertex detector (MVD), composed of silicon pixel strip detectors, will be used for high precision tracking and displaced vertex reconstruction. A straw tube tracker (STT), will be placed around the MVD to fulfill the requirements of the tracking system. After the tracking detectors a detector for internally reflected Cherenkov light (DIRC) and time-of-flight (TOF) systems are foreseen for the PID. These detectors will be placed on the inside of the barrel electromagnetic calorimeter (EMC), which will be used to reconstruct the shape of electromagnetic showers and measure the energy of electrons and photons. Using the shower shape information, also discrimination against neutral mesons is possible with this detector. All these detector systems will be placed inside a super-conducting solenoid. This solenoid will provide a highly homogeneous magnetic field of 2 T parallel to the beam direction. Detectors for
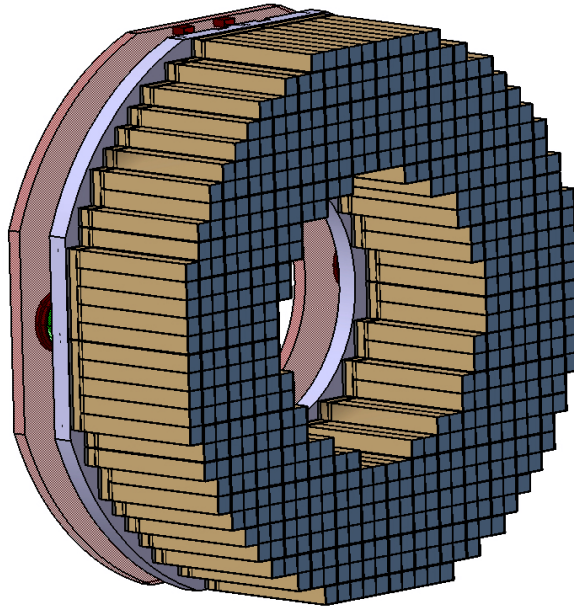
Figure 3.4: Artistic view of the BWEMC of $\overline{\text{P}}$ANDA.

muon identification will be interleaved with the iron yoke of the solenoid magnet. In forward direction, additional tracking stations and an end-cap Cherenkov detector as well as the forward endcap of the electromagnetic calorimeter are foreseen. The BWEMC will mainly cover the backward part of the spectrometer ($\sim 145°$ to $\sim 167°$). This detector is especially important for this work. Simulations have been done to check its energy resolution and efficiency. The results can be found in Chapter 5. A picture of the BWEMC can be seen in Figure 3.4. Due to the fixed target kinematics, the barrel and backward section of the target spectrometer measures lower energy particles. For momenta larger than 800 MeV/c, the DIRC provides pion-kaon separation [4]. PID for slower particles will be provided by energy loss measurements in the tracking detectors and by the TOF detector.

3.3.1.1 Target system

Different considerations are under study for the realization of the target system. The geometrical constraints as well as the necessities for developing the programmed experiments have to be taken into account. Basically, two different options are contemplated for the main physics program: a cluster jet target and a pellet target. In addition, other kind of targets could be used for the nuclear physics program or for the hypernuclear program.

Cluster jet target

The possibility of a cluster jet target is under intense study due to the high homogeneous profile that can be achieved. This is the main advantage of this kind of target. It consists of a narrow supersonic jet of hydrogen clusters produced after the injection of pressurized cold hydrogen gas into the vacuum through a specially shaped nozzle. The size of the clusters can be adjusted by the gas pressure between 10^3 to 10^6 hydrogen molecules, tending to become larger at higher inlet pressure and lower nozzle temperature. Over the time the experiment will be running, the density of the cluster jet can be adjusted to keep the instantaneous luminosity constant as the number of antiprotons in the HESR decreases with the number of interactions. The main disadvantage of this kind of target is the uncertainty in the determination of the interaction position, due to the lateral spread of the cluster. The target extension can be of the order of several millimeters, and the precision on the determination of the interaction point has to rely basically on the precision of the tracking system in the determination of displaced vertices. In addition, the demands of $\overline{\mathrm{P}}$ANDA require a higher cluster density in comparison to currently achieved values. A target density of $8 \cdot 10^{14}$ hydrogen atoms per square centimeter is achieved with a nozzle prototype using the exact geometry of $\overline{\mathrm{P}}$ANDA [67]. More research is being done to increase this density.

Pellet target

The pellet target device will produce a stream of frozen hydrogen pellets falling past the $\bar{p}$ beam. A standard achievable pellet production rate is on the order of $(1.0 - 1.5) \cdot 10^4 \, \mathrm{s}^{-1}$ with pellets sizes of $25 - 40 \, \mu\mathrm{m}$, and velocities about 60 m/s. At the interaction point the pellet stream has a lateral spread of the order of $\sigma \approx 1$ mm. The distance between the pellets varies between 0.5 to 5 mm. The main advantage of this system is the achievable high resolution in the determination of the vertex position. Due to the large interaction time between the pellet and the beam the number of produced reactions will be high enough to reproduce exactly the pellet position statistically. In addition a tracking system for the pellets is also being considered. The expected resolution on the vertex position determination is about the $50 \, \mu\mathrm{m}$. This kind of target is currently used at the WASA at COSY experiment [68] and was previously developed at TSL [69]. The design of the $\overline{\mathrm{P}}$ANDA pellet target is based on the COSY device. The main inconvenience of this kind of target is the large variation of the instant luminosity that can occur. A strong variation in the instantaneous luminosity results in a major challenge in coping with large associated fluctuation of the particle rates. Investigations to improve the luminosity variations are carried on.

Other targets

Other kind of targets, as liquid He target or polarized ^{3}He are under investigation to extend the $\overline{\text{P}}$ANDA research capabilities [66]. For solid target materials, a wire target is considered. For the hypernuclear program, the whole target region and upstream end-cap of the $\overline{\text{P}}$ANDA detector has to be redesigned. A primary and a secondary target, as well as appropriate detectors are necessary for this research [70].

3.3.1.2 Tracking system

The tracking system of the target spectrometer of $\overline{\text{P}}$ANDA will consist of three subdetector systems. The MVD surrounded by the STT in the central part of the target spectrometer and in the forward direction completed with a detector based on gas electron multiplier (GEM) stations.

Micro vertex detector

The MVD is the closest detector to the interaction region. Its design is thought to achieve the maximum acceptance possible. Its main purpose is the reconstruction of secondary decay vertices of short-lived particles like hyperons and strange and charmed mesons. It will also improve the transverse momentum resolution.

The design of the MVD is based on radiation-hard silicon pixel detectors with fast individual pixel readout circuits and silicon strip detectors. A four-layer barrel detector with an inner radius of 2.5 cm and an outer radius of 13 cm is foreseen. In addition, eight detector wheels arranged perpendicular to the beam in forward direction will contribute to the improvement of the acceptance and will help in the reconstruction of hyperon cascades.

The two innermost barrel layers and the four first wheel layers will be made entirely of silicon pixel detectors. The two outer barrel layers and the last two wheels will consist of double-sided silicon strip detectors. The rest of the perpendicular wheels will be a combination of pixel and strip silicon detectors.

Straw tube tracker

The STT is a cylindrical gas detector with a total length of 1.5 m and a maximum outer radius of 420 mm [71]. The total angular coverage of this detector goes from $\theta \sim 8°$ to $\theta \sim 160°$. Its building-block unit is an aluminized Mylar foil rolled up to a tube with an anode wire inside. The diameter of each tube is 1 cm and they are arranged forming an hexagonal shape around the MVD. The straws are filled with an Argon and CO_2 gas mixture to be operated at a stabiliz-

ing overpressure of 1 bar (*i.e.* a total pressure of 2 bar). This renders the straws self supporting. Charged particles traversing the gas volume ionize it and the free charges drift to the anode due to the the high voltage difference between tube and anode. The small diameter of the tubes assures a very small drift volume allowing a very fast readout. The gas mixture proportions are chosen to limit the gain to 10^5 in order to ensure a long term stability. A position resolution in $x-y$ coordinates of about $150\,\mu\text{m}$ is expected. Along z it is expected to be about $3\,\text{mm}$ for single hits [71].

Forward GEM detectors

To be able to cover angles below $22°$ three GEM stations placed in forward direction at 1.1 m, 1.4 m and 1.9 m from the target are foreseen. The detectors in this area have to be able to support the high counting rate due to the fixed target kinematics. GEM detectors can be operated in high rate environments and its read out is much faster compared to other kind of gas detectors.

3.3.1.3 PID detectors: Cherenkov detectors and time-of-flight

One of the main requirements of $\overline{\text{P}}$ANDA is the identification of charged particles over a large range of angles and momenta. Particles with momenta higher than 1 GeV/c will be identified in the Cherenkov detectors. A TOF detector is foreseen to identify slower particles. Energy loss measurements of other detectors and shower shape information in the calorimeter will be combined with the information of the Cherenkov and TOF detectors dedicated to PID to reach better results in the classification.

Barrel and disc DIRC

The use of Cherenkov light to identify the nature of a particle is a common technique used in many experiments. The Cherenkov detector foreseen for $\overline{\text{P}}$ANDA is based on the DIRC detector of the BaBar experiment [72]. At polar angles between $22°$ and $140°$, quartz slabs with a 1.7 cm thickness will surround the beam pipe at a distance of $45-54\,\text{cm}$. The Cherenkov light will be focused onto micro-channel plate multiplier detectors (MCP PMT) which are insensitive to magnetic fields.

In the forward direction, a disk made of the same quartz material will cover the angles between $5°$ and $22°$. The disk DIRC will be 2 cm thick and will have a radius of 110 cm. It will be placed directly upstream of the forward endcap of the electromagnetic calorimeter. The focusing of the light will be done using mirrors reflecting it onto the MCP PMT.

The geometry of the barrel and the disc DIRC detectors will allow the determination of two spatial coordinates and the measurement of the light propagation time. This will be a very fast detector and will allow also a very compact design. The good time resolution of the MCP PMT is taken into account.

Time-of-flight detector

For slow particles, PID will be provided by a TOF-tile detector in the barrel part. The time resolution of this detector has to be of 50 ps to 100 ps due to the small dimensions of $\overline{\mathsf{P}}$ANDA. The use of a start detector is not possible due to the space constraints. Therefore only relative timing between different particles has to be used. Scintillation bars or multi-gap resistive plate chambers are two possible options to be used for this device. The TOF detector will cover angles between $22°$ and $140°$ and it will be placed around the STT at a distance around 42 cm to 45 cm from the beam pipe.
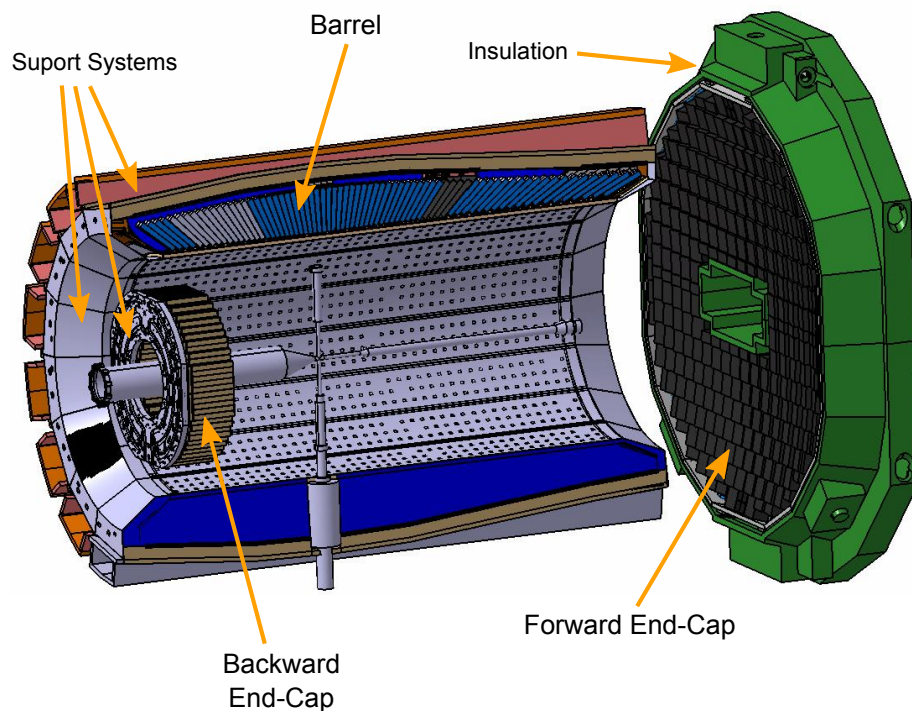

Figure 3.5: Technical drawing showing the structure of the $\overline{\mathsf{P}}$ANDA EMC, including the forward endcap of the electromagnetic calorimeter with its insulation system (in green), the barrel with the support system (light blue and orange) and a cut where one can see the arrangement of the crystals in the upper part, and the BWEMC with the mounting plate (gray disc) system placed around the beam pipe.

41

ρ [g/cm^3]	8.28
X_0 [cm]	0.89
R_M [cm]	2.00
τ_{decay} [ns]	6.5
λ_{max}[nm]	420
n at λ_{max}	2.17
relative LY at RT %(LY of NaI)	0.6
relative LY at -25°C %(LY of NaI)	2.5
hygroscopic	no
dLY/dT [%/°C]	-3.0 at RT
dE/dx (MIP) [MeV/cm]	10.2

Table 3.1: Properties of the PbWO$_4$ crystals of $\overline{\text{P}}$ANDA. Values extracted from Reference [79].

3.3.1.4 Electromagnetic calorimeters

The geometry of the EMC calorimeter of $\overline{\text{P}}$ANDA is subjected to the expected high count rates and the necessity of a compact design. A fast scintillator material with a short radiation length and Molière radius is required. Lead Tungstate (PbWO$_4$), a high density inorganic scintillator fulfills the requirements. With this material sufficient energy and time resolution can be achieved for the detection of electrons, photons and hadrons even at intermediate energies [73–75]. For high energy physics, this material has been chosen also by the CMS and ALICE collaborations at CERN [76, 77] and it has been optimized for large scale production. A short decay time of less than 10 ns and good radiation hardness has been achieved [78] for this kind of crystals. Recent developments yield a significant increase of light yield due to eliminating crystal imperfections, and introducing the appropriate doping. This enables photon detection in $\overline{\text{P}}$ANDA down to a few MeV with sufficient resolution. The light yield can be increased further by a factor 4 compared to room temperature by cooling the crystals down to -25°C. The properties of the PbWO$_4$ crystals can be read in Table 3.1.

In the design foreseen for $\overline{\text{P}}$ANDA the PbWO$_4$ crystals for the barrel and the forward end cap will be tapered with a front size of 2.1×2.1 cm^2 and 20 cm long, *i.e.* approximately $22X_0$. An energy resolution below 2% at 1 GeV can be achieved with these crystal dimensions [73–75] with a tolerable energy loss due to longitudinal leakage of the shower. The crystals will be mounted around the tracking and PID detectors with an inner radius of 57 cm. This implies 11 360 crystals in the barrel part. The forward end-cap calorimeter will have 3600 tapered crystals, they will be mounted downstream the interaction point, facing

the interaction region at a distance of 202 cm. For the backward end-cap 540 straight crystals with a front cross section of 24.4×24.4 mm^2 are foreseen. They will be mounted parallel to the beam pipe forming a shape with an inner radius of 182 mm and an outer radius of 406 mm. The center of mass of the crystals will be placed 694 mm upstream from the target. The readout of the crystals will be accomplished by large area avalanche photodiodes (LAAPD) in the barrel and the backward end-cap, and vacuum photo-triodes (VPT) or vacuum photo-tetrodes (VPTT) in the forward end-cap.

Figure 3.5 shows a schematic drawing of the current geometry of the calorimeter.

Note that the first part of the work reported in this Thesis (Chapter 6) has been done with a previous design of the geometry for the BWEMC. Originally it consisted of 592 tapered crystals placed upstream from the target position. The geometry was changed to cover a bigger solid angle. The old geometry was also used for the analyses presented in Reference [4].

3.3.1.5 Solenoid magnet

A superconducting solenoid with an inner radius of 90 cm and a length of 2.8 m will provide the magnetic field in the target spectrometer. The maximum magnetic field will be 2 T and the field homogeneity is expected to be better than 2% over the volume of the MVD and the STT. The cryostat for the solenoid will have two warm bores of 100 mm diameter, one above and one below the target position, to allow the insertion of internal targets. The coil will be provided with an external iron return yoke to improve the characteristics of the magnetic field.

3.3.1.6 Muon detectors

The iron yoke of the solenoid magnet will serve as a holder for the muon detectors, which will be installed inside the yoke. The muon detectors will be necessary for the separation of primary and secondary muons and pions. The iron yoke of $\overline{P}$ANDA will be segmented and used as an absorber with interleaved tracking detectors to measure energy loss of different particles. The muon detectors in the barrel region will be a group of 3 cm thick layers, separated by 3 cm thick iron layers. In the forward direction, the muon detector has to be split because of the size of the iron yoke in this direction. Extra layers will be placed between the target spectrometer and the forward spectrometer to complete the required amount of material for this detector. The detector used here will consist of rectangular aluminum drift tubes, based in the system used in COMPASS [80].
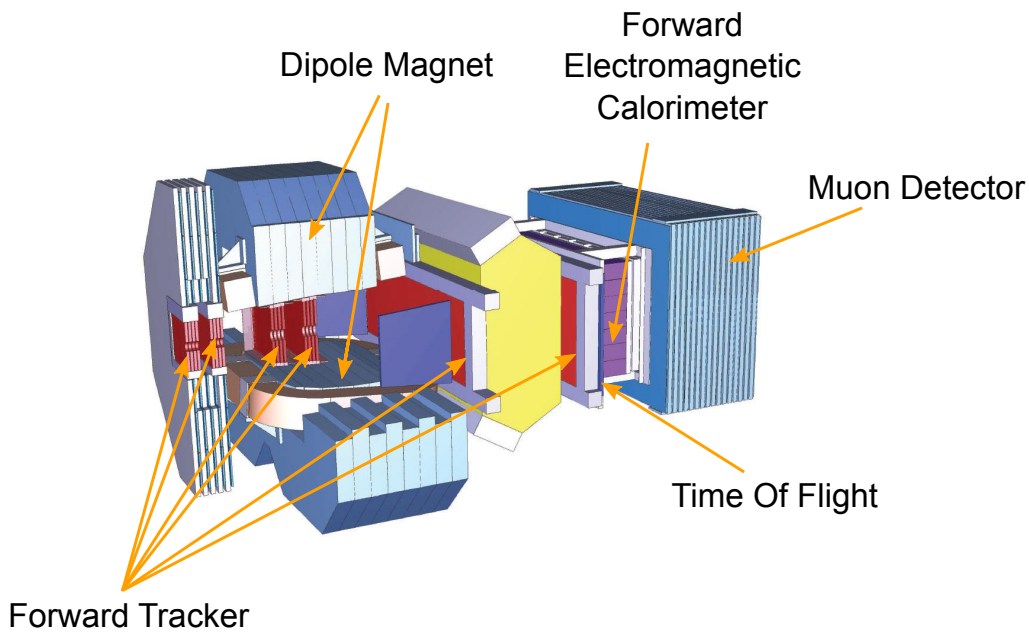
Figure 3.6: forward spectrometer of the P̄ANDA experiment [66].

3.3.1.7 Hypernuclear detector

For the study of Hypernuclei, a secondary target is foreseen. Also specific recoil detectors are needed. These elements will not be used during the rest of the physics program of P̄ANDA. The geometry of this setup is not within the scope of this work, however a detailed description of these detectors and the processes involving hypernuclei physics can be found for example in Reference [70].

3.3.2 Forward spectrometer

3.3.2.1 Dipole magnet

To cover the angular acceptance of the forward spectrometer (Figure 3.6), $\pm 10°$ and $\pm 5°$ in the horizontal and in the vertical direction respectively, a dipole magnet with a 1 m gap and more than a 2 m aperture will be used. The magnet yoke will be about 2.5 m long and will be placed at 3.5 m from the target. The maximum bending power will be of 2 Tm which corresponds to 2.2° deviation for antiprotons at the maximum momentum of 15 GeV/c. The beam deflection will be compensated by two correcting dipole magnets placed in the HESR around the P̄ANDA detection region [4].

3.3.2.2 Forward trackers

The tracking of particles entering the forward spectrometer will be done with a set of wire chambers, two placed in front of the dipole magnet, two within, and two behind it. This will allow one to track high momentum particles as well as very low momentum particles whose trajectories curl up inside the dipole.

Each chamber will contain three pairs of detection planes, with drift cells of 1 cm width each. One of the detection planes will be vertical and the other two will be inclined by $+10°$ and $-10°$ respectively. This will allow the reconstruction of the tracks in each chamber separately. The beam pipe will pass through central holes in the chambers.

The momentum resolution for 3 GeV/c protons is expected to be about $\delta p/p = 0.2\%$ and is limited by small-angle scattering from the chamber wires and the chamber gas.

3.3.2.3 Forward PID

RICH detector

The good separation between π/K and K/p at high momenta will be assured with a ring imaging Cherenkov counter (RICH) similar to the one used at HERMES [81] or COMPASS [82].

Using two radiators, silica aerogel and C_4F_{10} gas, it will provide $\pi/K/p$ separation in a momentum range from 2–15 GeV/c. The Cherenkov light will be focused by a mirror onto an array of phototubes outside the active volume. This allows to reduce the total thickness of the system to the thicknesses of the gas radiator ($5\% X_0$), the aerogel radiator ($2.8\% X_0$), and the aluminum window ($3\% X_0$).

TOF wall

A TOF stop counter placed 7 m away from the target is also foreseen. It will consist of a wall of slabs made of plastic scintillators with widths varying from 5 to 10 cm and read out on both ends by fast photo tubes. Similar detectors will also be placed inside the dipole magnet opening to detect low momentum particles which stop before exiting the magnetic field. The expected time resolution will be of $\sigma = 50$ ps, π/K and K/p separation on a 3σ level will be possible up to momenta of 2.8 GeV/c and 4.7 GeV/c, respectively.

3.3.2.4 Forward electromagnetic calorimeter

A Shashlyk-type calorimeter is foreseen for the detection of photons and electrons in the forward spectrometer. The technique has already been successfully used in the E865 experiment [83] and it has been also adopted for various other experiments [84–89] An energy resolution of at least $4\%/\sqrt{E}$ [87] can be achieved. The detection is based on lead-scintillator sandwiches read out by wavelength shifting fibres imbedded in the scintillators and coupled to photomultipliers. To cover the forward acceptace are needed 351 Shashlyk modules arranged in 13 rows and 27 columns. This detector will be placed at 7.5 m from the interaction region.

3.3.2.5 Forward muon detectors

A muon detector similar to the one in the target spectrometer is designed for higher momenta particles. It will be usefull to discriminate pions from muons, the detection of pion decays and for the determination, with moderate resolution, of neutrons and antineutron energies.

3.3.3 Luminosity monitor

The determination of the luminosity is crucial for every experiment and so will it be for $\overline{P}$ANDA. A luminosity monitor is being designed to measure the luminosity of the experiment online. The concept of this detector is based in the measurement of the Coulomb-scattered elastic $\bar{p}p$ events. The luminosity monitor will consist of four planes of doubled-sided silicon strip detectors placed as close to the beam axis as possible and at a distance between 10 to 12 m from the target. The planes will be separated by 20 cm along the z-direction. The determination of the luminosity is expected to be 3% absolute precission [4].

4

Simulation and analysis software

The software framework used for the simulation and analysis described in this Thesis has been originally ported from the framework of the BaBar experiment. It is the same software used for the analyses presented in the $\overline{\text{P}}$ANDA Physics Book [4]. Therefore this Chapter is presented as a summary of Chapter 3 in the named Reference and most of the information is extracted from there.

4.1 The simulation software

The software follows an object-oriented approach, and most of the code is written in C++. Several well-tested software tools and packages from other high-energy-physics experiments have been adapted to the needs of $\overline{\text{P}}$ANDA. The software contains

- event generators with accurate decay models for the individual physics channels, as well as for the relevant background channels,

- particle tracking through the complete $\overline{\text{P}}$ANDA detector using the GEANT4 transport code,

- simulation of signals in the individual detectors and their processing in the front-end electronics,

- reconstruction and identification of charged and neutral particles that provide lists of particle candidates for the physics analysis, and

- user-friendly high-level analysis tools that allow the use of vertex and kinematic fits to reconstruct extensive decay trees very easily.

In the following sections the most important features used in this work are explained.

4.2   Event generation

For the generation of the events for the benchmark reactions `EvtGen` [90] was used. It takes into account the known decay properties of the particles and angular distributions of the reactions, as well as polarization states. It also permits to use user-defined decay models. Once the events have been generated, they are given as an input to the detector simulation.

4.3   Detector simulation and particle tracking

The next step in the simulation process is to perform the transport of the particles through the detector. For this purpose GEANT4 [91, 92] is used, which takes into account all possible interactions and decays that the different particles may undergo. As an output of this step one gets a collection of hits in the different parts of the detector. This hits contain information about the intersection points and energy losses of all particles in every individual subdetector. The digitization process follows to this step. It takes into account the information of the hits collection and models the digitization of the signals in the front-end electronics. The objective is to produce a digitized detector response as close as possible to real data. This ensures that the same reconstruction code used in the analysis of Monte Carlo data can be used in the future to the analysis of real data. An effective smearing of the data has been used in some steps of the simulation to improve the performance of the software. The values for the smearing were derived from full Monte Carlo simulations and they are explained in the following sections.

4.3.1   Detector setup and geometry

The geometrical description of the $\overline{\text{P}}$ANDA detector is written using extensible markup language (XML) files, which allow an easy integration into a C++ environment.

For the simulations the complete $\overline{\text{P}}$ANDA setup described in Chapter 3 is used. The time-of-flight (TOF) detectors and the forward ring imaging Cherenkov counter (RICH) detectors are not included. The muon detector consists only of two scintillator layers instead of a multilayer scenario within the iron yoke. This was the most favored option during the implementation of the

geometry into the software. For the $\bar{p}p$ reactions the pellet target is chosen as an internal target, taking into account the material budget introduced by the target pipe and the pumping stations. The interaction point is considered with a spread of $\sigma = 0.275$ mm in each direction. Concerning the backward endcap of the electromagnetic calorimeter (BWEMC) the old version of the detector is used in the first physics simulations showed in this work, related with the electromagnetic form factors (EMFF) (Chapter 6). This is consisting of tapered crystals pointing to the target. To be able to cover a bigger solid angle, the design of the BWEMC was modified, and straight crystals are now used instead. The new geometry, described in Section 3.3.1.4, is used in the studies of the BWEMC energy resolution and efficiency (Chapter 5) and for the simulations concerning the transition distribution amplitudes (TDA) (Chapter 7)

4.3.2 Digitization

4.3.2.1 Readout of the tracking devices

Silicon readout of the MVD

The micro vertex detector (MVD) is composed by two different silicon detector types, silicon strip and pixel detectors. The readout is treated differently in the digitization process.

The signal is formed by using the local trajectory within the detector material to calculate the corresponding channel relative to the readout matrix of the sensor. The channel number, the deposited energy and the charge collected by the electronics are defined by the hit position on the sensor surface. The channel mapping of the particle trajectory is done on both sides of the sensor. For the pixel detectors the particle trajectory is projected onto the surface, all excited pixels are determined, and the charge is shared among the pixels depending on the fraction of the intercepted track. For the strip sensors the formation of digitized channels is done independently on both sides of the sensor. The procedure is similar to the pixel case but done only in one dimension.

The sizes of the readout structures are defined by the size of the pixel cell or the spacing of the strips. Each channel is assigned to a front-end, and a common number of 128 channels per front-end is chosen. The size of the ATLAS front-end chip was chosen for the pixel detector and it was used as the basis to assign channels to front-ends. The number of pixels per front-end is defined by the dimension of the front-end chip. The threshold for the electronics was set to the equivalent of 300 electrons, which is a reasonable value for pixel detectors.

STT and the drift chambers

The digitization of the signal from the straw tube tracker (STT) and the drift chambers (DCH) is treated in a similar way. Both detectors consist of wires inside a gas volume of Ar/CO$_2$. If a charged particle traverses the gas volume and ionizes the gas, the local helix trajectory is derived from the corresponding GEANT4 intersection points. The drift time of the ionization electrons is estimated from the minimum distance, d_h, between the helix trajectory to the wire. The uncertainty of the drift time measurement is taken into account by smearing the value of d_h with a Gaussian with a standard deviation of $\sigma = 150\,\mu\text{m}$ for the STT, and $\sigma = 200\,\mu\text{m}$ for the DCH.

The average number of primary ionization electrons is given by the total energy deposited in the gas volume divided by the ionization energy of 27 eV for the Ar/CO$_2$ gas mixture. The energy signal is finally calculated by using Poisson statistics.

The information about the energy deposited in the MVD and especially in the STT will be very important in the particle identification (PID) process. The separation of pions and electrons is crucial for the work presented in this Thesis and it will be possible thanks to the information provided by these detectors (see Section 4.4.3).

GEM readout

Each gas electron multiplier (GEM) detector consists of two planes separated by 1 cm. Each detector plane has two strip detector layers with perpendicular orientation to each other. The gas amplification process and the response of the strip detector was not simulated in detail. Instead, the entry point of a charged track into the detector plane was taken directly from GEANT4 and smeared by a Gaussian distribution of 70 μm width for each strip.

4.3.2.2 Readout of the DIRC

In the detector for internally reflected Cherenkov light (DIRC) the light propagation in the Cherenkov radiators, the signal processing in the front-end-electronics, and the reconstruction of the Cherenkov angle are modeled in a single step.

The resolution of the reconstructed Cherenkov angle σ_{Ch} is driven by the uncertainty of the single photon angle $\sigma_{\text{Ch},\gamma}$ and the statistics of the relatively small numbers of detected Cherenkov photons N_γ

$$\sigma_{\text{Ch}} = \frac{\sigma_{\text{Ch},\gamma}}{\sqrt{N_\gamma}}$$

A single-photon resolution of $\sigma_{Ch,\gamma} = 10\,\text{mrad}$ is used, corresponding to experience with existing DIRC detectors. The number of detected photons is calculated from the velocity, β, of charged particles passing through the quartz radiators and the path length L within the radiator, via

$$N_\gamma = \varepsilon\, 2\pi\alpha L \left(1 - \frac{1}{\beta^2 n_{\text{quartz}}^2}\right)\left(\frac{1}{\lambda_{\text{min}}} - \frac{1}{\lambda_{\text{max}}}\right),$$

where α is the fine structure constant and $n_{\text{quartz}} = 1.473$ is the index of refraction of quartz. The sensitive wavelength interval, $[\lambda_{\text{min}}, \lambda_{\text{max}}]$, is chosen to be $[280\,\text{nm}, 350\,\text{nm}]$, and a total efficiency of $\varepsilon = 7.5\%$ is used to take into account the transmission and reflectivity losses, as well as the quantum efficiency of the photo detectors.

The information form the Cherenkov detectors will be also used for PID.

4.3.2.3 EMC scintillator readout

For the electromagnetic calorimeter in the target spectrometer (TSEMC) reasonable properties of $PbWO_4$ crystals at the operational temperature of -25°C are considered. A Gaussian distribution with $\sigma = 1\,\text{MeV}$ is used for the constant electronic noise in the large area avalanche photodiodes (LAAPD). The statistical fluctuations are estimated by 80 photo electrons per MeV produced in the LAAPD. An excess noise factor of 1.38 is used, corresponding to the measurements with the first LAAPD prototype with an internal gain of $M = 50$ [93]. This results in a noise term of $\frac{0.41\%}{\sqrt{E[\text{GeV}]}}$ from photon statistics.

4.3.2.4 Muon detector readout

A parametrized digitization is used for the muon detector, because the layout was still under development when the software was written. The intersections of the particle tracks with the scintillators of the muon detectors are derived from the detector hits provided by the GEANT4 transport code. In the process of matching muon detector hits with reconstructed charged tracks, the uncertainties are dominated by the errors from the extrapolation of the reconstructed tracks to the muon detector, and therefore the finite position resolution of the muon detector is neglected. The algorithm that is used to deduce PID probabilities from the muon detector hits is described in Section 4.4.3.1.

4.4 Reconstruction

4.4.1 Charged particle track reconstruction

4.4.1.1 MVD cluster reconstruction

The MVD provides very precise space-point measurements as a basis for track and vertex reconstruction. For multi-hit clusters, charge weighting between the pixels in the cluster is used to calculate the mean position of the hit. Without using the energy information, the resolution of the position measurement would be

$$\sigma_{geom} = p/\sqrt{12}$$

where p is the pixel size. Using (100×100) μm^2 pixels, the geometric resolution per pixel is $\sigma_{geom} = 28$ μm. For high-momentum particles the hit resolution limits the overall track resolution whereas for low-momentum particles small-angle scattering is the limiting factor.

4.4.1.2 Global track reconstruction

The track provides information about a charged particle's path through space. It contains a collection of hits in the individual tracking subdetectors. For each hit a residual distance with respect to a reference trajectory can be calculated. An idealized pattern recognition program has been used for track-building based on Monte Carlo information, which assigns reconstructed hits to their original tracks. Tracks that contain less than eight detector hits are rejected.

The tracks in the target spectrometer are then fitted with a Kalman Filter algorithm, which considers not only the measurements and their corresponding resolutions but also the effect of the interaction with the detector material, *i.e.* multiple scattering and energy loss. A detailed description of the implementation of the algorithm, which has been adapted from the reconstruction software of the BaBar Collaboration, can be found in Reference [94]. For simplification a constant magnetic field parallel to the z-axis has been assumed in the target spectrometer region.

Multiple scattering and energy loss depend on the mass of the particle. Therefore, the tracks have been refit separately for all five particle hypotheses (e, μ, π, K and p). This results in an adequate accuracy of the reconstructed kinematics assigned to the individual particle species.

4.4.2   Photon reconstruction

In this Thesis, a study of the energy resolution of the BWEMC of $\overline{\mathrm{P}}$ANDA is presented in Chapter 5. The photon reconstruction algorithm is very important for a successful analysis of the BWEMC properties. The method used for the photon reconstruction is explained in the following.

4.4.2.1   Reconstruction algorithm

Photons and electrons entering the electromagnetic calorimeter (EMC) develop electromagnetic showers inside the scintillating material of the detector. Generally, the electromagnetic showers are extended over several scintillator crystals. A contiguous area of crystals containing part of an electromagnetic shower is called a cluster.

The four vector of the initial photon or electron can be determined by the energy deposited and the locations of the scintillator crystals in a cluster. The EMC reconstruction software used here is based in the cluster finding and bump-splitting algorithms developed by the BaBar experiment [95, 96].

The first step of the cluster reconstruction algorithm is finding a contiguous area of scintillator crystals with energy deposition. The process starts finding the crystal with the highest energy deposition and is adding contiguous neighbors if the energy deposited on them is above a certain threshold E_{xtl}. Finally, if the total energy deposit in the contiguous area is above a second threshold E_{cl} the cluster gets accepted.

A cluster can be formed by more than one particle if the angular distances between them are small. In this case the cluster has to be subdivided into regions which can be associated with the individual particles. These regions are called bumps, and a new algorithm to separate the clusters in possible different bumps is needed in this step. This procedure is called the *bump splitting*. A bump is defined by a local maximum inside the cluster: The energy deposit of one scintillator crystal E_{local} must be above E_{max}, and all the neighbor crystals must have smaller energy depositions. In addition the highest energy $E_{N_{max}}$ of any of the N neighboring crystals must fulfill

$$0.5\,(N-2.5) > E_{N_{max}}\,/\,E_{local} \qquad (4.1)$$

The total cluster energy is then shared between the bumps, taking into account the shower shape of the cluster. For this step an iterative algorithm is used, which assigns a weight w_i to each scintillator crystal, so that the bump energy is defined as $E_b = \sum_i w_i E_i$, in which E_i represents the energy deposited in the i-th crystal and the sum runs over all crystals in the cluster. The crystal

	TSEMC	FSEMC
E_{xtl}	3 MeV	8 MeV
E_{cl}	10 MeV	15 MeV
E_{max}	20 MeV	10 MeV

Table 4.1: Reconstruction thresholds for the electromagnetic calorimeter in the target spectrometer (TSEMC) and the electromagnetic calorimeter in the forward spectrometer (FSEMC).

weight for each bump is calculated as

$$w_i = \frac{E_i \exp(-2.5\, r_i / r_m)}{\sum_j E_j \exp(-2.5\, r_j / r_m)} \tag{4.2}$$

where r_m is the Molière radius of the scintillator material, r_i and r_j are the distance of the i-th and j-th crystal to the center of the bump, respectively, and the index j runs over all crystals. The procedure is repeated until convergence. The center position is always determined from the weights of the previous iteration, and convergence is reached when the bump center stays stable within a tolerance of 1 mm.

The spatial position of a bump is calculated via a center-of-gravity method. The radial energy distribution, originating from a photon, decreases exponentially. Therefore, a logarithmic weighting with

$$W_i = \max\left[0,\, A(E_b) + \ln(E_i/E_b)\right] \tag{4.3}$$

was chosen, where only crystals with positive weights are used. The energy-dependent factor $A(E_b)$ varies between 2.1 for the lowest and 3.6 for the highest photon energies.

4.4.2.2   Reconstruction thresholds

To detect low energetic photons and to achieve a good energy resolution, the thresholds should be set as low as possible. On the other hand, the thresholds must be sufficiently high to suppress the electronic noise. The single crystal threshold was set to 3 MeV of deposited energy, corresponding to the energy equivalent of 3σ of the electronic noise (see 4.3.2.3). All reconstruction thresholds for the electromagnetic calorimeter in the target spectrometer as well as for the electromagnetic calorimeter in the forward spectrometer are listed in Table 4.1.

4.4.2.3 Leakage corrections

The sum of the energy deposited in the scintillator material of the calorimeters is less than the actual energy of the incident photon. This is due to energy deposition in the material between the different crystals.

The reconstructed energy of the photon in the electromagnetic calorimeter in the target spectrometer is expressed as a product of the measured total energy deposited and a correction function which depends logarithmically on the energy and, due to the geometry of the EMC, also on the polar angle. The correction function

$$
\begin{aligned}
\mathrm{f}(\ln E, \theta) = \exp(a_0 + a_1 \ln E + a_2 \ln^2 E + a_3 \ln^3 E \\
+ a_4 \cos(\theta) + a_5 \cos^2(\theta) + a_6 \cos^3(\theta) \\
+ a_7 \cos^4(\theta) + a_8 \cos^5(\theta) \\
+ a_9 \ln E \cos(\theta))
\end{aligned}
$$

has been calculated using Monte Carlo simulations with single photons. The corrected photon energy is then $E_{\gamma, cor} = E \cdot \mathrm{f}(\ln E, \theta)$.

The energy leakage in the electromagnetic calorimeter in the forward spectrometer is driven by the large amount of absorber material between the scintillating crystals and is only slightly caused by the geometry. Therefore, the considered correction depends only on the collected energy.

4.4.3 Charged PID

Good PID for charged hadrons and leptons plays an essential role for $\overline{\mathrm{P}}$ANDA and must be guaranteed over a large momentum range from 200 MeV/c up to approximately 10 GeV/c. Of special interest for this Thesis is the separation between electrons and pions. Several subdetectors provide useful PID information for specific particle species and momenta. While energy-loss measurements within the trackers provide good criteria differentiation between the different particle types below 1 GeV/c, the DIRC detector is the most suitable device for the identification of particles with momenta above the Cherenkov threshold. Moreover, in combination with the tracking detectors, the EMC is the most powerful detector for an efficient and clean electron identification, and the Muon detector is designed for the separation of muons from the other particle species. The best PID performance however can be obtained by taking into consideration all available information of all subdetectors.

The PID software is divided into two stages. In the first stage the recognition is done for each detector individually, so that finally probabilities for all five particle hypotheses (e, μ, π, K and p) are provided. The probabilities are

normalized uniquely by assuming the same fluxes for each particle species. In the second stage the global PID combines this information by applying a standard likelihood method. Based on this can be used flexible tools which allow an optimization of efficiency and purity up to the required values.

4.4.3.1 Subdetector PID

dE/dx measurements

The energy loss of particles in thin layers of material directly provides dE/dx. The Bethe-Bloch formula shows that for a given momentum, particles of different types have different specific energy losses, dE/dx. This property can be used for PID. The method however suffers from two limitations. First of all, a plot of dE/dx vs. p has crossing points where there is no possibility to disentangle particle types. Secondly, the distribution of the specific energy loss displays a long tail which constitutes a limitation to the separation, especially when large differences exist between the different particle yields. Various methods have been worked out to avoid this second limitation. In $\overline{P}ANDA$, two detectors will give access to dE/dx, the MVD, and the STT.

PID with the MVD

Although the number of reconstructed MVD hits per track is limited to 4 in the barrel section and 5-6 in the forward domain the energy loss information provided by the readout electronics can be used as part of the PID decision. The ability of separating different particle species relies on an accurate energy loss information and a good knowledge of the track position with respect to the sensors. Figure 4.1 shows the calculated energy loss versus particle momentum for different particle types in the MVD. Separation is possible only for protons (upper band) and kaons (middle) from the lowest band which is a superposition of pions, muons and electrons. The width of the individual bands depends on the energy-loss distribution which varies with momentum.

PID with the STT

The energy loss of particles through thin layers of gas provides better information for PID at large momenta than the MVD detector. However, when thicknesses as low as a few millimeters of gas are considered, the fluctuations resulting from the relatively low number of primary collisions (less than 100 on a 1 cm Ar path-length) give rise to an extended Landau tail in the energy loss distribution. To prevent this phenomenon which could result into a dramatic reduction of PID capabilities, truncation methods associated with different averaging procedures are often used. The truncated arithmetic mean has been used in
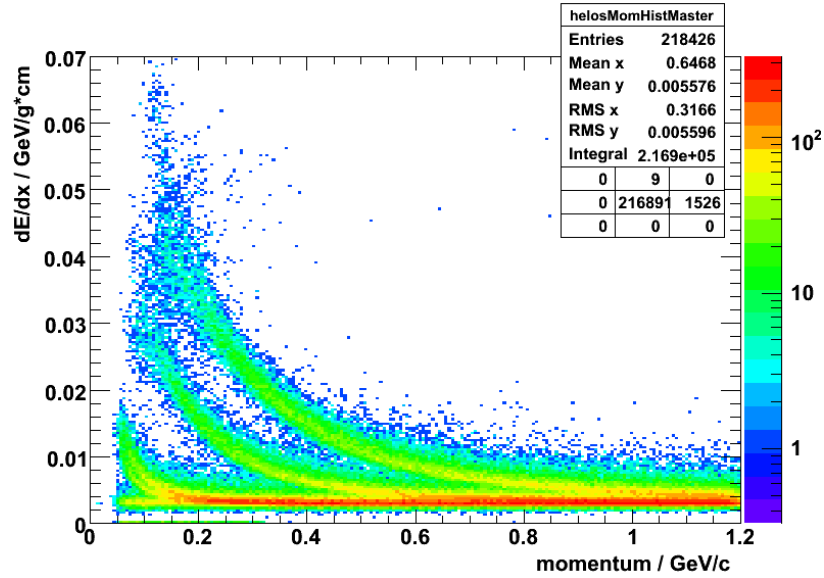
Figure 4.1: dE/dx information from the MVD versus track momentum for protons (upper band), kaons (middle) and pions/muons/electrons (lower).

the framework of $\overline{\text{P}}$ANDA. Moreover, because straw tubes are cylindrical detectors, a path length determination is necessary to calculate dE/dx. A transverse resolution of 150 μm was assumed. A truncation parameter of 70, corresponding to keeping 70 % of the smallest energy loss values, was found to be the best compromise between the resolution defined by the Gaussian fit and the tail still remaining after truncation. For a given triplet (p, θ, dE/dx_{trunc}), five prior probabilities are calculated using the parameters of the Gaussians (μ_i, σ_i, $i = e$, μ, π, K and p), properly normalized. To take into account the role of possible non-Gaussian tails, a lower limit on the likelihood was set to 1%. These likelihoods can then be directly combined with the ones from the other detectors to calculate a global likelihood.

Whereas an efficiency above 98% is observed for electrons (see Figure 4.2), the contamination rate, that is the probability for another type of particle (μ, π, K and p) to be identified as an electron varies between 1% and 16%. One should. however, note that these values are averaged over the polar angle: at forward angles, the contamination increases as the result of the strong decrease of the number of hits in the straw tubes.

The PID information provided by the STT detector is of high importance for the separation of pions and electrons in the studies presented in this Thesis.
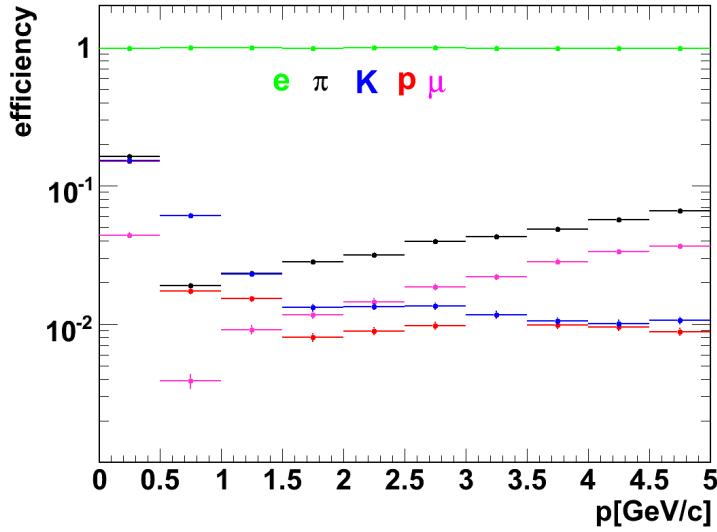
Figure 4.2: PID efficiency for electrons in the momentum range between 0.2 GeV/c and 10 GeV/c and the contamination rates for the four other particle types, averaged over the whole STT angular range.

PID with the DIRC

Charged tracks are considered if they produce Cherenkov light in the DIRC detector. Based on the reconstructed momentum, the reconstructed path length of the particle in the quartz radiator and the particle hypothesis, the expected Cherenkov angles and its errors are estimated. Compared with the measured Cherenkov angle the likelihood and significance levels for each particle species are calculated. While below the Cherenkov threshold of approximately 500 MeV/c almost no kaons can be identified, the efficiency above the threshold is more than 80% over the whole momentum range up to 5 GeV/c. The fraction of pions misidentified as kaons is substantially less than 10^{-3} for momenta below 3 GeV/c and increases up to 10% for 5 GeV/c.

Electron PID with the EMC

The footprints of deposited energy in the calorimeter differ distinctively for electrons, muons and hadrons. While muons and hadrons in general lose only a small fraction of their kinetic energy by ionization processes, electrons deposit their complete energy in an electromagnetic shower. The ratio of the measured energy deposited in the calorimeter to the reconstructed track momentum (E/p) will be approximately unity. Due to the hadronic interactions, hadrons may also

have a higher E/p ratio than expected from ionization. Figure 4.3 shows the reconstructed E/p fraction for electrons and pions as a function of the momentum.
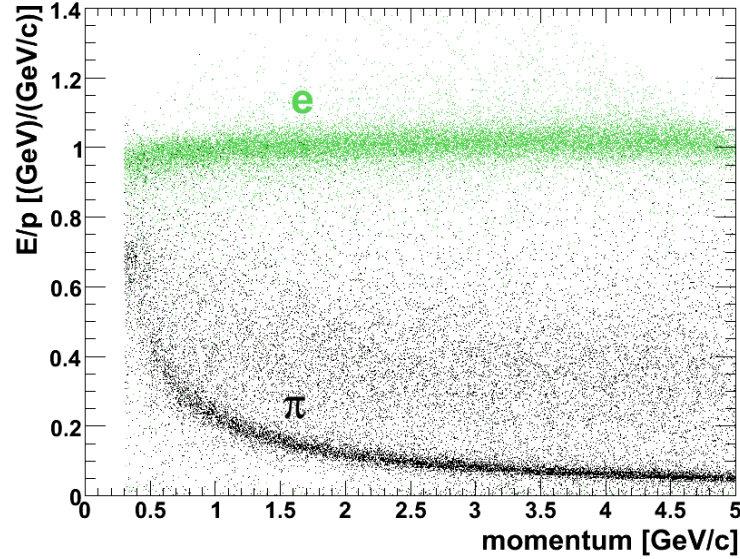
Figure 4.3: E/p in the EMC versus track momentum for electrons (green) and pions (black) in the momentum range between 0.3 GeV/c and 5 GeV/c.

Furthermore, the shower shape of a cluster is helpful to distinguish between electrons, muons and hadrons. Since the chosen size of the scintillator crystals corresponds to the Molière radius of the material, the largest fraction of an electromagnetic shower originating from an electron is contained in just a few crystals. Instead, a hadronic shower with a similar energy deposit is less concentrated. These differences are reflected in the shower shape of the cluster, which can be characterized by the following properties:

- E_1/E_9 which is the ratio of the energy deposited in the central scintillator crystal and in the 3×3 crystal array containing the central crystal and the first innermost ring. Also the ratio between E_9 and the energy deposit in the 5×5 crystal array E_{25} is useful for electron identification.

- The lateral moment of the cluster defined by

$$\mathrm{mom}_{LAT} = \sum_{i=3}^{n} E_i r_i^2 / (\sum_{i=3}^{n} E_i r_i^2 + E_1 r_0^2 + E_2 r_0^2)$$

  with

  – n = number of crystals associated to the shower

- – E_i = deposited energy in the i-th crystal with $E_1 \geq E_2 \geq ... \geq E_n$
- – r_i = lateral distance between the central and the i-th crystal
- – r_0 = the average distance between two crystals.

- A set of Zernike moments [97],

$$U_n^m(\rho, \varphi) = R_n^m(\rho)\left(\cos(m\varphi) - i\sin(m\varphi)\right), \qquad (4.4)$$

with

$$R_n^m(\rho) = \begin{cases} \sum_{k=0}^{\frac{1}{2}(n-m)} \frac{(-1)^k(n-k)!}{k!\left(\frac{1}{2}(n+m)-k\right)!\cdot\left(\frac{1}{2}(n-m)-k\right)!}\rho^{n-2k} & \text{for } n-m \text{ even} \\ 0 & \text{for } n-m \text{ odd} \end{cases}$$

$$(4.5)$$

describe the energy distribution within a cluster by radial and angular dependent polynomials. Specially the Zernike moments (3 1),

$$Re(U_1^3) = \sum_i^{N_{crystals}} \frac{E_i}{E_{tot}} \cdot (3 \cdot r_i^3 - 2 \cdot r_i) \cdot \cos(\phi_i), \qquad (4.6)$$

$$Im(U_1^3) = - \sum_i^{N_{crystals}} \frac{E_i}{E_{tot}} \cdot (3 \cdot r_i^3 - 2 \cdot r_i) \cdot \sin(\phi_i), \qquad (4.7)$$

and (4 2),

$$Re(U_2^4) = \sum_i^{N_{crystals}} \frac{E_i}{E_{tot}} \cdot (4 \cdot r_i^4 - 3 \cdot r_i^2) \cdot \cos(2 \cdot \phi_i), \qquad (4.8)$$

$$Im(U_2^4) = - \sum_i^{N_{crystals}} \frac{E_i}{E_{tot}} \cdot (4 \cdot r_i^4 - 3 \cdot r_i^2) \cdot \sin(2 \cdot \phi_i), \qquad (4.9)$$

are used for the separation of electrons from other kind of particles.

An example is given in 4.4, where the Zernike moment 31 is depicted for each particle type.

A neural network is also used to combine all the information provided by the different EMC measured variables. The neural network is able to assign different probabilities to the different particle species which have been considered (e, p, k, μ and π).

For the global PID a correlation between the network output and the PID likelihood of the EMC has been calculated. Figure 4.5 shows the electron identification efficiency and contamination rate as a function of momentum achieved by requiring an electron likelihood fraction of the EMC of more than 95%. For momenta above 1 GeV/c one can see that the electron efficiency is greater than 98% while the contamination by other particles is substantially less than 1%. For momenta below 1 GeV/c, the electron identification based solely on the EMC information has a poor efficiency and an insufficient purity.
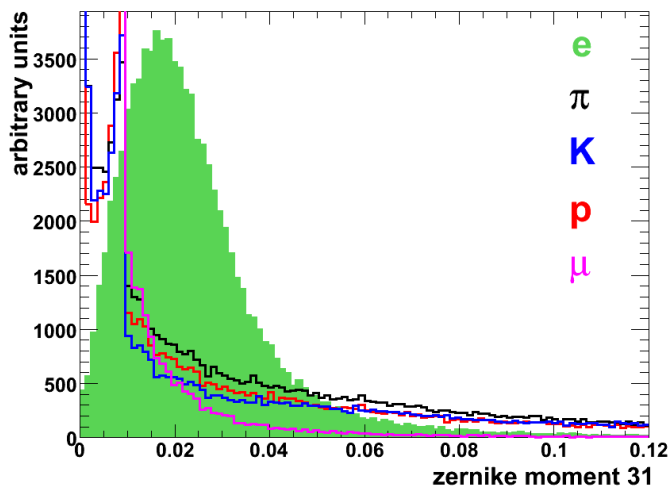
Figure 4.4: Zernike moment number 31 for electrons, muons and hadrons.

PID with the muon detector

The PID for the muon detector is based on an algorithm that quantifies for each reconstructed charged track the compatibility with the muon hypothesis. It propagates the charged particles from the tracking volume outward through the neighboring detectors like the DIRC and the EMC and finally through the iron yoke, where the scintillator layers of the muon device are located. This procedure takes into account the parameters of the global tracking and the magnetic field, as well as the muon energy loss in the material and the effects of multiple scattering. Then the extrapolated intersection points with the scintillators are compared with the detected muon hit positions. If the distance between the expected and the detected hit is smaller than 12 cm, which is 4σ of the corresponding distribution, the muon hit will be associated with the corresponding charged track. Based on the numbers of associated and expected muon hits, the likelihoods for each particle type are estimated.

The procedure results in good muon identification for momenta above approximately 1 GeV/c. While electrons can be completely suppressed, a contamination fraction of a few percent is present for hadrons.

4.4.3.2 Global PID

The global PID, which combines the relevant information of all subdetectors associated with one track, has been realized with a standard likelihood method. Based on the likelihoods obtained by each individual subdetector the probability for a track originating from a specific particle type $P(k)$ is evaluated
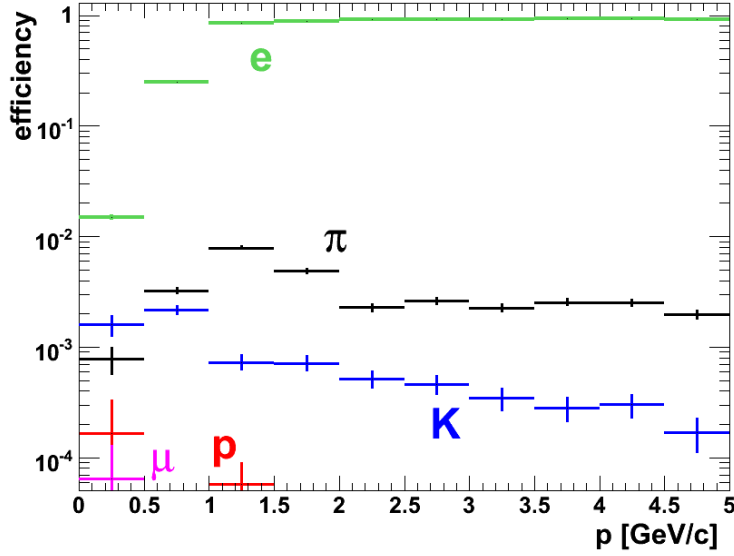
Figure 4.5: The electron identification efficiency and contamination rates for muons, pions, kaons, and protons in different momentum ranges using the combined information provided by the neural network in the EMC.

from the likelihoods as follows:

$$P(k) = \frac{\prod_i P_i(k)}{\sum_j \prod_i P_i(j)}, \qquad (4.10)$$

where the product with index i runs over all considered subdetectors and the sum with index j over the five particle types (e, μ, π, K and p).

Due to the variety of requirements imposed by the different benchmark channels, various kinds of particle-candidate lists for different selection criteria on the global likelihood are provided for the analysis (see Table 4.2). The usage of the so called Very Loose and Loose candidate lists yields good efficiencies, and the Tight and Very Tight lists are optimized to obtain a good purity with efficient background rejection.

4.5 Physics analysis

The event data used for physics analysis is structured in three levels of detail:

- The small TAG level contains brief event summary data.

particle	candidate list			
	Very Loose	Loose	Tight	Very Tight
e	20%	85%	99%	99.8%
μ	20%	45%	70%	85%
π	20%	30%	55%	70%
K	20%	30%	55%	70%
p	20%	30%	55%	70%

Table 4.2: Minimal values for the global likelihood (see Equation 4.10), for the corresponding particle types for four selection scenarios.

- The analysis object cata (AOD) consists of PID lists of particle candidates, and, in the case of Monte Carlo data, also of Monte Carlo truth data. Most analysis jobs run on AOD data.

- The event summary data (ESD), which holds all reconstruction objects down to the detector hits which are necessary to redo the track and neutral particle reconstruction, and to rebuild the PID information. The detailed ESD data are needed by very few analysis jobs.

This event data design directly supports the typical analysis tasks, which usually can be subdivided into three steps:

- A fast event preselection that uses just the TAG data.

- An event reconstruction and refined event selection step using the AOD data. In the event reconstruction, decay trees are built up, and geometrical and kinematic fits are applied to them. Cuts on the fit probabilities, invariant masses or kinematic properties of the candidates are common to refine the event selection in this step. The output of this analysis step is usually n-tuple data.

- In the last analysis step the event selection can be further refined by applying cuts on the n-tuple data. Histogram fits or partial wave analyses can be performed on the final set of events.

4.5.1   Kinematic fit

Once a first selection of the event candidates is done using the AOD data, a kinematic fit can be performed to improve the quality of the data. The kinematic fit assumes that the measured variables (for example, the energy and momentum of a track) are not completely independent of each other, but they are connected

by the initial constraints defined by the hypothesis selected for the assumed decay (for example, the mass of the particles). Then new values for the measured variables within the resolution of the initial measurement are calculated. A confidence level (*CL*) is then calculated, which gives an idea of the goodness of the hypothesis used for the fit. A general description of the kinematic fit is described in the following [98].

Considering the vector of measured variables $\vec{x} = (x_1, ..., x_n)$ and the initial constraints $a_k(\vec{x} + \vec{\delta x}) = 0$, the kinematic fit will look for the corrections δx_i of the measured values x_i using the minimum quadratic method. Therfore the equation,

$$L = \vec{\delta x}^T V^{-1} \vec{\delta x} + 2\vec{\lambda}^T \vec{a}(\vec{x} + \vec{\delta x}) = \min \qquad (4.11)$$

has to be minnimized. Here V is the symmetric $n \times n$ covariant matrix of the n measured variables, λ_k are the Lagrange multipliers associated to the m initial constraints ($k = 1, ..., m$) and $\vec{a}(\vec{x} + \vec{\delta x}) = (a_1(\vec{x} + \vec{\delta x}), ..., a_m(\vec{x} + \vec{\delta x}))$. This condition is fulfilled when the total derivative of L is zero,

$$dL = 2\vec{\delta x}^T V^{-1} d(\vec{\delta x}) + 2\vec{\lambda}^T \frac{\partial \vec{a}(\vec{x} + \vec{\delta x})}{\partial(\vec{\delta x})} d(\vec{\delta x}) = 0. \qquad (4.12)$$

Assuming that the dependence of the initial constraints with the measured values is linear,

$$\vec{a}(\vec{x} + \vec{\delta x}) = \vec{a}(\vec{x}) + \frac{\partial \vec{a}(\vec{x})}{\partial \vec{x}} \vec{\delta x} = \vec{0}, \qquad (4.13)$$

we have

$$dL = 2\vec{\delta x}^T V^{-1} d(\vec{\delta x}) + 2\vec{\lambda}^T \frac{\partial \vec{a}(\vec{x})}{\partial \vec{x}} d(\vec{\delta x}) = 0. \qquad (4.14)$$

Equations (4.13) and (4.14) can be written in a compact way as

$$\begin{pmatrix} V^{-1} & \frac{\partial \vec{a}(\vec{x})^T}{\partial \vec{x}} \\ \frac{\partial \vec{a}(\vec{x})}{\partial(\vec{x})} & 0 \end{pmatrix} \begin{pmatrix} \vec{\delta x} \\ \vec{\lambda} \end{pmatrix} = \begin{pmatrix} \vec{0} \\ -\vec{a}(\vec{x}) \end{pmatrix}. \qquad (4.15)$$

This defines a system of $n + m$ equations from which the values of $\delta x_1, ..., \delta x_n$ and $\lambda_1, ..., \lambda_m$ can be calculated. The new fitted variables $x_1 + \delta x_1, ..., x_n + \delta x_n$ exhibit a new covariant matrix, V_{new} that is calculated from the propagation of errors,

$$V_{\text{new}}^{-1} = V^{-1} - V^{-1} \frac{\vec{a}(\vec{x})^T}{\partial(\vec{x})} \left(\frac{\vec{a}(\vec{x})}{\partial(\vec{x})} V^{-1} \frac{\vec{a}(\vec{x})^T}{\partial(\vec{x})} \right)^{-1} \frac{\vec{a}(\vec{x})}{\partial(\vec{x})} V^{-1}. \qquad (4.16)$$

The quadratic deviation is then,

$$\chi^2 = \vec{\delta x}^T V^{-1} \vec{\delta x}. \qquad (4.17)$$

It gives a measurement of the goodness of the fit performed with the chosen hypothesis. It indicates how much the errors of the measured values have to be changed in order to fullfil the initial constraints of Equation (4.13). In practice one often uses an overall confidence level (*CL*), defined as

$$CL = \int_{\chi^2}^{\infty} \frac{x^{m/2-1}e^{-x/2}}{2^{m/2}\Gamma(m/2)} dx. \tag{4.18}$$

The confidence level takes a value between 0 and 1. For the ideal case in which the fit hypothesis is working perfectly, the confidence level takes the value 1. If the hypothesis of the fit can not be fullfiled, then the confidence level is equal to zero.

5

Energy resolution and efficiency studies for the backward endcap calorimeter

The backward endcap of the electromagnetic calorimeter (BWEMC) is an important part of the $\overline{\mathsf{P}}$ANDA detector. It is needed for the detection of low-energy electrons and photons emitted at backward angles. For the study of some processes of interest the detection of electrons and photons at backward angles is essential. For example for the study of the validity of the transition distribution amplitudes (TDA) approach for the calculation of the cross section $\bar{p}p \rightarrow e^+e^-\pi^0$ at zero value of the π^0 transverse momentum ($\Delta_{T_{\pi^0}=0}$), the BWEMC will play a crucial role.

The material budget of dead material introduced by other detectors in front of the calorimeter, such as the supply and cooling systems of the micro vertex detector (MVD) or the straw tube tracker (STT), could worsen the properties of the BWEMC. A full analysis of the effect of this dead material was necessary. The study of the efficiency and energy resolution of this subdetector of $\overline{\mathsf{P}}$ANDA is presented in this Chapter.

5.1 Simulation characteristics

The whole geometry of $\overline{\mathsf{P}}$ANDA was described in Chapter 3. This geometry is basically the one that has been implemented in the software for the simulations. However, for the studies presented in this Chapter, slight modifications

have been made in different steps to see how the properties of the BWEMC change. The BWEMC was implemented in the code using standard extensible markup language (XML) and GEANT4. A macro was written to place the 540 PWO-II straight crystals (24.4×24.4 mm and 200 mm long) in a crown around the beam pipe with an inner radius of 182 mm, an outer radius of 406 mm, and an upstream location 504 mm from the target. Each crystal was also wrapped in a thin layer of carbon fiber that plays the role of the crystal holders [93]. Also a thin layer of air was introduced between the crystals and the carbon fiber. The total angular coverage goes from $\sim 146°$ to $\sim 167°$. The beam pipe, the STT and the MVD are taken into account for all the simulations.

Figure 5.1 shows a front view of the BWEMC as it is implemented in the software.
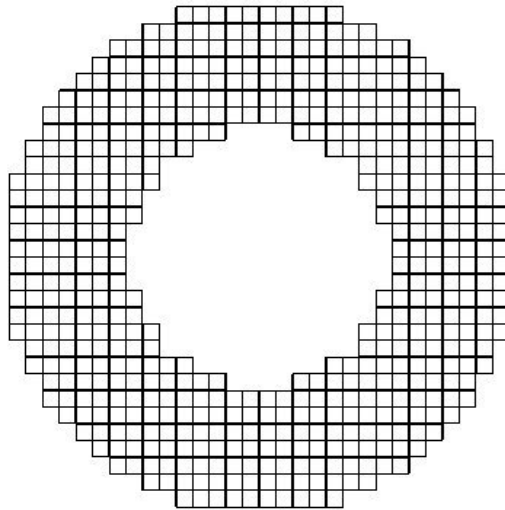
Figure 5.1: Front schematic view of the backward calorimeter geometry used for the simulation. The 540 straight PWO crystals are arranged in a crown shape around the beam pipe of the $\overline{\mathrm{P}}$ANDA experiment.

5.1.1   Study of the STT dead material

The influence of the dead material introduced by the STT on the energy resolution and efficiency of the BWEMC was studied first. For the simulations in this step, three slightly different geometries were used. In the first geometry (STT-0), no additional dead material was introduced to the setup of $\overline{\mathrm{P}}$ANDA. The BWEMC, the STT and the MVD were used as described in the previous Section without any further modification. In the second geometry (STT-Low), a thin layer of aluminum with a thickness of 2 cm was placed behind the STT, following its border shape, to simulate the effect of the electronic and cabling

systems. In the third geometry (STT-High), a thicker aluminum layer, 4 cm, with the same shape was used. The named two scenarios including dead material were chosen as possible ones because at the time the simulations were done no quantitative estimation of the dead material introduced by the STT electronics and cabling systems was available. However, the chosen thicknesses represent already a conservative selection for the simulations.

Figure 5.2 shows a schematic side view of the calorimeter and the 4 cm aluminum layer placed behind the STT. This Figure corresponds to the geometry named STT-High. One can see that particles emitted at $\theta = 160°$ or above could interact with the introduced dead material before reaching the BWEMC.
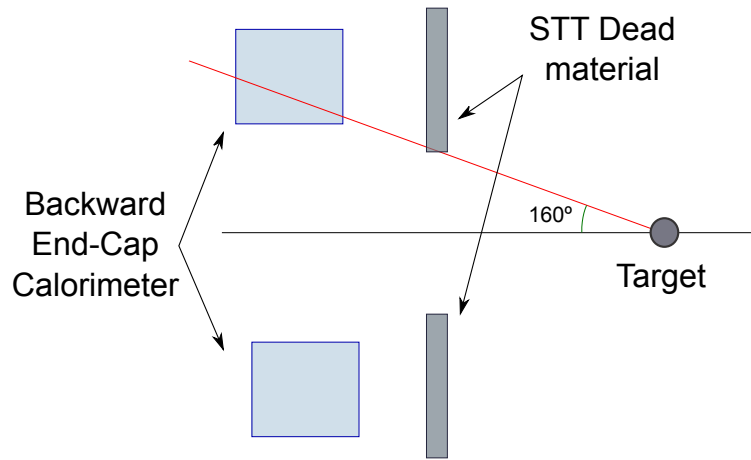
Figure 5.2: Side schematic view of the BWEMC and the STT dead material positions with respect to the target. The thickness of the dead material in this cases corresponds to 4 cm (Geometry case STT-High).

E (MeV)	θ	ϕ
30	145°	
100	150°	1°
250	155°	22.5°
500	160°	45°
700	165°	

Table 5.1: E, θ and ϕ photon parameters for the simulations. Simulations with 50 000 photons have been done for each possible combination of E, θ and ϕ using three different geometries including dead material.

For each possible geometry were done simulations with 50 000 single photons with all possible combinations of energies and angles shown in Table 5.1. That makes 75 different simulation setups in total (*i.e.* 3 geometries × 5 energies × 5 θ angles × 3 ϕ angles).

5.1.2 Study of the MVD dead material

To study the influence of the MVD on the energy resolution and efficiency of the BWEMC on full $\overline{P}$ANDA performance, further simulations including additional geometrical elements were done. These new elements were designed to simulate the cabling and support systems introduced by the MVD detector between the interaction region and the BWEMC. The dead material introduced by the STT detector, presented in the previous Section, was taken into account also in these studies by keeping in the geometry file the 2 cm thick aluminum layer considered in the geometry case with lower dead material (STT-Low). In addition, the shapes and positions of the elements of dead material introduced by the MVD were implemented in the code modeling them from the studies done by T. Würschig for PandaROOT [99]. In Figure 5.3 one can see that the angular regions with the most dead material introduced by the MVD are concentrated between $\theta = 145°$ and $\theta = 155°$. This dead material introduces 1.5 to 2.0 radiation lengths in very localized spots.
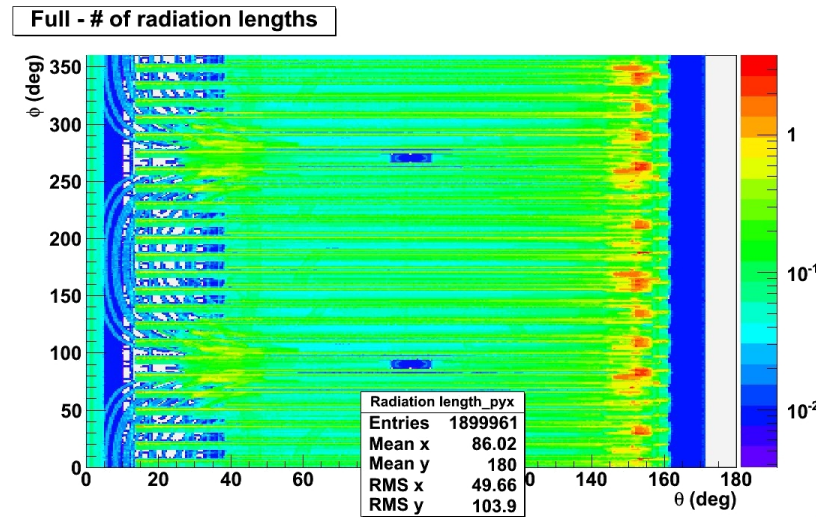
Figure 5.3: MVD dead material measured in radiation lengths from Reference [99]. These data were used to insert the dead material introduced by the MVD into the simulations. See text for more information.

Copper tapered blocks (see Figures 5.4a and 5.4b) with equivalent radiation lengths and the same angular coverage as shown by Figure 5.3 were designed using a CAD program. However, the implementation of this geometry was very difficult to do with the existing software. Therefore, the shapes designed in CAD were measured and squared boxes with interpolated dimensions were placed instead in the same positions. In the geometry file were implemented as a result of this interpolation 10 boxes $(21.73 \times 21.73 \times 22)$ mm^3 and 4 boxes $(14.5 \times 14.5 \times 22)$ mm^3 corresponding to $X_0 \sim 1.8$ in each case. Figures 5.4c and 5.4d show how these blocks look in the simulation. In addition, an

(a) Estimation front

(b) Estimation side

(c) Interpolation front

(d) Interpolation side
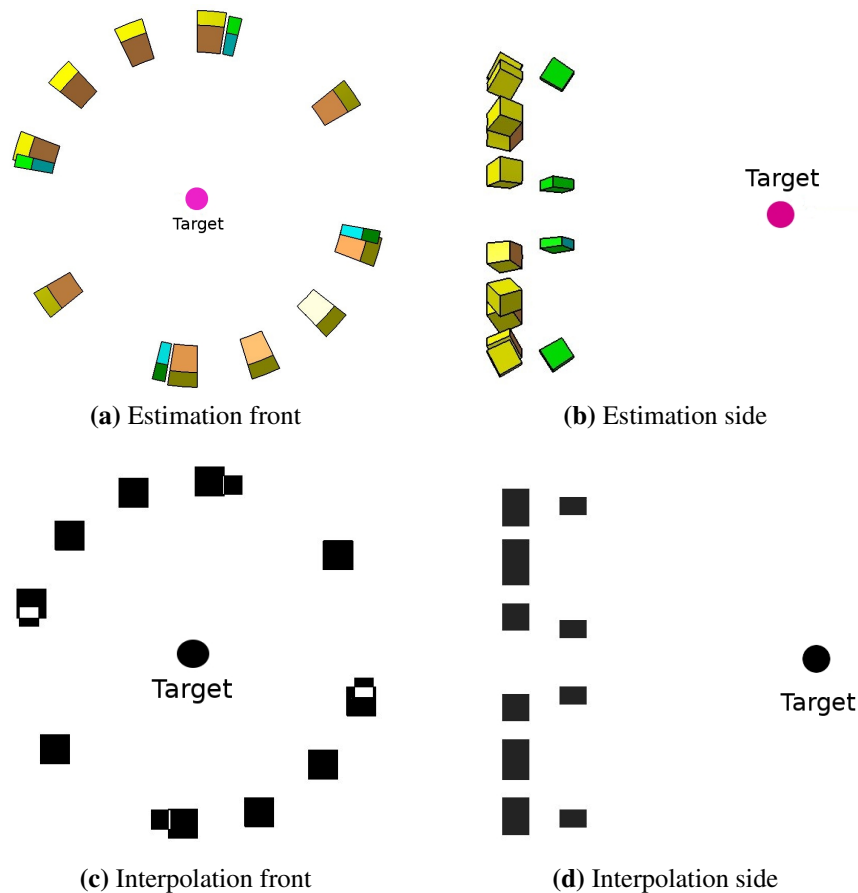
Figure 5.4: Dead material introduced by the cabling and support systems of the MVD. Left, view from the target position towards backward angles. Right, side view with the target position on the right. Above, a representation of the blocks designed using a CAD program. These blocks are build using the information in Figure 5.3. Below, the interpolated blocks for the implementation in the geometry file in the software. The dimensions have been calculated as an interpolation of the dimensions of the blocks designed in CAD.

aluminum cylinder $2\,\mathrm{cm}$ thick was placed around the beam pipe introducing a radiation length of approximately $X_0 \sim 0.5$ between the target and the BWEMC. A 3D cut view of the setup of the BWEMC and the dead material introduced by the MVD (blocks and cylinder) can be seen in Figure 5.5, where also the three paths chosen for the simulations with this geometry are also shown. Although the disc simulating the dead material of the STT is not shown in the Figure, it is taken into account for the simulations.

The three paths chosen to study the influence of the dead material introduced by MVD on the energy resolution and efficiency of the BWEMC were

selected to hit either one of the boxes implemented in the software or the cylinder. Studying only these three cases and taking into account the symmetry of the geometry one can extrapolate the results to other areas of the BWEMC. For the simulations 50 000 photons at three different energies (30 MeV, 250 MeV and 700 MeV) were generated at three combinations of θ and φ angles:

- First at θ = 147.5° and φ = 78°, where one of the small boxes of dead material and the cylinder are hit by the photons (Figure 5.5a). From the Figure one can also see that the photons traversing the dead material reach the calorimeter only on the border. The energy of these photons will not be correctly measured because the electromagnetic shower cannot take place fully inside the detector volume.

- Second at θ = 152.5° and φ = 34.5°, where one of the big boxes and the cylinder are hit by the photons (Figure 5.5b). Here the reconstruction of the photons reaching the calorimeter is expected to be better, because the path that they follow is hitting the calorimeter in the middle. The electromagnetic shower is fully contained inside the detector.

- Third at θ = 152.5° and φ = 45°, where only the thin cylinder is hit by the photons (Figure 5.5c). Here more photons are expected to reach the calorimeter because the amount of dead material they have to traverse is lower. The reconstruction of their energy is also expected to be good, because their paths are again fully contained inside the calorimeter volume.
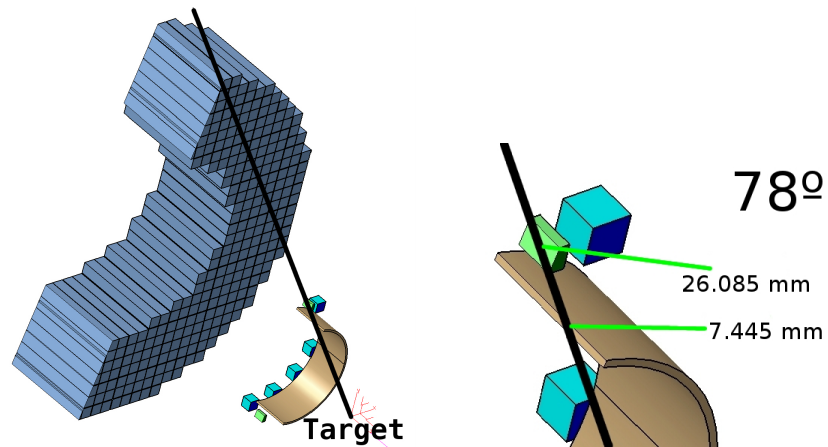
(a) Path followed by photons emitted at $\theta = 147.5°$ and $\phi = 78°$.
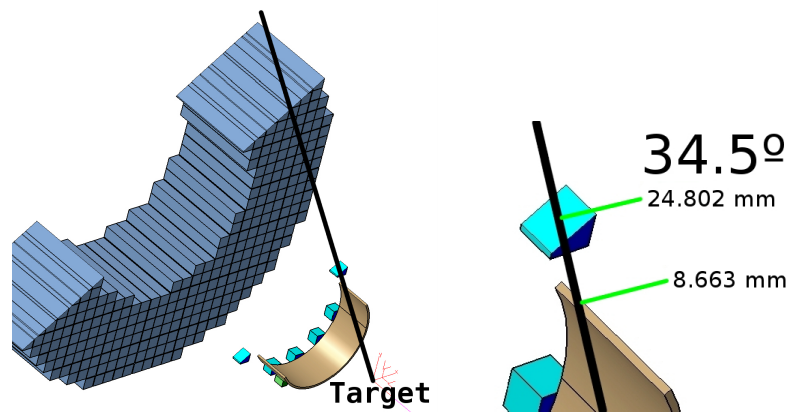
(b) Path followed by photons emitted at $\theta = 152.5°$ and $\phi = 34.5°$.
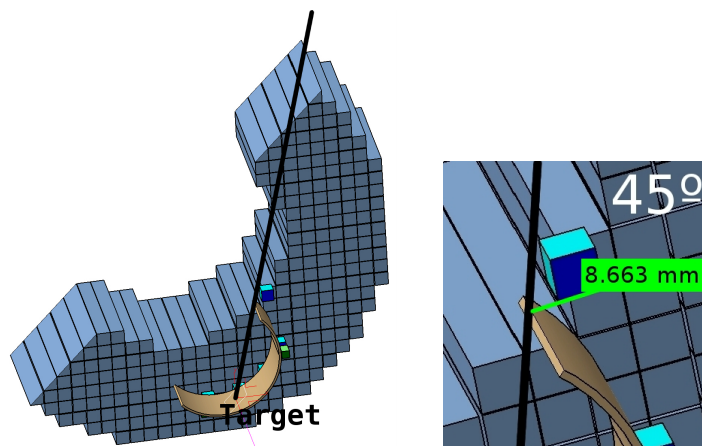
(c) Path followed by photons emitted at $\theta = 152.5°$ and $\phi = 45°$.

Figure 5.5: Photon paths chosen for the simulations in the study of the MVD dead material influence on the BWEMC.

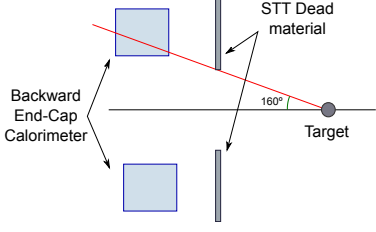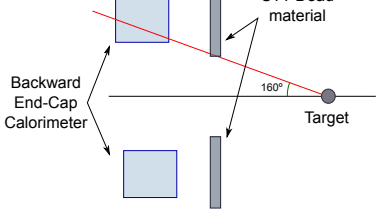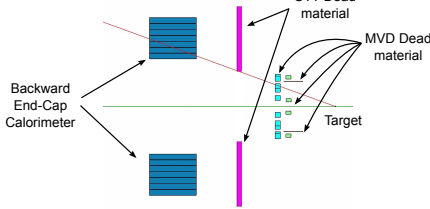In Table 5.2 one can see a summary of the different geometries used for the simulations presented in this Chapter.
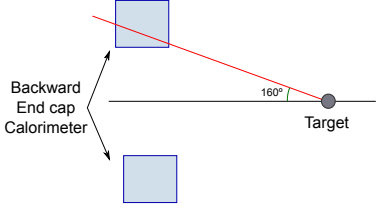
Geometry	Description	Drawing
STT-0	Only the $\overline{\text{P}}$ANDA geometry	
STT-Low	$\overline{\text{P}}$ANDA geometry + 2cm Aluminum disc behind the STT to simulate its electronics	
STT-High	$\overline{\text{P}}$ANDA geometry + 4cm Aluminum disc behind the STT to simulate its electronics	
MVD	$\overline{\text{P}}$ANDA geometry + STT-Low + 4 small blocks + 10 big blocks + cylinder to simulate the cabling and support systems of the MVD	

Table 5.2: Geometries for the study of the influence of the dead material introduced by other subdetectors of $\overline{\text{P}}$ANDA on the energy resolution and the efficiency of the BWEMC.

5.1.3 Energy resolution and efficiency in the whole BWEMC

As a last step, an energy resolution map and an efficiency map were done for one half-quarter of the BWEMC using different photon energies. For that, simulations were done with 50 000 photons with energies from 30 MeV to 700 MeV emitted at angles $150° < \theta < 163.5°$ and $314° < \phi < 359°$.

(a) Volume of the BWEMC covered by the simulations, θ limits in orange, φ limits in brown

(b) Front view of the area covered by the simulations, showing the maximum and minimum φ values.

(c) Lateral cut of the BWEMC and dead material showing the maximum and minimum θ values.
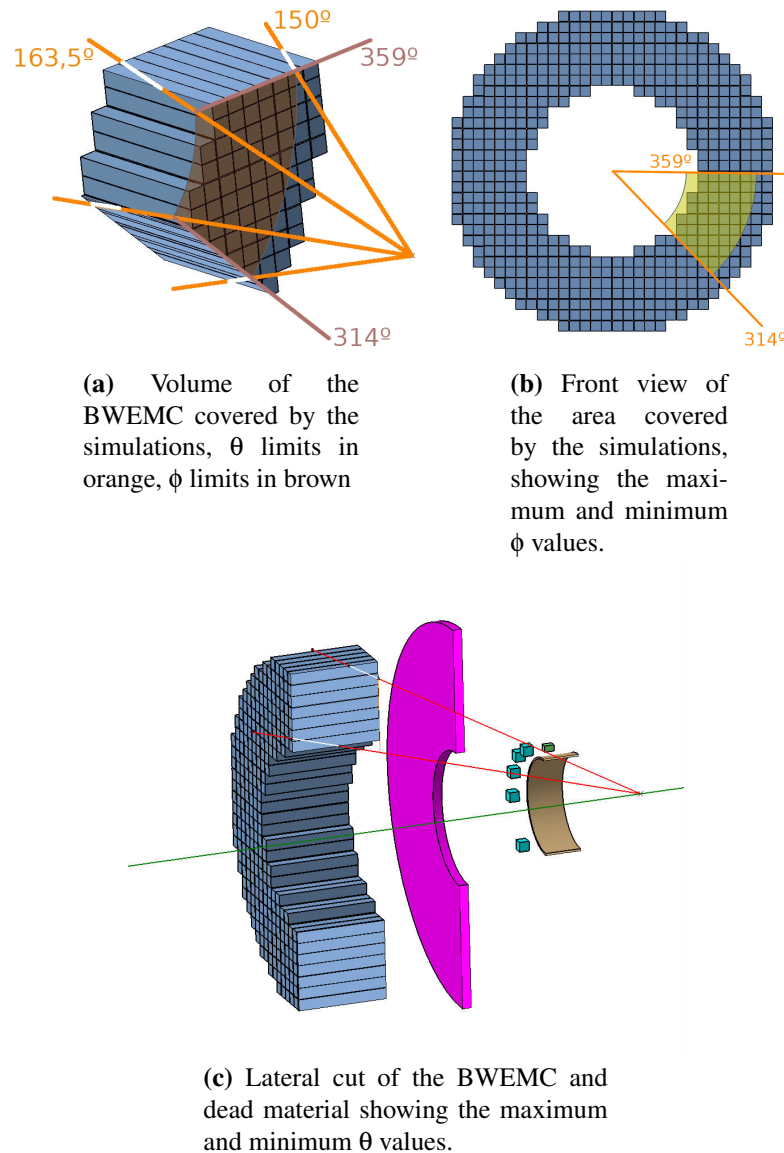
Figure 5.6: Area of the BWEMC covered in the simulations from three different points of view.

Due to the symmetry of the geometry, this was enough to investigate the efficiency and energy resolution in the whole BWEMC. Figure 5.6 shows the area of the BWEMC covered by the simulations from three different viewpoints.

Table 5.3 summarizes all the different setups in which the simulations performed for this Chapter have been done, connecting them with the different geometry scenarios.

Simulation	Geometry	Setup	Number of setups
Influence of STT dead material	STT-0	Combinations of $\theta = 145°, 150°, 155°, 160°, 165°,$ $\phi = 1°, 22.5°, 45°$ and $E = 30\,\mathrm{MeV}, 100\,\mathrm{MeV}, 250\,\mathrm{MeV}, 500\,\mathrm{MeV}, 700\,\mathrm{MeV}$	75
	STT-Low		
	STT-High		
Influence of MVD dead material	MVD	$\phi = 78°$ and $\theta = 147.5°$ at $E = 30, 250,$ and $700\,\mathrm{MeV}$	3
	MVD	$\phi = 34.5°$ and $\theta = 152.5°$ at $E = 30, 250,$ and $700\,\mathrm{MeV}$	
	MVD	$\phi = 45°$ and $\theta = 152.5°$ at $E = 30, 250,$ and $700\,\mathrm{MeV}$	
Influence of MVD dead material whole End Cap	MVD	Combinations of $\theta = 150°, 151.5°, 153°, 154.5°, 156°, 157.5°, 159°, 160.5°, 162°, 163.5°,$ $\phi = 314°, 319°, 324°, 329°, 334°, 339°, 344°, 349°, 354°, 359°$ and $E = 30\,\mathrm{MeV}, 100\,\mathrm{MeV}, 250\,\mathrm{MeV}, 500\,\mathrm{MeV}, 700\,\mathrm{MeV}$	500

Table 5.3: Simulations for the study of the influence of dead material introduced by the MVD and STT electronics and support systems in the energy resolution and efficiency of the BWEMC

5.2 Reconstruction and analysis

5.2.1 Event reconstruction and event selection

For the analysis of the effects on the energy resolution and the efficiency only the bump with the highest energy per simulated event was chosen to reconstruct the energy deposition of the photons in the calorimeter. A typical histogram showing the reconstructed energy can be seen in Figure 5.7 for 250 MeV photons emitted at $\theta = 158°$ and $\phi = 339°$. The energy resolution can be estimated from the width of the peak, and the efficiency is defined from the number of events reconstructed in the histogram (see Section 5.2.2 for more details on the calculation of the energy resolution and the efficiency). The same analysis has been applied for the energy reconstruction of the photons generated under all combinations of θ and ϕ angles and energies with the different geometries. The results of the analyses are shown in the following sections.
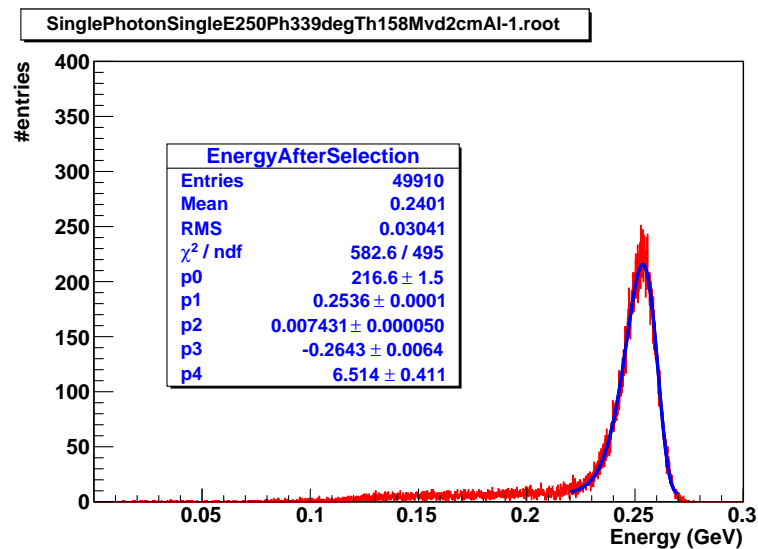
Figure 5.7: Typical energy reconstruction histogram for photons emitted at $\theta = 155°$ and with 250 MeV energy.

(a) $\phi = 45°$, $\theta = 145°$

(b) $\phi = 45°$, $\theta = 150°$

(c) $\phi = 45°$, $\theta = 155°$

(d) $\phi = 45°$, $\theta = 160°$

(e) $\phi = 45°$, $\theta = 165°$
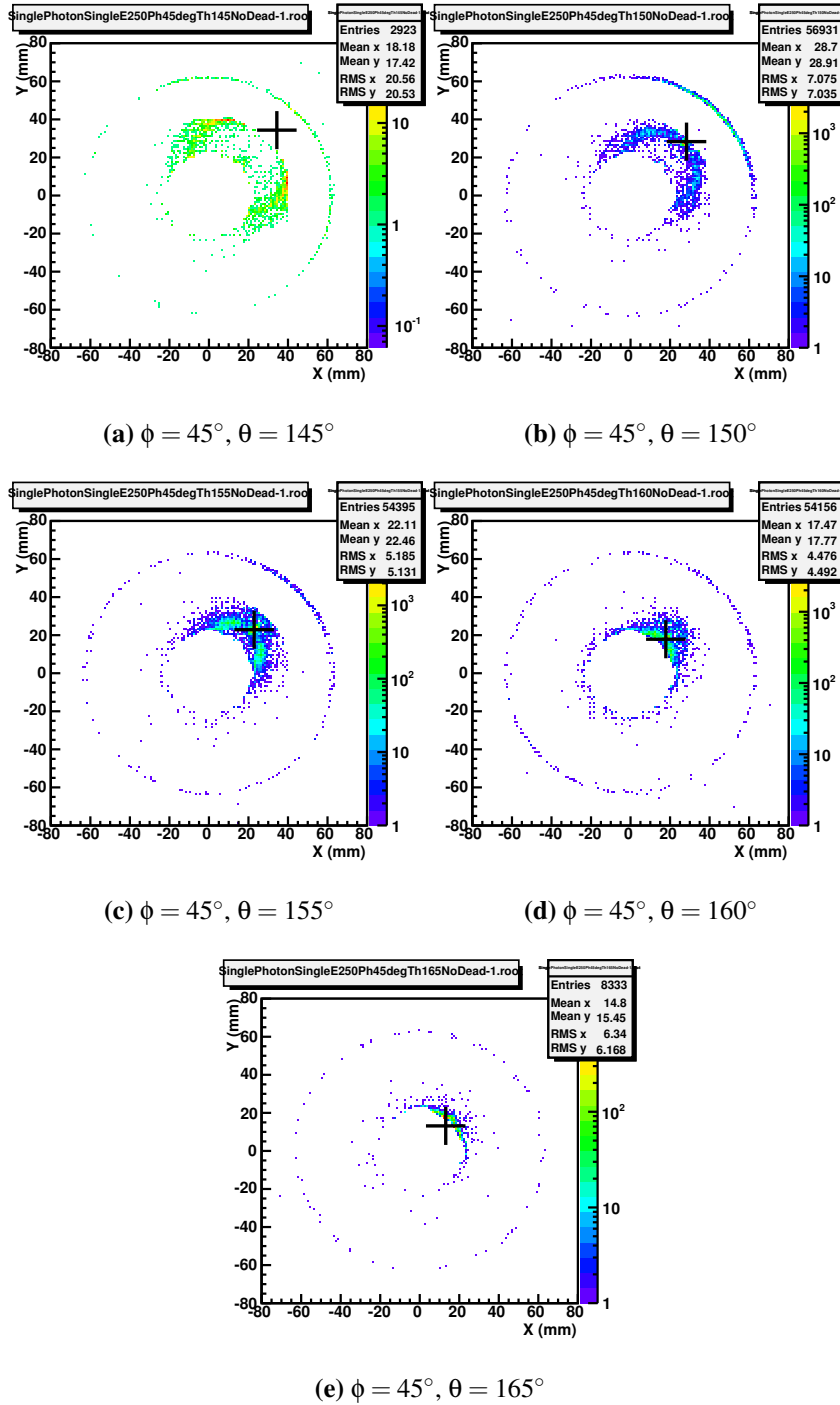
Figure 5.8: Reconstructed bumps in the electromagnetic calorimeter for a simulation with 250 MeV photons without additional dead material. The cross represents the projected impact position (x, y) where a generated γ at the corresponding angles (θ, ϕ) should hit the calorimeter. The ring around the cross corresponds to conversion pairs (e^+e^-) which travel in opposite directions inside the magnetic field (see Figure 5.9 for a better understanding). The outer ring in the pictures corresponds to reconstructed bumps in the barrel produced by secondary particles.
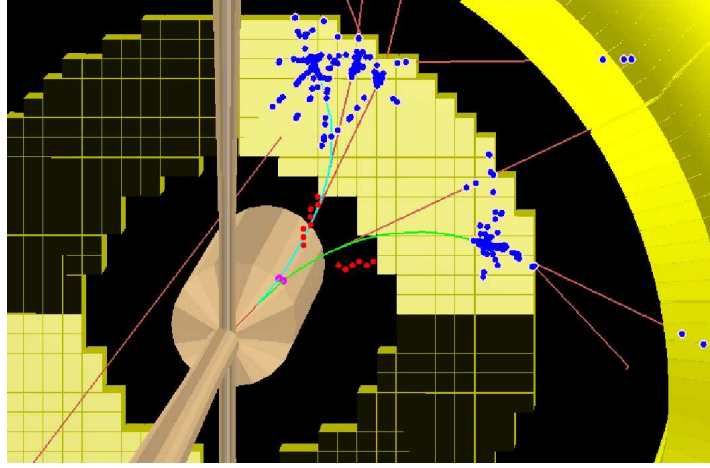
Figure 5.9: Pair production event. A conversion pair e^+e^- (blue and green lines in the picture) travels in opposite directions inside the magnetic field and hits the calorimeter at two different points disposed symmetrically away from the point the original photon should hit the detector. Different conversion pairs would hit the calorimeter in different positions. The accumulation of events explains the ring disposition of the bumps in Figure 5.8.

A cross check between the angle the photons are generated and the point they are reconstructed in the calorimeter was done by drawing the X-Y projection of the positions of the reconstructed bumps. In Figure 5.8 one can see an example for the simulations performed with 250 MeV photons without additional dead material (geometry STT-0). The cross in the pictures represents where a photon shot at the corresponding θ and ϕ angles should hit the BWEMC. The cross is in agreement with the centroid of the reconstructed bumps in the calorimeter. The ring structure around the cross corresponds to conversion pairs (e^+e^-) which travel in opposite directions inside the magnetic field (see Figure 5.9 and caption for a better understanding). The outer ring in the pictures corresponds to hits in the Barrel calorimeter, produced by secondary particles.

5.2.2   Analysis

Each reconstructed energy histogram was fit using the Novosibirsk function [100]

$$f(E) = A \exp\left\{ -\frac{1}{2} \left[\frac{\ln^2\left[1 + \Lambda\tau(E - E_0)\right]}{\tau^2} + \tau^2 \right] \right\}, \qquad (5.1)$$

with

$$\Lambda = \frac{\sinh\left(\tau\sqrt{\ln(4)}\right)}{\sigma\tau\sqrt{\ln(4)}}. \tag{5.2}$$

Here A is a normalization factor, E_0 is the position of the maximum, σ is the standard deviation and τ is a tail parameter.

The energy resolution has been defined as the full width at half maximum (FWHM) divided by the maximum position,

$$E_{res} = \frac{2.35\sigma}{\mu}. \tag{5.3}$$

For the analysis, both σ and μ have been extracted from the fit results.

For the calculation of the efficiency, each fit function has been integrated between $\mu - 3\sigma$ and $\mu + 2\sigma$. This gives us an idea of the number of correctly reconstructed events. The efficiency has been defined as the ratio of this integral and the number of simulated events (50 000).

$$\text{Eff} = \frac{1}{50\,000} \int_{\mu-3\sigma}^{\mu+2\sigma} f(E)dE. \tag{5.4}$$

5.3   Results

5.3.1   Influence of the STT dead material

Figure 5.10 shows three reconstructed histograms for the analysis of the dead material of the STT from simulations with 250 MeV photons emitted at $\phi = 45°$. Comparing them with the drawings shown in Figure 5.11 one can realize that the histogram shown in Figure 5.10a does not reproduce the deposited energy of the photons very well because they are not hitting the calorimeter (145° line in Figure 5.11). Only some secondary particles deposit their energy in the crystals. The histogram in Figure 5.10b shows a very good energy resolution. This is because the photons in this case deposit their full energy in the center of the calorimeter (155° line in Figure 5.11). Finally, the histogram in Figure 5.10c shows the case in which photons only deposit part of their energy in the calorimeter (150° line in Figure 5.11). Similar histograms are obtained for the simulations with photons at $\phi = 1°$ and $\phi = 22.5°$.

Based on this geometry, the simulations at $\theta = 145°$ and $\theta = 165°$ have not been taken into account for the analysis of the energy resolution and the effi-
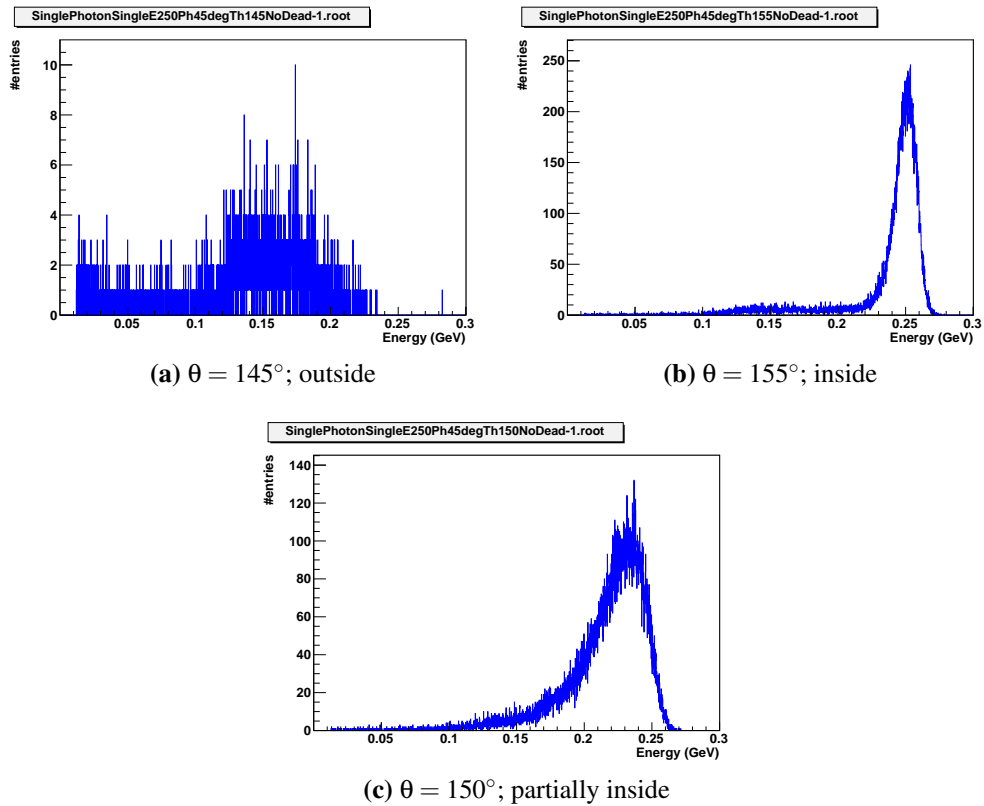
(a) θ = 145°; outside

(b) θ = 155°; inside

(c) θ = 150°; partially inside

Figure 5.10: Typical energy reconstruction histograms for photons with paths inside, outside or partially inside the BWEMC.
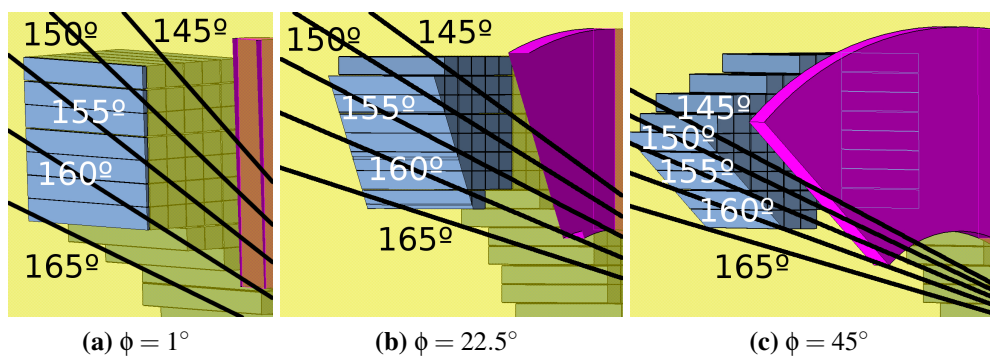

(a) φ = 1°

(b) φ = 22.5°

(c) φ = 45°

Figure 5.11: Schematic view of the trajectories followed by the generated photons in relation to the backward electromagnetic calorimeter for (a) φ = 1°, (b) φ = 22.5° and (c) φ = 45°.

81

E (MeV)	φ \ θ	Eff 150	Eff 155	Eff 160	E$_{res}$ 150	E$_{res}$ 155	E$_{res}$ 160
	1	87.7	84.5	82.2	29.21±0.17	24.29±0.13	25.15±0.15
30	22.5	89.6	84.3	82.5	27.57±0.15	23.32±0.12	23.38±0.13
	45	90.8	84.6	82.3	28.72±0.16	26.21±0.14	23.51±0.13
	1	84.5	84.6	82.3	23.51±0.15	12.28±0.06	12.55±0.06
100	22.5	85.6	84.5	82.3	19.87±0.12	12.20±0.06	12.28±0.06
	45	88.1	84.8	82.0	20.26±0.11	12.60±0.06	12.57±0.06
	1	85.4	84.0	81.9	25.24±0.18	6.97±0.03	7.27±0.03
250	22.5	85.0	84.1	81.9	19.86±0.14	7.07±0.03	7.09±0.03
	45	87.7	84.1	82.0	18.31±0.12	7.20±0.03	7.39±0.03
	1	79.6	83.1	82.1	26.28±0.23	4.74±0.02	5.02±0.02
500	22.5	83.0	83.3	81.8	20.68±0.17	4.62±0.02	4.78±0.02
	45	85.2	83.6	82.2	17.18±0.12	4.83±0.02	4.95±0.02
	1	77.6	82.5	82.7	27.31±0.27	3.88±0.02	4.21±0.02
700	22.5	81.2	83.0	82.1	21.54±0.20	3.84±0.02	3.97±0.02
	45	83.4	83.2	82.8	16.66±0.12	4.01±0.02	4.18±0.02

Table 5.4: Efficiency and energy resolution of the BWEMC from the study without additional dead material for the STT (STT-0). The error of the efficiency has been treated only statistically and it is of the order of 0.3% to 0.5%.

E (MeV)	φ \ θ	Eff 150	Eff 155	Eff 160	E$_{res}$ 150	E$_{res}$ 155	E$_{res}$ 160
	1	83.0	77.2	77.4	31.96±0.21	25.37±0.15	25.25±0.16
30	22.5	83.8	77.7	77.6	29.91±0.18	24.33±0.16	23.56±0.13
	45	85.8	77.7	77.4	31.54±0.20	27.67±0.17	23.56±0.13
	1	64.6	74.8	77.8	23.88±0.30	12.71±0.07	12.68±0.07
100	22.5	71.2	74.7	77.5	20.19±0.19	12.63±0.07	12.41±0.06
	45	72.8	74.9	77.7	20.82±0.18	13.02±0.07	12.82±0.07
	1	73.1	72.3	77.0	27.19±0.29	6.91±0.04	7.30±0.04
250	22.5	79.6	72.3	76.8	22.18±0.18	7.04±0.04	7.03±0.04
	45	81.9	73.0	77.1	19.94±0.14	7.23±0.04	7.30±0.04
	1	63.5	72.8	78.9	28.80±0.55	4.85±0.02	5.17±0.03
500	22.5	74.5	73.2	78.1	22.86±0.25	4.79±0.02	4.89±0.02
	45	80.2	74.1	79.0	18.38±0.15	4.97±0.02	5.07±0.02
	1	68.6	73.8	79.9	28.78±0.41	4.07±0.02	4.37±0.02
700	22.5	77.1	73.8	79.4	22.79±0.23	4.02±0.02	4.17±0.02
	45	80.2	75.1	80.6	17.88±0.15	4.22±0.02	4.37±0.02

Table 5.5: Efficiency and energy resolution of the BWEMC from the study with 2 cm of aluminum as additional dead material for the STT (STT-Low). The error of the efficiency has been treated only statistically and it is of the order of 0.3% to 0.5%.

E (MeV)	θ / φ	Eff 150	Eff 155	Eff 160	E_{res} 150	E_{res} 155	E_{res} 160
30	1	73.2	69.1	68.5	38.87±0.23	25.77±0.18	25.26±0.17
	22.5	73.3	68.8	69.0	30.51±0.21	25.41±0.17	23.50±0.15
	45	75.2	69.2	68.7	32.32±0.21	28.24±0.20	23.79±0.14
100	1	55.8	65.3	67.5	24.91±0.39	13.00±0.08	12.82±0.08
	22.5	61.2	64.8	67.6	20.92±0.22	12.66±0.08	12.48±0.07
	45	62.7	65.2	68.3	20.73±0.21	13.23±0.08	13.09±0.08
250	1	66.7	61.9	66.7	30.49±0.42	7.04±0.05	7.36±0.05
	22.5	72.1	61.5	66.9	25.06±0.25	6.92±0.05	7.12±0.04
	45	74.8	62.3	67.2	21.92±0.19	7.20±0.05	7.43±0.05
500	1	61.3	63.4	70.3	30.52±0.69	5.00±0.03	5.46±0.03
	22.5	70.7	63.6	69.5	24.38±0.30	5.00±0.04	5.25±0.03
	45	75.6	64.7	71.7	19.95±0.19	5.18±0.03	5.62±0.04
700	1	67.5	65.7	73.0	30.58±0.51	4.39±0.03	4.85±0.03
	22.5	75.3	66.4	71.9	23.22±0.24	4.47±0.03	4.63±0.03
	45	77.9	67.1	73.7	19.09±0.18	4.64±0.03	4.98±0.03

Table 5.6: Efficiency and energy resolution of the BWEMC from the study with 4 cm of aluminum as additional dead material for the STT (STT-High). The error of the efficiency has been treated only statistically and it is of the order of 0.3% to 0.5%.

ciency of the calorimeter because the photons do not hit the calorimeter directly or they deposit only a small fraction of their total energy.

Tables 5.4, 5.5, and 5.6 show the results of the analysis of the STT dead material influence. One can observe that the energy resolution is basically unaffected. At 250 MeV, the energy resolution is about 7% for all simulations. However, the influence of the dead material is evident on the reconstruction efficiency. The efficiency passes from about 85% without dead material to a 65% in the case with 4 cm of aluminum (STT-High). This is because the photons either interact with the dead material or not before reaching the BWEMC, but they do not change their energy in flight. The photons that reach the calorimeter deposit their energy normally. This is translated in a reduction of the detection efficiency but the energy resolution remains the same. The efficiency values obtained for the case with the highest dead material are still considered good for the reconstruction of particles at backward angles.

In Figure 5.12 one can see the fit histograms of reconstructed photons at 250 MeV, θ = 155° and φ = 22.5° generated using the three STT geometries (STT-0, SST-Low and SST-High). One can easily see the influence of the dead material on the efficiency by looking to the peak height. Fewer photons go into the peak whereas more go into the tail with the increase of dead material. On the other hand one can also easily see that the peak width, which gives the energy

(a) No additional dead material

(b) 2 cm of aluminum

(c) 4 cm of aluminum

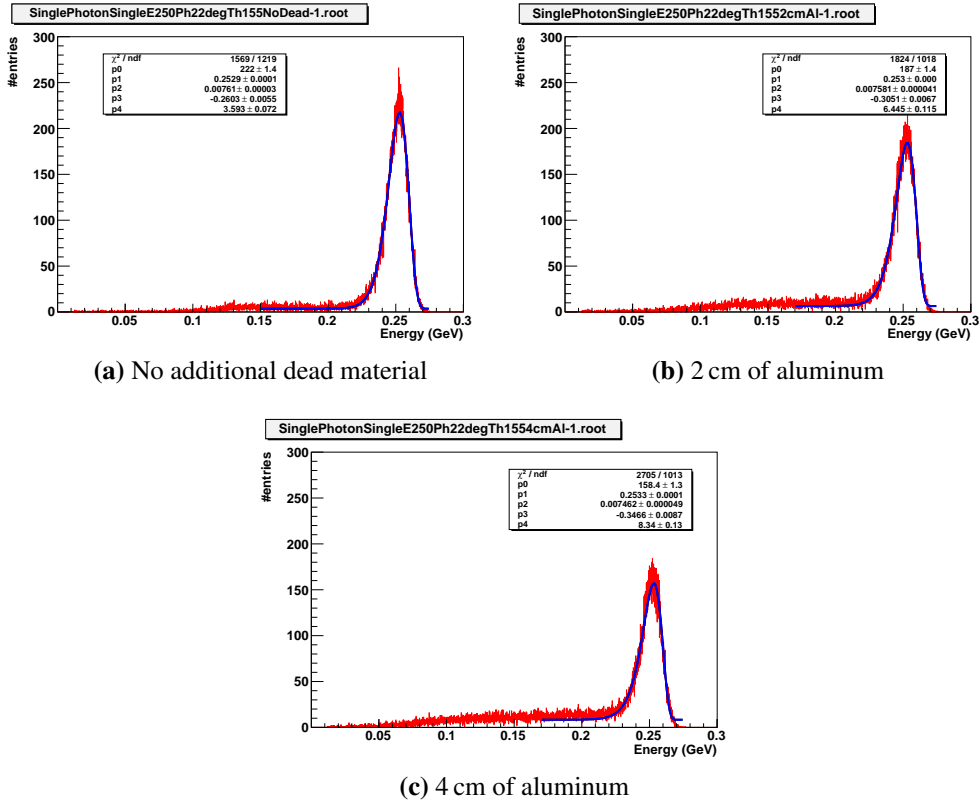**Figure 5.12:** Typical histograms showing the energy reconstruction of photons emitted at $\theta = 155°$ and $\phi = 22.5°$ with 250 MeV and the influence of the dead material introduced by the STT. The width of the peak and the amount of photons reconstructed outside the maximum increases with the amount of dead material. This is translated into an increase of the energy resolution and a lowering of the efficiency.

resolution, is not really affected. It remains approximately the same in all three histograms.

5.3.2 Influence of MVD dead material

The same kind of study as for STT dead material was done for the MVD. The reconstructed photon histograms were fit with the Novosibirsk formula, Equation (5.1), and the energy resolution and the efficiency were calculated in each case from the results of the fit using Equations (5.3) and (5.4) respectively.

E (MeV) ϕ	30	250	700
34.5	29.54	16.11	13.29
45	66.38	53.82	53.13

Table 5.7: Efficiency results for the study of the dead material introduced by the MVD

E (MeV) ϕ	30	250	700
34.5	26.89± 0.29	7.31±0.11	4.19±0.08
45	28.57±0.20	8.24 ±0.07	5.01 ±0.04

Table 5.8: Energy resolution results for the study of the dead material introduced by the MVD

Table 5.7 shows the efficiency for each case simulated. For the simulations done at $\phi = 78°$ the efficiency was impossible to measure because the photons are emitted in a direction almost outside the BWEMC (see left side of Figure 5.5a). The same problem appears for the energy resolution measurement at the same angle (Table 5.8).

For the simulations done at the other ϕ angles one can appreciate that the efficiency is very much influenced by a big block of dead material intersecting the photon trajectory, but the efficiency is still above the 50% when the trajectory intersects only the cylinder of dead material of the MVD.

For the energy resolution, show in Table 5.8, the same conclusion as for the study with the STT dead material apply. The energy resolution is again not affected much by the dead material in the cases in which the efficiency was good. For the cases in which the efficiency was not good, the energy resolution is in general worsen but in it can still be calculated in almost all cases giving reasonable values (around 8% at $E = 250\,\text{MeV}$ and $\phi = 45°$).

Eresolution 250MeV

(a)
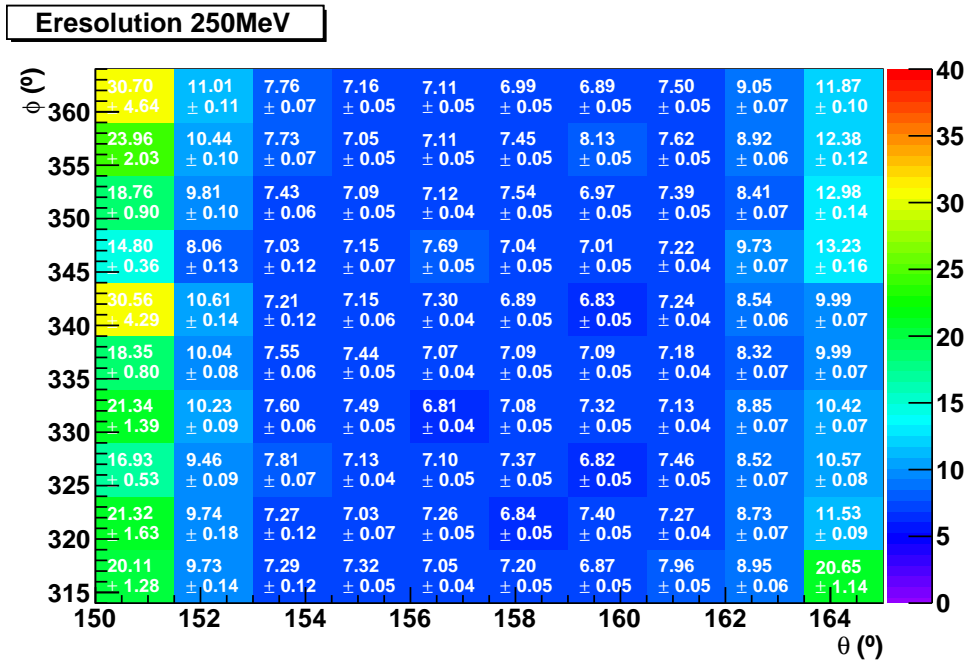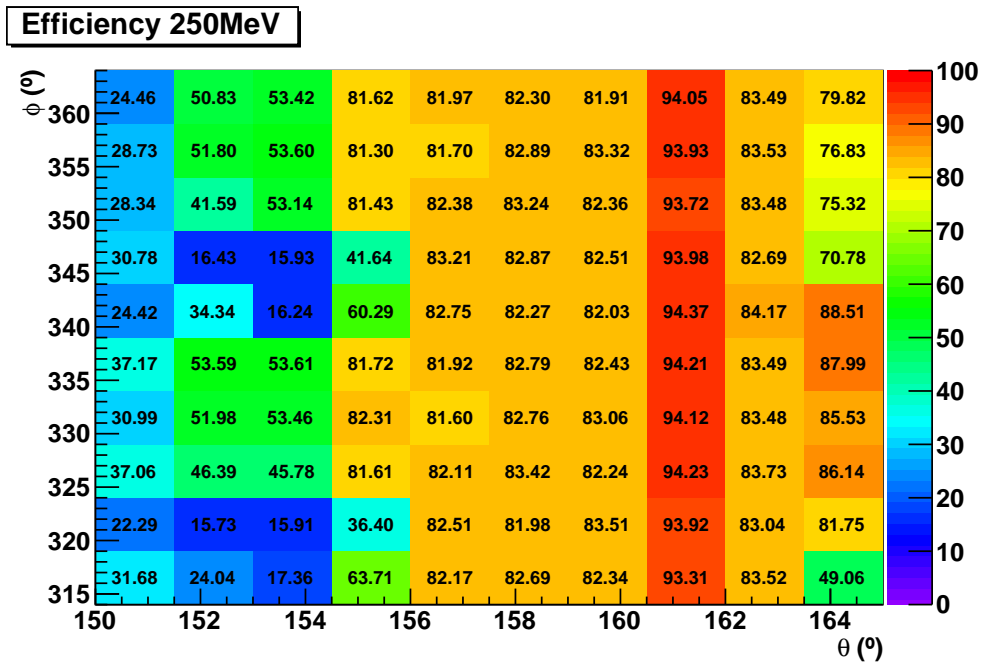
Efficiency 250MeV

(b)

Figure 5.13: Energy resolution and efficiency map for 250 MeV (values given in %). It includes the dead material introduced by the STT and the MVD.

5.3.3 Energy resolution and efficiency in the whole BWEMC

To have a complete understanding of the influence of the dead material introduced by the STT and MVD detectors, simulations with photons emitted under θ and ϕ angles covering half a quarter of the BWEMC were done. The results of the efficiency and the energy resolution from these simulations are shown in Figure 5.13 for a photon energy of 250 MeV. One can see that the energy resolution is about 7% in this case for the whole central part of the calorimeter (between $\theta = 153°$ and $\theta = 160.5°$ in Figure 5.13a). In the most inner and outer parts of the calorimeter (right and left bands in the plots) one can see the border effects of the energy loss, *i.e.* the energy of the photons hitting there is not fully deposit inside the calorimeter and the loss effects are translated into an efficiency reduction.

One can recognize different areas in the efficiency map (Figure 5.13b). Below $\theta = 154.5°$, the efficiency is lower because some photons have to go through the MVD cylinder. For $\phi \in [339°, 349°]$ and $\phi \in [339°, 349°]$ there is a big reduction in the efficiency due to the blocks representing the dead material of the MVD. Despite the efficiency being quite low in these regions, they cover only a very small area (of the order of less than 10%) in front of the BWEMC and do not represent a problem for the energy resolution, which stays nearly the same (compare with the same areas in Figure 5.13a). The inner part of the map in Figure 5.13b (orange region) shows an efficiency of about 82%. In this area the photons go through the 2 cm aluminum plate that simulates the STT dead material. Some of these photons are converted into e^+e^--pairs and do not reach the calorimeter but the efficiency in this region is still very good. Next to this area, one can recognize a red band ($\sim 93\%$ efficiency) for photons at $\theta = 160.5°$. At this angle, there is a gap through which the photons can reach the BWEMC without interacting with any additional dead material, being able to be detected with very high efficiency. Above $\theta = 162°$ some photons are again lost due to border effects. Their energy is not fully deposited and they are reconstructed outside the peak in the histogram (see for example Figure 5.10c).

5.4 Conclusion

Simulations of single photons with different energies and θ and ϕ angles have been done under different dead material conditions using the $\overline{P}$ANDA detector setup. The energy resolution and the efficiency of the BWEMC were calculated in each case and the influence of the dead material was studied.

A map of energy resolution and efficiency was performed for half a quarter of the BWEMC. Due to geometry symmetries this is enough to study the characteristics of the whole BWEMC.

The results showed that the efficiency of the BWEMC is very much low-ered (below 20%) in some very small and localized points. These areas represent less than a 10% of the whole solid angle covered by the BWEMC. Therefore, this low efficiency spots should not be a problem for the detection of particles in the backward direction. The efficiency stays above the 50% for a quarter of the calorimeter and above the 80% for the rest.

On the other side, the energy resolution of the BWEMC is very good (of the order of 7% at 250 MeV) and it is not very much affected by the lowering in the efficiency. Only the border effects can be noticed at lower and higher θ angles.

Both characteristics of the BWEMC show that the performance of this subdetector will be good enough to carry out the $\overline{\mathsf{P}}$ANDA physics program and the detection of particles under backward angles will be feasible.

6

Feasibility study for a measurement of the electromagnetic form factors in the time-like region

---

This Chapter concentrates on the measurement feasibility of the electromagnetic form factors (EMFF) of the proton in time-like region with $\overline{\mathsf{P}}$ANDA.

The EMFF of the proton can be accessed via the annihilation process $\bar{p}p \to e^+e^-$. Simulations to study the reconstruction of this channel as well as to study the rejection of the background, mainly $\bar{p}p \to \pi^+\pi^-$, have been done in the framework of this Thesis. Part of the results exposed here have been also published in Reference [5].

6.1 Simulation and analysis procedure

Simulations of signal and background samples at different beam energies have been done following the conditions described in Sections 2.3.3 and 2.3.4 of Chapter 2.

For the analysis of the signal, simulations with high statistics have been used for the analysis of the detector acceptance and the study of the efficiency corrections. Samples with the calculated amount of events expected for an integrated luminosity of $\mathcal{L} = 2\,\mathrm{fb}^{-1}$ have been used for the study of the feasibility of measuring the cross section at different values of q^2.

	Cut	Reason for the cut
PID CUTS	Very Loose Loose Tight Very Tight	Selection of electrons
CL CUTS	$CL_{e^+e^-/\pi^+\pi^-} > 10^{-3}$ $CL_{e^+e^-} > 10 \cdot CL_{\pi^+\pi^-}$	Rejection of extremely bad fits Rejection of pions

Table 6.1: PID and kinematic fit cuts applied to discriminate $\bar{p}p \to \pi^+\pi^-$ from $\bar{p}p \to e^+e^-$.

All possible combinations of one positive track and one negative track have been taken into account as candidates for the reaction $\bar{p}p \to e^+e^-$ in all background and signal channels. Once these preselection is done, the different cuts on the electron particle identification (PID) probability are applied to separate π from e. The number of candidates surviving to the cuts in the background samples has to be very small in comparison with the signal samples. In addition, also a kinematic fit using different hypotheses ($\bar{p}p \to e^+e^-$ or $\bar{p}p \to \pi^+\pi^-$) has been performed also over all signal and background samples. Additional cuts on the confidence level of the fits have been applied to reach the desired background suppression. Table 6.1 shows a list of all the cuts used in the analysis.

A more detailed description of all the process is presented in the following.

6.2   Suppression of $\pi^+\pi^-$ and $\pi^0\pi^0$ backgrounds

Due to the difference of six orders of magnitude in the cross section between the signal and the $\pi^+\pi^-$ background, three event samples of at least 10^8 $\pi^+\pi^-$ events each were simulated at $q^2 = 8.21$, 13.8, and 16.7 (GeV/c)^2.

The strategy of the analysis is based in applying different PID and kinematic cuts to the background and signal samples in order to suppress the maximum amount of background whilst keeping the maximum amount of signal possible. To discriminate pions from electrons, different cuts have been applied to the PID combined likelihood for the assumption that the detected particle is an electron. The numbers of simulated $\pi^+\pi^-$ events left after Loose, Tight and Very Tight PID cuts (corresponding respectively to the minimum values of the identification probability 85%, 99% and 99.8% for each lepton of the pair) are displayed in Table 6.2. The Very Tight cuts are needed to reach a rejec-

tion factor of at least few times 10^7 (pink line in Figure 6.1 as an example for $q^2 = 8.2\,(\text{GeV/c})^2$) for all background samples.

Further selection based on the reaction vertex and on the kinematic fit method, explained in Chapter 4, is applied. The kinematic fit method is a constrained fit that takes into account energy and momentum conservation. From this, a confidence level (CL) associated with $\pi^+\pi^-$ hypothesis, CL_π, and with the e^+e^- hypothesis, CL_e, are calculated. The selection of the electrons results from two conditions: $CL_{\pi,e} > 10^{-3}$ (which corresponds to $\chi^2 < 7$ for the kinematic fit) and $CL_e > 10\,CL_\pi$. These conditions result in an additional rejection factor of the background of $\simeq 100$. Finally, combining the kinematic fit with the 10^7 suppression factor of the PID cut (Table 6.2) one can assure that the overall background suppression factor is of the order of a few times 10^9 for all samples. For $|\cos(\theta)| < 0.8$, due to the value of the cross section of the background in this angular area and due to the good PID performance of the detector, the $\pi^+\pi^-$ contamination does not depend drastically on the angle and remains below 0.1% in the q^2 range of interest. This can be seen in Figure 6.1, where the number of misidentified background events is approximately constant at every $\cos\theta$ after the cuts.
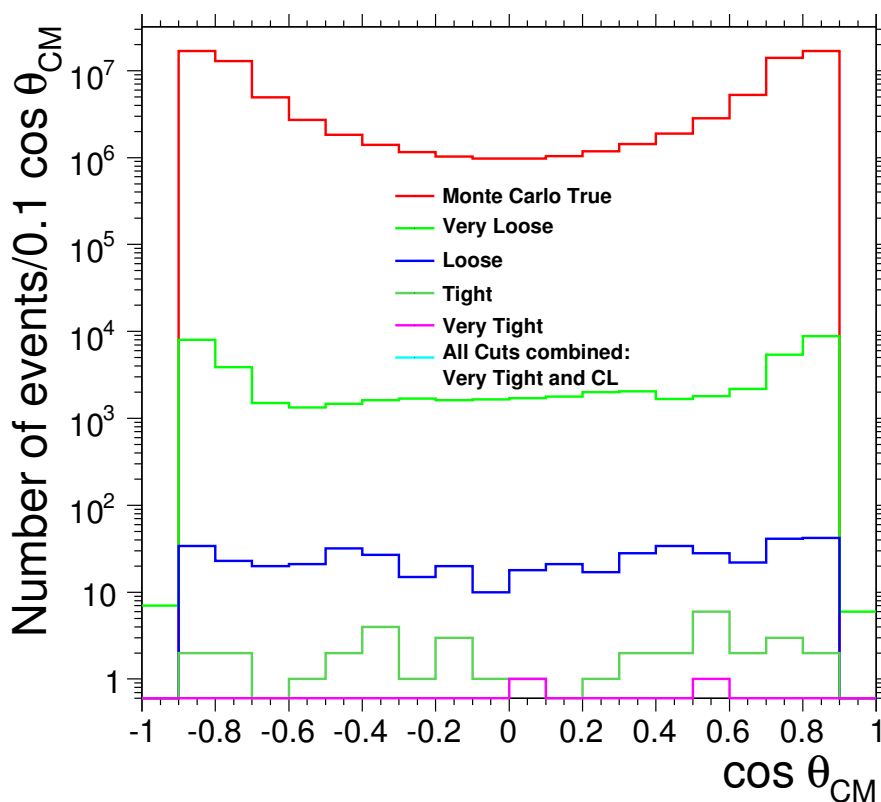
Figure 6.1: Example of background suppression of $\bar{p}p \to \pi^+\pi^-$ at $q^2 = 8.2\,(\text{GeV/c})^2$.

q^2 [GeV/c]^2	8.2	12.9	16.7
Simulated	10^8	10^8	$2 \cdot 10^8$
Loose	425	$1.2 \cdot 10^3$	$3 \cdot 10^3$
Tight	31	70	120
Very Tight	2	5	6
Kinematic fit (CL)	$8 \cdot 10^5$	10^6	$2.5 \cdot 10^6$

Table 6.2: Number of $\pi^+\pi^-$ events, misidentified as e^+e^-, after Loose, Tight and Very Tight PID cuts corresponding to respective minimum values of the electron identification probability 85%, 99% and 99.8% and after the confidence level (CL) cut on the kinematic fit for three different q^2 values (see text).
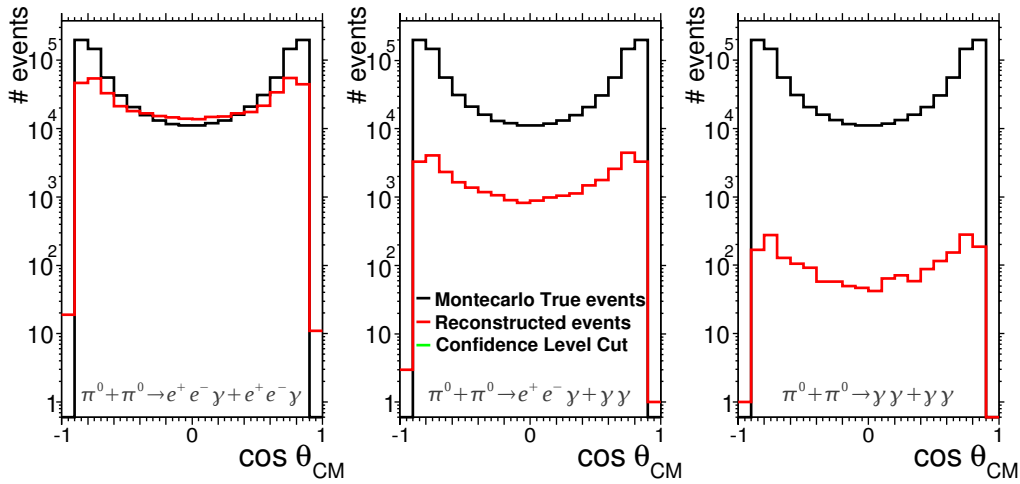
Figure 6.2: Suppression of $\pi^0\pi^0$ background events, including possible Dalitz decays. The left plot corresponds to normal decay of π^0, the middle plot corresponds to one of the π^0 decaying via Dalitz decay and the right plot corresponds to both π^0 decaying via Dalitz decay. The curve after CL cuts is not visible in the plots since there are no background misidentified events after this cut.

For the $\pi^0\pi^0$ channel, Dalitz decay, $\pi^0 \rightarrow e^+e^-\gamma$, has a probability 10^{-2}. Three processes can be sources of e^+e^- pairs: i) double Dalitz decay of the two π^0, ii) Dalitz decay of one of the pions and photon conversion from the other pion, and iii) photon conversion from two different pions. All these processes, with comparable rates, produce a six particle final state. However, even if the produced e^+e^- pairs fulfill the PID cut, the kinematic constraints give a rejection factor, which combined with the probability for such processes, lead to an efficient suppression of this background. Moreover, by requiring that only a single e^+e^- pair has been identified in the whole detector solid angle, it is possible to reduce even further the contribution of this channel. Figure 6.2 shows that

only *CL* cuts are enough to suppress the whole background coming from possible $\pi^0\pi^0$ decays: no misidentified event survives to the cuts.

6.3 Analysis of the e^+e^- channel

The same cuts used for the suppression of the background were used for the analysis of the signal in order to assure that the background contamination fraction remains below the required 0.1%. Simulations for the reaction $\bar{p}p \rightarrow e^+e^-$ were done at the nine q^2 values corresponding to Table 2.1 for $\mathcal{R} = 0$, 1, and 3.

A realistic projection of the angular distribution of e^+e^- events expected at $\overline{\mathsf{P}}$ANDA is given in Figure 6.3, for $q^2 = 8.21$ (GeV/c)^2, assuming $|G_E| = |G_M|$. The reconstructed events (red squares) are obtained with a full Monte Carlo simulation that takes into account tracking, detector efficiency, and acceptance.
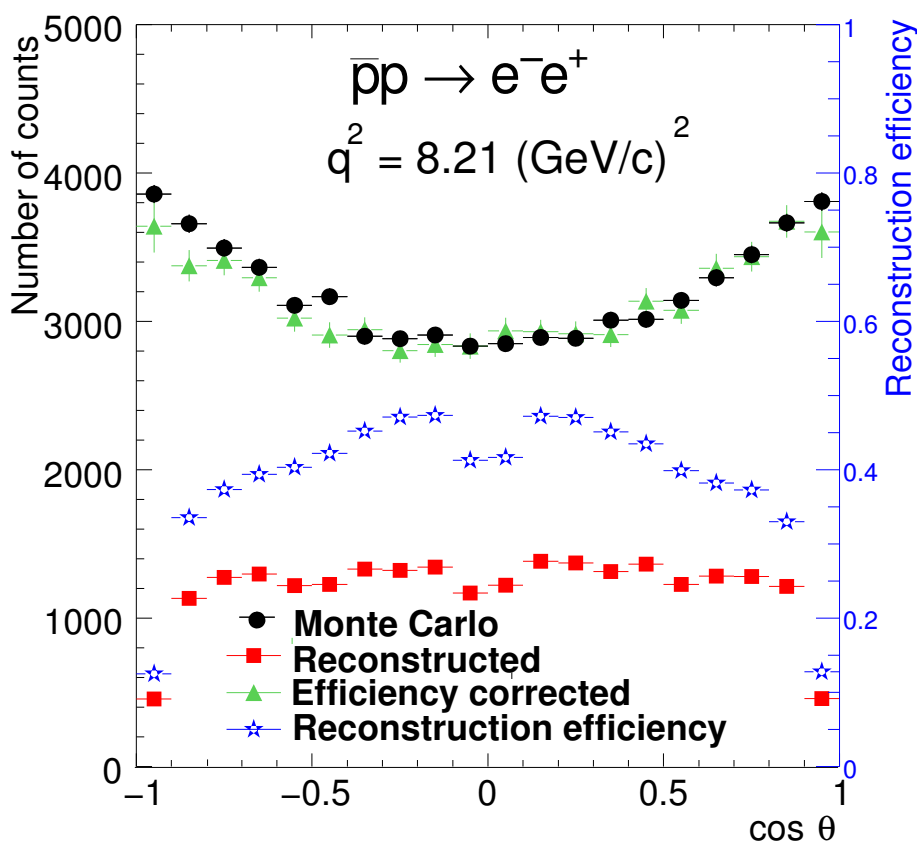
Figure 6.3: Angular distribution of electrons from e^+e^- pairs as a function of $\cos\theta$ at $q^2 = 8.21$ (GeV/c)^2: generated events (black circles), reconstructed events (red squares), acceptance and efficiency correction (blue stars, left scale), and efficiency corrected events (green triangles).
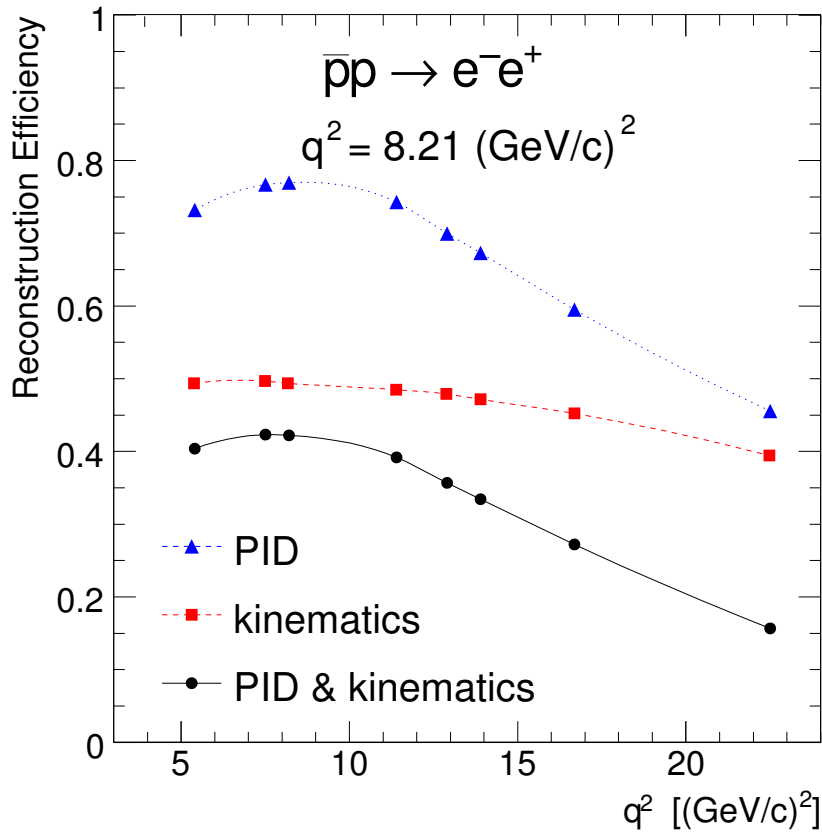
Figure 6.4: Reaction $\bar{p}p \to e^+e^-$: average reconstruction efficiency as a function of q^2 (black solid line). The effect of applying kinematic constraints (red dashed line) and PID cuts (blue dotted line) are separately shown.

The reconstruction efficiency corrections (blue stars, right scale) have been obtained from an independent simulation with high statistics which assumes an isotropic electron distribution. Once corrected for this efficiency, the distribution (green triangles) nicely agrees with the generated data (black circles). One can see that at this q^2 value the average efficiency is on the order of 40%. The reconstruction efficiency depends on the angle. The sudden drop at $|\cos\theta| > 0.8$ corresponds to a decrease of the PID efficiency. At $q^2 = 8.21\,(\mathrm{GeV/c})^2$ the poor dE/dx identification from the STT is responsible of this drop. The loss of efficiency at $\cos\theta = 0$ is due to the two holes drilled in the iron yoke for the injection of the target material. This areas are as a consequence not covered by any detector. Similar plots as in Figure 6.3 are shown in Appendix A for all the other simulated energies, including also a fit to the reconstructed and corrected angular distribution (see next Section).

The reconstruction efficiency, after integration over the angular range $|\cos\theta| \leq 0.8$, is shown in Figure 6.4. It is maximum at $q^2 \sim 8\,(\mathrm{GeV/c})^2$ and decreases to 15% at $q^2 \sim 23\,(\mathrm{GeV/c})^2$. The effects of PID and kinematic con-

straints are shown separately. The drop at large q^2 is mainly due to PID cuts because the laboratory angular distribution is more forward peaked with increasing q^2, whereas the kinematic selection shows a nearly constant behavior.

6.4 Results and discussion

For each q^2 value, the simulated differential cross section was fitted with a two-parameter function, in order to extract a global normalization α and the form factor ratio $\mathcal{R} = |G_E|/|G_M|$, according to

$$N(\cos\theta) = \alpha[\tau(1 + \cos^2\theta) + \mathcal{R}^2 \sin^2\theta]. \tag{6.1}$$

The reason for that is because the luminosity was not taken into account in the first analysis. The results are shown in Figure 6.5, where the expected statistical uncertainty on $\mathcal{R}$ is plotted as a function of q^2 as a yellow band for the case $\mathcal{R} = 1$ and compared with the existing values from References [2] (squares) and [101] (triangles). The results of the fits for all simulated q^2 values and assumptions for the ratio $\mathcal{R}$ can be seen in Appendix A. In addition to the fits for the extraction of $\mathcal{R}$, several methods were used to extract the error bars. Different kinds of fits were performed with MINUIT, extracting $\mathcal{R}$ or $\mathcal{R}^2$ from the quadratic Expression (6.1) and also from the angular asymmetry which enters linearly in a $\cos^2\theta$ distribution (see [5] for more details on the angular asymmetry definition). A Monte Carlo method was also used. Detailed discussion and numerical values for different assumptions of $\mathcal{R}$ can be found in Reference [102]. As an example, for $q^2 = 13.84\,(\text{GeV/c})^2$, one obtains from a Monte Carlo approach $\mathcal{R} = 1^{+0.54}_{-0.51}$, $\mathcal{R} = 3^{+0.90}_{-0.53}$ and an upper limit of 0.61 ($CL = 68\%$) for $\mathcal{R} = 0$. Therefore we concluded that a meaningful value for $\mathcal{R}$ can be extracted up to $q^2 \sim 14\,(\text{GeV/c})^2$. In the low q^2 region, the precision is at least an order of magnitude better than for the existing data. With a precise measurement of the luminosity the extraction of $|G_E|$ and $|G_M|$ in time-like region will also be possible. Their values can be compared with the corresponding space-like values and with existing model calculations.

Model predictions vary widely as shown in Figure 6.5. A QCD inspired parametrization based on scaling laws [55, 56] predicts $\mathcal{R} = 1$ (red dashed line). The green solid line is based on a vector meson dominance (VMD) approach from Reference [103], and grows up to $q^2 \sim 15\,(\text{GeV/c})^2$. The blue dash-dotted line is the prediction of Reference [104], based also on VMD, but including terms to ensure the proper asymptotic behavior of QCD. These models, originally built in the space-like region, have been analytically extended to the time-like region and the parameters have been readjusted in Reference [105] in order to fit the world data in the whole kinematic region (*i.e.*, in space-like region, the electric and magnetic proton and neutron EMFF, and in time-like region,

the magnetic FF of the proton and the few existing data for neutron [106]). Although these models reproduce reasonably well the EMFF data, they give very different predictions for the form factor ratio. Polarization observables show a large sensitivity to these models (Reference [105]).
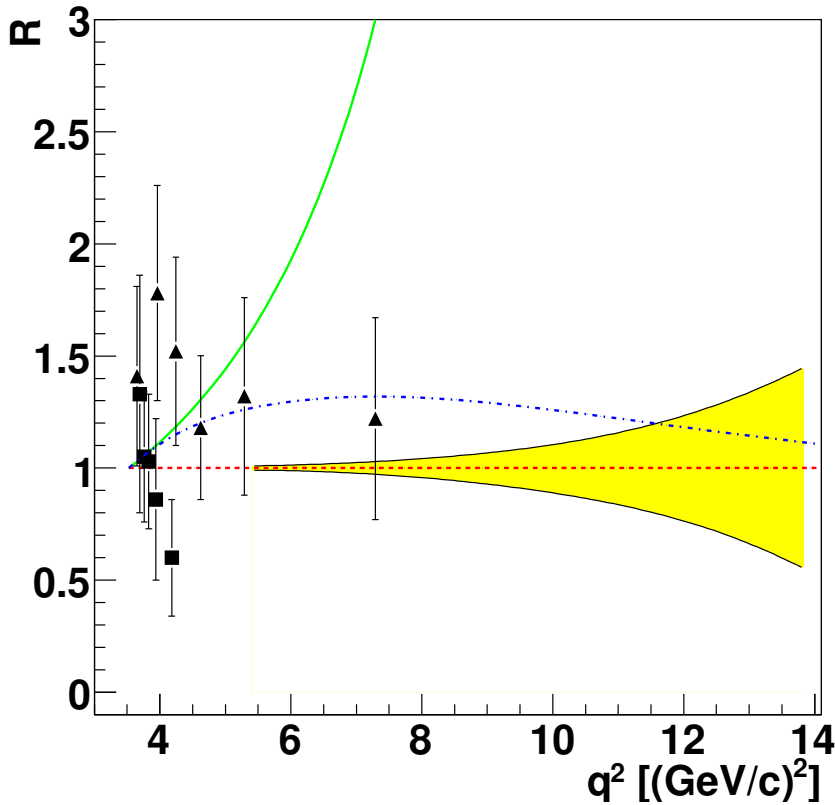

Figure 6.5: Expected statistical precision on the determination of the ratio $\mathcal{R}$, (yellow band) for $\mathcal{R} = 1$, as a function of q^2, compared with the existing data from References [101] (triangles) and [2] (squares). Curves are theoretical predictions (see text).

At larger q^2, when the sensitivity of the experiment is insufficient to extract $\mathcal{R}$ directly from a fit, $|G_M|$ will be determined assuming $\mathcal{R} = 1$, as done in previous measurements. With a precise knowledge of the luminosity, the absolute cross section can be measured up to $q^2 \sim 28\,(\text{GeV/c})^2$. The precision of such a measurement assuming $|G_E| = |G_M|$ is shown in Figure 6.6.

The comparison with the world data shows an expected improvement of at least a factor ten. Here only the statistical accuracy, based on the number of events measured and identified is taken into account. The reported error bars are based on a conservative extrapolation of the values reported in Table 6.2.

Systematic effects of the tracking and reconstruction procedure will be evaluated for the real data, mostly by measurements of known reactions, which are the source of well controlled data samples.
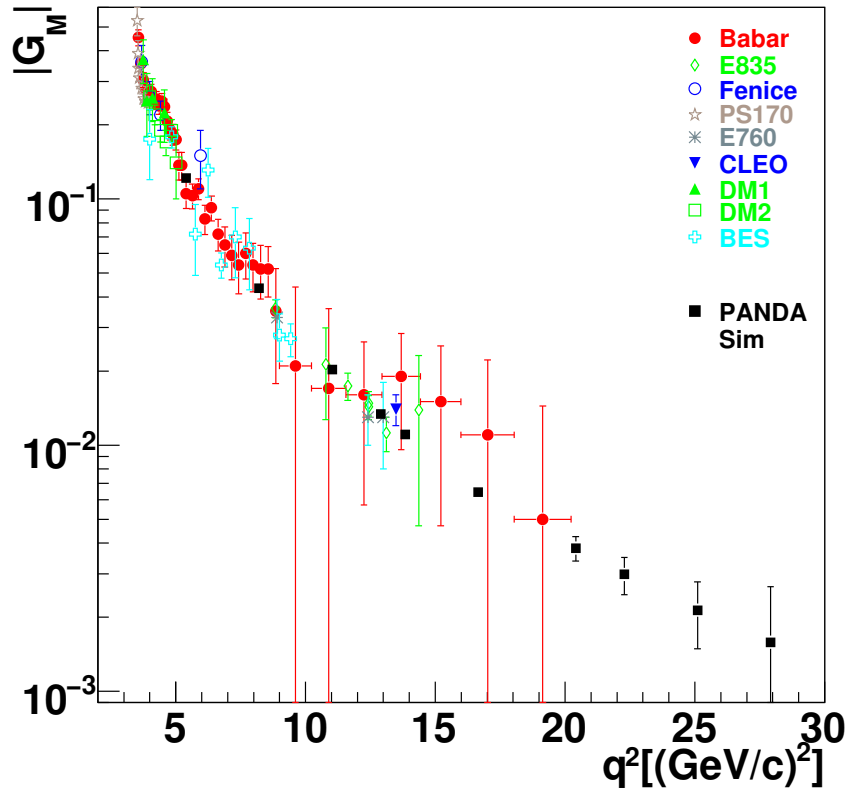
Figure 6.6: q^2 dependence of the world data on the effective proton time-like FF, $|G_M|$, as extracted from the annihilation cross section assuming $|G_E| = |G_M|$: BaBar [101] (red full circles); Fenice [106] (blue open circles); E835 [1, 107] (green open lozenge); PS170 [2] (gray open stars); E760 [54] (blue asterisk); DM1 [108] (green full triangles); DM2 [109] (green open squares); BES [110] (cyan open cross); CLEO [111](blue triangle down); $\overline{\text{P}}$ANDA (full black squares) corresponding to an integrated luminosity of 2 fb^{-1}, errors are statistical only (this work).

Comparing such data samples to simulations, as a function of momentum and angle, will allow one to check the rejection power against pions for each subdetector and to determine the electron identification efficiency. This insures complete understanding of the global rejection probability (*i.e.* the purity of the electron data sample) and knowledge of the overall electron reconstruction efficiency.

6.5 Simulations with muons

The same analysis for the extraction of the protons form factors could be done using the reaction

$$\bar{p}p \rightarrow \mu^+\mu^-. \tag{6.2}$$

The cross section for this process is also given by Equation (2.23). Different simulations for the signal were also done to study the feasibility of measurement of the form factors using this process at the q^2 values and hypotheses for $\mathcal{R}$ shown in Table 6.3.

q^2	$\mathcal{R}$ hypothesis	N events simulated
5.4	0 1 3	10^6
8.2	0 1 3	10^6
12.9	0 1 3	10^6

Table 6.3: $\mathcal{R}$ hypothesis for the simulations and number of events simulated in each case.

Two samples of background, which is assumed to be the same as for the electronic case, were generated at $q^2 = 8.2$ and $12.9\,\mathrm{GeV/c^2}$ and analysed to study the rejection factor in this case. The separation of muons and pions using only PID cuts was found to be more difficult than in the case of electrons. The hypotheses used in the likelihood level for the identification of muons are shown in Table 6.4. The reason why the PID cuts were not helping in the discrimination of μ is because the muon detector was not fully implemented in the simulation software, and only three detector layers were taken into account. This is translated in a very poor efficiency for the identification of muons. In addition to the PID cuts, also the kinematic fit analysis was performed using two hypotheses: $\mu^+\mu^-$ and $\pi^+\pi^-$. The cuts applied to the confidence level of the fits under both hypotheses are also shown in Table6.4 The similarity among the masses of π and μ makes the kinematic fit to fail in the separation of background and signal. Combining the CL cuts with the previously studied PID cuts one can get a good background suppression, but it implies a drastic signal reduction in all cases. An example of these results can be seen in Figure 6.7 for the simulations at $q^2 = 12.9\,\mathrm{GeV/c^2}$, where different PID and *CL* cuts have been applied to signal and background samples.

	Cut	Reason for the cut
	VL	
	L	
PID CUTS	T	Selection of muons
	VT	
	LH>90%	
CL CUTS	$CL_{\mu^+\mu^-} > 10^{-3}$	Rejection of extremely bad fits
	$CL_{\mu^+\mu^-} < 10 \cdot CL_{\pi^+\pi^-}$	Rejection of pions
	$CL_{\mu^+\mu^-} < 50 \cdot CL_{\pi^+\pi^-}$	

Combination of cuts	
Combined 1	LH>90% $+ CL_{\mu^+\mu^-} > 10^{-3} + CL_{\mu^+\mu^-} < 10 \cdot CL_{\pi^+\pi^-}$
Combined 2	LH>90% $+ CL_{\mu^+\mu^-} > 10^{-3} + CL_{\mu^+\mu^-} < 50 \cdot CL_{\pi^+\pi^-}$

Table 6.4: PID and kinematic cuts used for the study of the measurement of the EMFF using muons.

q^2	Cut	Background Suppression	Signal Efficiency (%)
8.2	Combined 1	$3.7 \cdot 10^7$	0.30
	Combined 2	$3.7 \cdot 10^7$	0.07
12.9	Combined 1	$1.1 \cdot 10^8$	0.22
	Combined 2	$1.1 \cdot 10^8$	0.03

Table 6.5: Background suppression and signal efficiency achieved using muons as signal.

Table 6.5 shows the achieved background suppression and the signal efficiency after the studied cuts. A measurement of this channel would not be possible under the simulated conditions if we want to keep a sufficiently clean sample. Although the results obtained in this analysis are not very promising, we expect that the same simulations and a similar analysis could be successfully done using the new PandaROOT software. This software will include better PID capabilities for muons, *i.e.* it includes all the foreseen layers for the muon detector, and the results are expected to be better in the new framework.
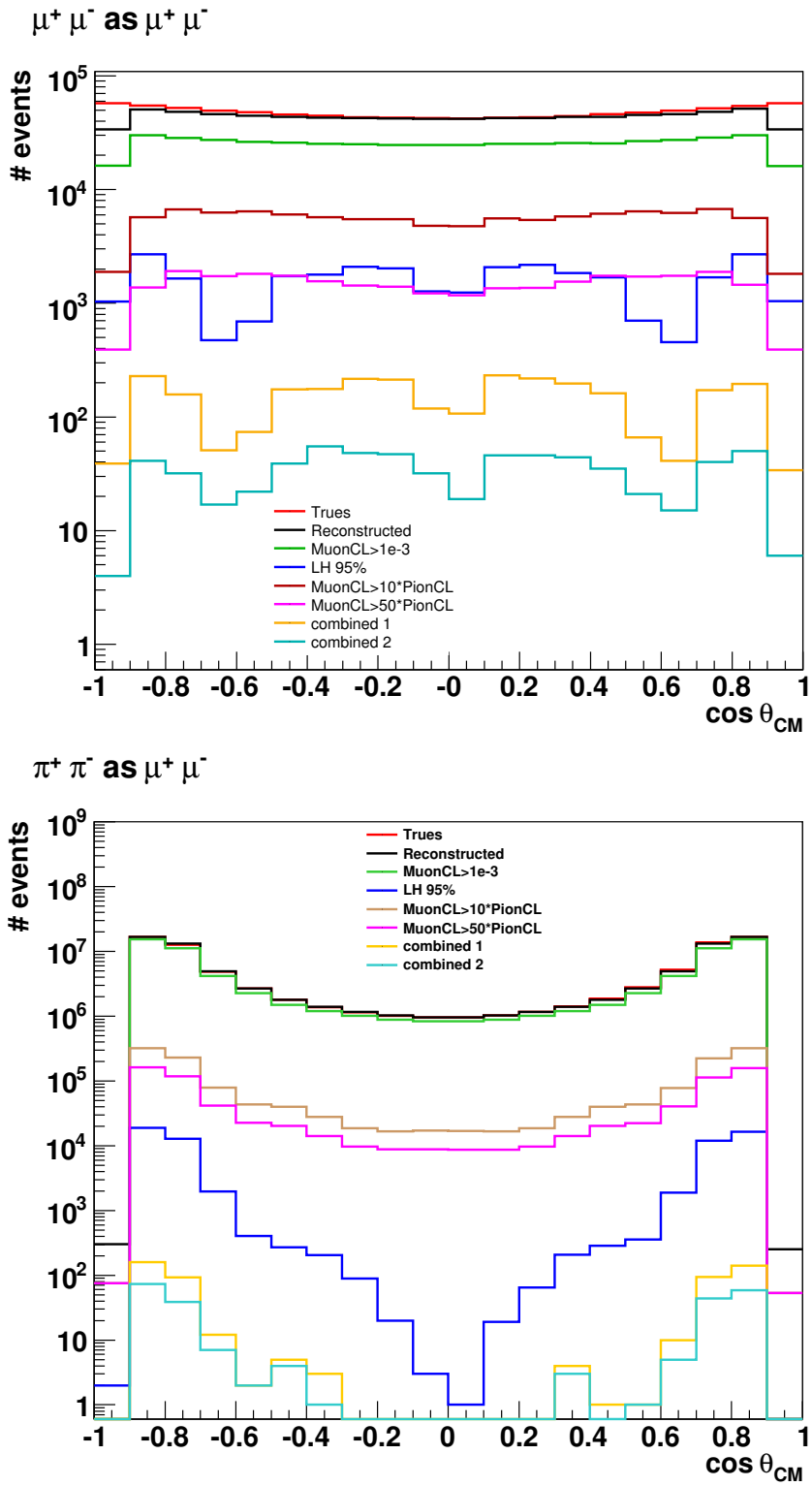
Figure 6.7: Reconstruction of $\bar{p}p \to \mu^+\mu^-$ and $\bar{p}p \to \pi^+\pi^-$ background suppression.

7

Measurement of the transition distribution amplitudes

The measurement of the differential cross section for the channel $\bar{p}p \to e^+e^-\pi^0$ with $\overline{\text{P}}$ANDA will serve as a test of the predictions given by the transition distribution amplitudes (TDA) production mechanism and as a test of the validity of this approach. Dedicated simulations have been performed in the framework of this Thesis to study the feasibility of measurement of this channel with $\overline{\text{P}}$ANDA. This Chapter summarizes the work done and shows the results of the analysis.

7.1 Simulation studies and analysis procedure

Several simulations for signal and background have been performed following the conditions described in Sections 2.4.1.1 and 2.4.1.2 of Chapter 2 for $W^2 = 5\,(\text{GeV/c})^2$ and $W^2 = 10\,(\text{GeV/c})^2$.

The simulation of the signal has been done in two steps. First, 10^6 events were simulated to study the reconstruction efficiency and the detector acceptance. The results of these simulations were later used for the correction of the reconstructed events in a sample with the expected statistics for an integrated luminosity of $\mathcal{L} = 2\,\text{fb}^{-1}$. Second, simulations with realistic statistics were performed to study the feasibility of measuring the channel of interest (reaction in Equation (2.45)).

For the background rejection, at least 10^8 $\bar{p}p \to \pi^+\pi^-\pi^0$ events, following the same angular distribution than the signal, were generated in each case. The

	Reaction	$W^2[\,(\text{GeV/c})^2]$	π^0	N_{events}
Background suppression	$\pi^+\pi^-\pi^0$	5	forward	$\approx 10^8$
	$\pi^+\pi^-\pi^0$	5	backward	$\approx 10^8$
	$\pi^+\pi^-\pi^0$	10	forward	$\approx 10^8$
	$\pi^+\pi^-\pi^0$	10	backward	$\approx 10^8$
Efficiency studies	$e^+e^-\pi^0$	5	forward	$\approx 10^6$
	$e^+e^-\pi^0$	5	backward	$\approx 10^6$
	$e^+e^-\pi^0$	10	forward	$\approx 10^6$
	$e^+e^-\pi^0$	10	backward	$\approx 10^6$
Expected statistics	$e^+e^-\pi^0$	5	forward	150 000
	$e^+e^-\pi^0$	5	backward	150 000
	$e^+e^-\pi^0$	10	forward	6 000
	$e^+e^-\pi^0$	10	backward	6 000

Table 7.1: Number of events simulated for the analysis of $\bar{p}p \to e^+e^-\pi^0$ and rejection of the major background channel, $\bar{p}p \to \pi^+\pi^-\pi^0$, divided in three blocks: background rejection studies, efficiency studies and expected statistics.

	$W^2 = 5\,(\text{GeV/c})^2$	$W^2 = 10\,(\text{GeV/c})^2$
Simulation limits	$3.61 < q^2 < 5.29$	$5.76 < q^2 < 9.18$
Analysis limits	$3.8 < q^2 < 4.2$	$7.00 < q^2 < 8.00$

Table 7.2: q^2 limits for the simulation and analysis of $\bar{p}p \to e^+e^-\pi^0$.

background suppression power was studied with these samples. Table 7.1 shows a compilation of the total number of events simulated for different samples of signal and background. Each simulation has been done in a slightly broader q^2 region than the one selected for the analysis to be able to avoid border effects in the estimation of the reconstruction efficiency. Table 7.2 shows the q^2 limits used for the simulation of the events and the values used for the analysis of the signal.

For the selection of event candidates all possible combinations of two neutral tracks combining in a π^0 candidate and two charged tracks (one positive and one negative) have been performed. In some cases, there are two or more candidates per simulated event but after the cuts chosen for the analysis only the best candidate survives. Several cuts were studied with the goal of suppressing

the major amount of background, but keeping the maximum amount of signal possible. One can find a definition of all the applied cuts in Table 7.3. By applying more restrictive cuts, the amount of misidentified background events is reduced, but also the amount of signal events is decreased. After applying the different cuts, one can compare the amount of signal and background surviving to each one and choose the cut which represents the best compromise of signal and background suppression. The best cut has been selected to be the one that gives the highest signal significance, defined as

$$S_{Sg} = \frac{N_{\text{Cut}}^{Sg}}{\sqrt{N_{\text{Cut}}^{Sg} + N_{\text{Cut}}^{Bg}}}. \tag{7.1}$$

To calculate it with the information from our simulations the same cuts were applied to background and signal samples with high statistics. A background efficiency was defined as

$$\text{Eff}_{Bg} = \frac{N_{\text{Cut}}^{Bg}}{N_{\text{True}}^{Bg}}. \tag{7.2}$$

An analogous definition was used for the signal efficiency,

$$\text{Eff}_{Sg} = \frac{N_{\text{Cut}}^{Sg}}{N_{\text{True}}^{Sg}}. \tag{7.3}$$

In this way we calculated normalized efficiencies.

For each sample, the signal significance has been calculated as a function of the selection cut and taking into account a realistic amount of signal and background events, corresponding to an integrated luminosity of $\mathcal{L} = 2\,\text{fb}^{-1}$, and the expected relation between signal and background events $N_{\text{True}}^{Bg} = 10^6 \cdot N_{\text{True}}^{Sg}$. In this way the signal significance is

$$S_{Sg} = \frac{\text{Eff}_{Sg}\, N_{\text{True}}^{Sg}}{\sqrt{\left(\text{Eff}_{Sg} + 10^6\,\text{Eff}_{Bg}\right) N_{\text{True}}^{Sg}}}. \tag{7.4}$$

A plot with the values of the signal significance as a function of the cut number (cuts are defined in Table 7.3) can be seen in Figure 7.1. The best cut corresponds in the four simulated cases to the selection of exactly one Very Tight electron and one Very Tight positron. The preselection of the event candidates implies that a valid π^0 is also combined. A kinematic fit to the reconstructed tracks, which takes into account energy and momentum conservation, was done under two different hypotheses: $e^+ e^- \pi^0$ and $\pi^+ \pi^- \pi^0$, each one considering the signal or background products respectively. However, the results of the fits were

N_{Cut}	Definition of the cut
1	No additional cuts, only event selection cuts involved
2	Exactly one electron and one positron (2 tracks) with Very Loose probability.
3	Exactly one electron and one positron (2 tracks) with Loose probability.
4	Exactly one electron and one positron (2 tracks) with Tight probability.
5	Exactly one electron and one positron (2 tracks) with Very Tight probability.
6	Cut 5 and Cut 17
7	Cut 5 and Cut 18
8	Cut 5 and Cut 19
9	At least one electron and one positron with Very Loose probability.
10	At least one electron and one positron with Loose probability.
11	At least one electron and one positron with Tight probability.
12	At least one electron and one positron with Very Tight probability.
13	Cut 12 and Cut 17
14	Cut 12 and Cut 18
15	Cut 12 and Cut 19
16	Confidence level for the fit with $e^+e^-\pi^0$ hypothesis greater than 10^{-3}
17	Cut 16 and confidence level for the fit with $e^+e^-\pi^0$ hypothesis greater than the confidence level of the fit with $\pi^+\pi^-\pi^0$ hypothesis
18	Cut 16 and confidence level for the fit with $e^+e^-\pi^0$ hypothesis greater than two times the confidence level of the fit with $\pi^+\pi^-\pi^0$ hypothesis
19	Cut 16 and confidence level for the fit with $e^+e^-\pi^0$ hypothesis greater than three times the confidence level of the fit with $\pi^+\pi^-\pi^0$ hypothesis
20	Cut 16 and confidence level for the fit with $e^+e^-\pi^0$ hypothesis greater than four times the confidence level of the fit with $\pi^+\pi^-\pi^0$ hypothesis

Table 7.3: Definition of the cuts used for the background suppression studies.
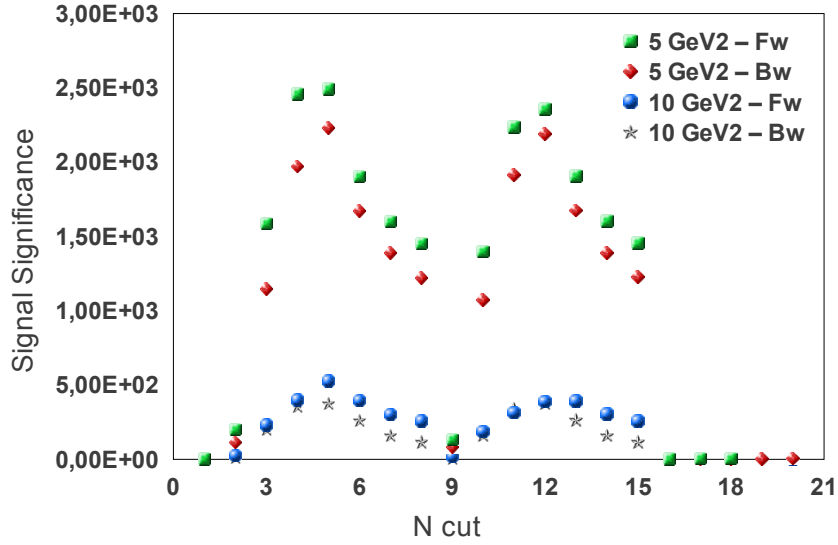
Figure 7.1: Best cut selection analysis: The criteria to select the best cut is based on the maximization of the signal significance. In all cases the cut number 5 is the best one. This cut corresponds to one Very Tight electron combined with one Very Tight positron and requiring only two charged tracks. Two neutral particles combining a π^0 candidate are also required.

not satisfactory and were very similar in both cases. The reason for that is that there were two charged tracks to be fitted together with two neutral candidates combined into a π^0. The minimization process for the fit does not work properly anymore for so many degrees of freedom. In addition, also the resolution of the π^0 in the electromagnetic calorimeter (EMC) is very bad in comparison with the resolution for photons and electrons.

A second way to select the event candidates would be to combine one positive charged track with one negative charged track and look for the missing mass. The missing mass has to correspond to the mass of the undetected π^0. If this condition is fulfilled, the event could be treated as a valid candidate. Although this method has not been used for the analysis presented in this Thesis it would be a future step to follow.

7.2 Background suppression

Applying the selected best cut to the background samples one achieves a background suppression factor close to 10^8 for $W^2 = 5\,(\text{GeV/c})^2$ with the π^0 in forward direction and at least 10^8 for the other cases (see Table 7.4).

Direction	$W^2 = 5\,(\text{GeV/c})^2$	Suppression	$W^2 = 10\,(\text{GeV/c})^2$	Suppression
Forward	2/99210000	$9.92 \cdot 10^7$	0/108000000	$> 1.08 \cdot 10^8$
Backward	1/103460000	$1.03 \cdot 10^8$	3/108280000	$1.08 \cdot 10^8$

Table 7.4: Background suppression factor for the channel $\bar{p}p \to \pi^+\pi^-\pi^0$. In the second and fourth columns are shown the number of misidentified background candidates over the total amount of events generated in the simulation. The corresponding suppression factor is shown in columns three and five.

A study of the remaining background contamination fraction was done with realistic statistics. Table 7.5 shows the results of this study. The expected number of reconstructed signal and background events was calculated using the definitions in Equations (7.2) and (7.3) in the previous Section, starting from the expected amount of True signal and background events. Later, the background contamination in the whole reconstructed sample was defined as

$$\text{Cont}_{Bg} = \frac{N_{\text{Reco}}^{Bg}}{N_{\text{Reco}}^{Sg} + N_{\text{Reco}}^{Bg}}. \tag{7.5}$$

The background contamination remained below 10% for $W^2 = 10\,(\text{GeV/c})^2$ and π^0 backward. For the other simulations, the background contamination was lower than 5% and a measurement of the cross section seems to be possible. These results can be used for disentangling the amount of background events in the reconstructed event samples in $\overline{\text{P}}\text{ANDA}$, where signal events and misidentified background ones are reconstructed together.

7.3   Signal analysis

The first analysis of the signal samples with expected statistics for an integrated luminosity of $\mathcal{L} = 2\,\text{fb}^{-1}$ was done considering that there was no background contamination in the data sample. For the study of the efficiency correction, and to avoid border effects in the estimation of the reconstruction efficiency, the simulations with high statistics were done in an extended q^2 range. An additional cut on q^2 and $\Delta_{T_{\pi^0}}$ was done to select the kinematic region in which we want to measure.

In Figure 7.2 one can see a schematic representation of the cuts done for the study of the efficiency correction. True events simulated outside the $q^2_{\text{min,ana}} < q^2 < q^2_{\text{max,ana}}$ region could be reconstructed inside this region and the other way around. For the efficiency correction calculation the events reconstructed between the kinematic region of interest and the True events simulated

W^2	Forward		Backward	
[(GeV/c)^2]	Signal	Background	Signal	Background
		Expected number of True events		
	N_{True}^{Sg}	N_{True}^{Bg}	N_{True}^{Sg}	N_{True}^{Bg}
5	150000	$1.5 \cdot 10^{11}$	150000	$1.5 \cdot 10^{11}$
10	6000	$6 \cdot 10^9$	6000	$6 \cdot 10^9$
		Efficiencies [%]		
	Eff_{Sg}	Eff_{Bg}	Eff_{Sg}	Eff_{Bg}
5	43.28 ± 0.05	$(2.0 \pm 1.8) \cdot 10^{-6}$	34.09 ± 0.05	$(1.0 \pm 1.4) \cdot 10^{-6}$
10	47.24 ± 0.05	$(0.9 \pm 1.3) \cdot 10^{-6}$	26.04 ± 0.04	$(2.8 \pm 1.9) \cdot 10^{-6}$
		Reconstructed events after efficiencies		
	N_{Reco}^{Sg}	N_{Reco}^{Bg}	N_{Reco}^{Sg}	N_{Reco}^{Bg}
5	64916	3023	51134	1449
10	2834	55	1562	166
		Background Contamination [%]		
	$\text{Cont}_{Bg,Fw}$		$\text{Cont}_{Bg,Bw}$	
5	4.4 $\pm$ 3.7		2.8 $\pm$ 3.8	
10	1.9 $\pm$ 2.7		9.6 $\pm$ 5.8	

Table 7.5: Signal purity calculation taking into account realistic statistics based on an integrated luminosity of $\mathcal{L} = 2\,\text{fb}^{-1}$ for signal and background.
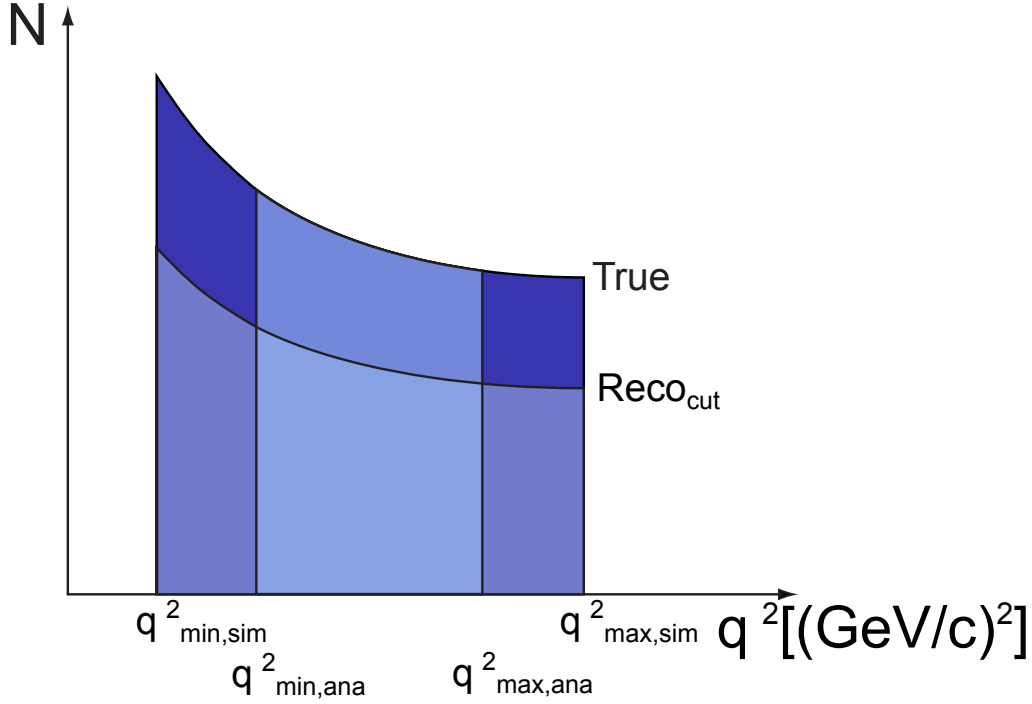
Figure 7.2: Selection of the kinematic region in q^2.

inside the same region were considered. The border effects are reduced in this way. Following the notation in Figure 7.2, the efficiency correction is defined as

$$\text{Corr} = \frac{N_{\text{Reco}}^{Sg}[q_{\text{min,ana}}^2, q_{\text{max,ana}}^2]}{N_{\text{True}}^{Sg}[q_{\text{min,ana}}^2, q_{\text{max,ana}}^2]}. \tag{7.6}$$

Table 7.2 shows the limits in which the efficiency correction has been studied for each simulation. An additional cut $\Delta_{T_{\pi^0}} < 0.5\,\text{GeV/c}$ was also applied to the reconstructed events. In our simulation, the events were always generated at $\Delta_{T_{\pi^0}} = 0\,\text{GeV/c}$. However, the events were reconstructed outside this limit value. For the improvement of the efficiency correction, a new simulation with the π^0 beyond $\Delta_{T_{\pi^0}} = 0.5\,\text{GeV/c}$ is needed, but it could not be done because the event generator was not yet developed. A sample with the expected number of True events simulated for an integrated luminosity of $\mathcal{L} = 2\,\text{fb}^{-1}$ was analysed for each W^2 and π^0 direction using the best cut selected in the background suppression study. The results showed that the measurement of the cross section could be done in all cases (see Table 7.6) keeping the relative error on the reconstruction of signal events below the 5%.

A second analysis introducing the expected fraction of misidentified background events in the sample was done. The amount of misidentified events was statistically estimated using the background contamination value (Equa-

Simulation	N^{Sg}_{True}	$N^{Sg}_{Reconstructed}$	$N^{Sg}_{Corrected}$
5 (GeV/c)^2 - fw	72263 $\pm$269	30661 $\pm$ 175	72732 $\pm$ 433
5 (GeV/c)^2 - bw	72405 $\pm$269	25386 $\pm$ 159	73164 $\pm$ 488
10 (GeV/c)^2 - fw	1336 $\pm$37	662 $\pm$ 26	1319 $\pm$ 51
10 (GeV/c)^2 - bw	1313 $\pm$ 36	394 $\pm$ 20	1312 $\pm$ 66

Table 7.6: Analysis of $\bar{p}p \rightarrow e^+e^-\pi^0$ without taking into account the background contamination.

Simulation	$N^{Sg+Bg}_{Reconstructed}$	$N^{Sg}_{Extracted}$	Relative Error [%]
5 (GeV/c)^2-fw	31967 $\pm$ 179	30544 $\pm$ 1190	4
5 (GeV/c)^2-bw	26067 $\pm$ 162	25348 $\pm$ 1601	4
10 (GeV/c)^2-fw	674 $\pm$ 26	661 $\pm$ 31	5
10 (GeV/c)^2-bw	429 $\pm$ 21	387 $\pm$ 31	8

	$N^{Sg}_{Corrected}$	Relative Error [%]
5 (GeV/c)^2-fw	72454 $\pm$ 2825	4
5 (GeV/c)^2-bw	73055 $\pm$ 2889	4
10 (GeV/c)^2-fw	1317 $\pm$ 62	5
10 (GeV/c)^2-bw	1289 $\pm$ 104	8

Table 7.7: Analysis of $\bar{p}p \rightarrow e^+e^-\pi^0$ taking into account the background contamination fraction.

tion (7.5)) calculated in Table 7.5. The total amount of reconstructed events was taken to be the sum of the reconstructed events in the sample without background contamination plus the calculated fraction of misidentified events,

$$N^{Sg+Bg}_{Reconstructed} = N^{Sg}_{Reconstructed} + N^{Bg}_{Estimated}. \tag{7.7}$$

The result was taken as the real number of events that would be measured by $\overline{\text{P}}$ANDA. From this new sample, the fraction of signal and background events had to be calculated again using the values in Table 7.5. Finally, the calculated fraction of signal events was corrected using the calculated value for the efficiency correction, extracted from the simulation of signal with high statistics. Table 7.7 shows the results of this last analysis. In all the calculations shown here, only statistical errors have been considered [112]. The measurement of the number of events in the kinematic region of our interest could be done within a relative error lower than 8%, being this the value in the worst case. The number of measured events have been corrected integrating the number of events on q^2. The study done for the background contamination fraction is valid only for the integrated cross section in q^2. The determination of the integrated number of events has the advantage that it minimizes the statistical error.

A study of the angular distribution of the events as a function of q^2 using only few bins (~ 5) could be done without taking into account the background contamination. In Figure 7.3 one can see how the corrected signal would look in this case. However, to be able to perform this kind of analysis taking into account the background, a more detailed estimation of the background suppression bin per bin is needed. So far this was impossible to do due to the huge amount of simulated background events needed to perform this study (more than 10^{10} events per case), which is translated in a computational time constraint. The discrepancies between the simulated signal and the corrected signal, specially for the case at $W^2 = 10\,(\text{GeV/c})^2$ and the π^0 backward, come from statistical fluctuations and due to the small cross section in this case. This can be easily check by increasing the amount of bins in the histogram (see Figure 7.4). As an effect of the random event generator, there are less events in the last bins in the histograms in which the bin size is bigger, but the events appear consistently distributed if one decreases the bin size.

Using the integrated luminosity, one can measure the integrated cross section of (2.45) in the region calculated in Reference [62]. The comparison of the measured cross section to the theoretical predictions constitutes a test of the TDA production mechanism.

The results of these simulations show that such a comparison could be done with data taken by $\overline{\text{P}}$ANDA. Although new event generators for signal and background are needed, the simulations presented here represent the worst possible scenario for the separation of signal and background. Therefore, an im-
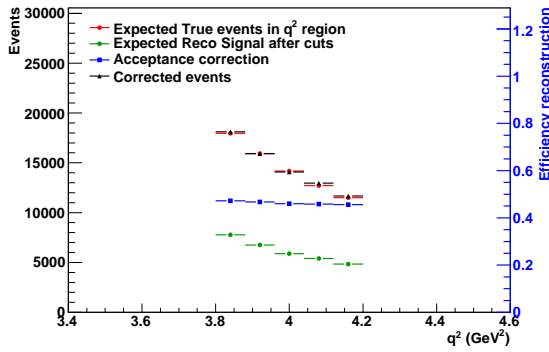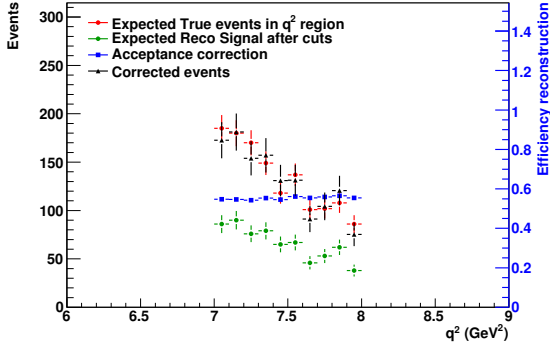
(a) $W^2 = 5\,(\text{GeV/c})^2$, π^0 forward
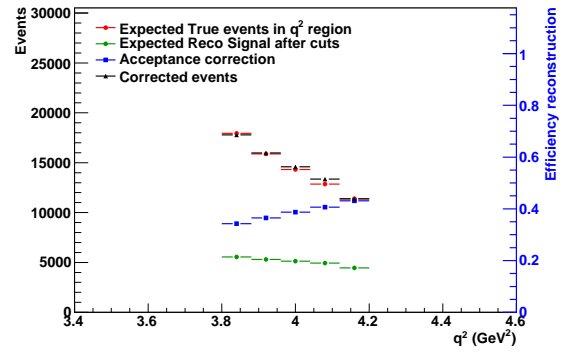
(b) $W^2 = 5\,(\text{GeV/c})^2$, π^0 backward
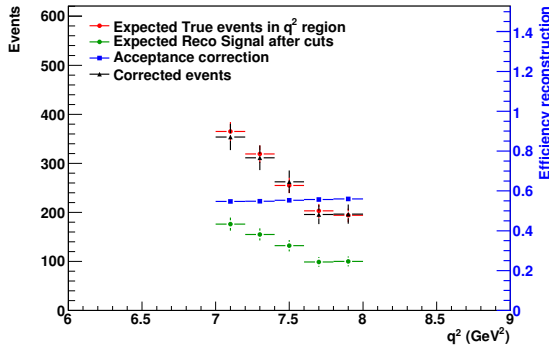
(c) $W^2 = 10\,(\text{GeV/c})^2$, π^0 forward
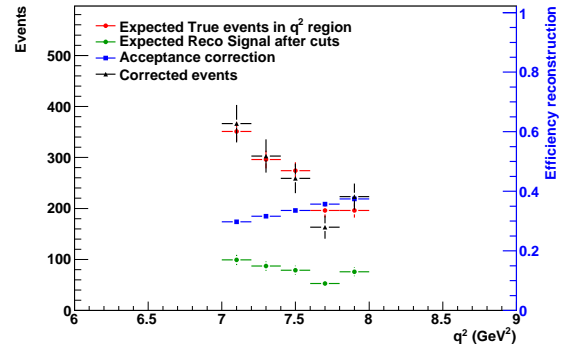
(d) $W^2 = 10\,(\text{GeV/c})^2$, π^0 backward

Figure 7.3: Reconstruction and correction of the q^2 angular distribution of the reaction $\bar{p}p \to e^+e^-\pi^0$. The background contamination is not taken into account.
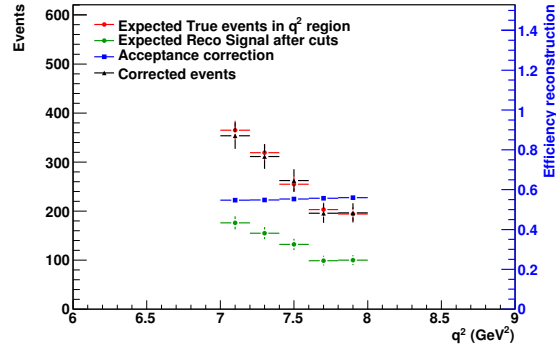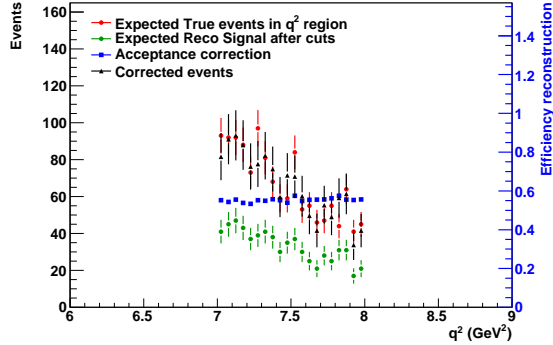
(a) $W^2 = 10\,(\text{GeV/c})^2$, π^0 forward, 5 bins

(b) $W^2 = 10\,(\text{GeV/c})^2$, π^0 forward, 10 bins

(c) $W^2 = 10\,(\text{GeV/c})^2$, π^0 forward, 20 bins

Figure 7.4: Influence of the bin size in the statistic fluctuations. With bigger bins, it seems to be an inconsistency in the number of events in the last bins of the histogram. However, by decreasing the bin size, one can see that the events are nevertheless, consistently distributed following the defined q^2 angular distribution.

112

provement in the results is expected with more realistic background and signal event generators.

8

Conclusion and outlook

In this thesis several studies related to the $\overline{\text{P}}$ANDA detector at FAIR have been exposed. In particular, two of them are related with the study of the electromagnetic form factors (EMFF) of the proton and the transition distribution amplitudes (TDA). The other one is related to the development of the backward endcap of the electromagnetic calorimeter (BWEMC) of $\overline{\text{P}}$ANDA. The importance of the hadron structure study is intimately related with the improvement of our knowledge of the strong force in the low energy regime. The EMFF are very suitable variables to understand the proton structure. The EMFF can be measured via electron elastic scattering in the space-like region, and via electron or proton annihilation processes ($e^+e^- \to \bar{p}p$ or $\bar{p}p \to e^+e^-$) in the time-like region. The detector $\overline{\text{P}}$ANDA will offer a unique opportunity to measure the annihilation of proton-antiproton into electron-positron pairs. The high luminosity that will be achieved in $\overline{\text{P}}$ANDA will increase the statistics in the measurement of this reaction compared to previous experiments allowing the determination of the proton EMFF with precision at least one order of magnitude better in a wide q^2 range.

Feasibility studies of measuring proton EMFF at $\overline{\text{P}}$ANDA have been presented. Realistic Monte Carlo simulations have been performed taking into account the geometry, the material budget and the performance of the future detector, as well as its tracking efficiency and particle identification power. Several background reactions have been considered, with particular attention to two body hadron production due to its close kinematic similarity to the signal process. The results show that, applying combined particle identification (PID) criteria and kinematic constraints, it is possible to reach a background to signal ratio of the order of 0.1%, which is sufficient to ensure a clean identification of e^+e^- pairs corresponding to the reaction of interest ($\bar{p}p \to e^+e^-$). The ra-

tio $|G_E|/|G_M|$, which was measured by BaBar with a 40% uncertainty, will be measured by $\overline{P}$ANDA with a precision of few percent, increasing the precision by at least a factor 10 with respect to previous measurements. The ratio of the electric to the magnetic form factor will be measurable until $q^2 \simeq 14\,(\text{GeV/c})^2$, with an error comparable to the existing data taken at much lower q^2. Above this value it is still possible to extract a generalized form factor from the total cross section and test its asymptotic and analytic properties. With a good luminosity measurement the form factors $|G_E|$ and $|G_M|$ can be extracted individually.

The study of the efficiency and energy resolution of the BWEMC was also of significant importance for these studies. The good detection of electrons and photons in the backward direction is mandatory to be able to measure the channel $\bar{p}p \to e^+e^-\pi^0$, important in the TDA approach. Several simulations were performed to study these characteristics, taking into account the BWEMC geometry and the dead material introduced by other detectors placed in front of our calorimeter. The results showed that the efficiency and energy resolution are sufficient to detect electrons and photons in different energy ranges and traversing different thicknesses of dead material. Only in some small spots the efficiency was lowered very much due to the material budget in front of the calorimeter. However, this was not affecting the energy resolution, which stays around the expected values.

At higher energies, a second approach to study the hadron structure is the use of TDA. TDA are new non-perturbative objects describing the transition between a baryon and a meson. They are used in the cross section calculation of hard exclusive processes. The validity of this approach can be investigated in $\overline{P}$ANDA by measuring the cross section of $\bar{p}p \to e^+e^-\pi^0$ and comparing the results with the theory values. Dedicated simulations have been done to study the feasibility of measuring this cross section. The main background channel, $\bar{p}p \to \pi^+\pi^-\pi^0$, was taken into account. For the simulation of signal, the event generator was based on the cross section calculation available for $\bar{p}p \to e^+e^-\pi^0$ using the TDA approach. This calculation is done for zero transverse momentum of the pion. Although a new event generator for non-zero transverse momenta for the pion is needed, no big differences in the reconstruction efficiency of the signal in the kinematic region of interest are expected. The cross section of the main background channel was unknown at the moment the simulations were done. To be able to perform the studies, the background was simulated using the same angular distribution as the signal and it was supposed to be 10^6 times higher. The first assumption was taken because that represents the worst case for the suppression of background, being then a very conservative approach. A good background suppression under these conditions is very promising because it can be improved with a more realistic background angular distribution. The background to signal cross section ratio was chosen to be 10^6 following the average value taken for the study of $\bar{p}p \to e^+e^-$ reconstruction. Dedicated theory work is being done in order to calculate the background channel cross section

to perform a better simulation. The results showed that the signal cross section can be measured with a relative error of about 8% in the worst case, sufficient precision for a first comparison to the predictions given in the TDA approach.

In this Thesis it has been shown that $\overline{\text{P}}$ANDA is an ideal tool to study nucleon structure observables with high precision. The key point in these studies has been the clean separation of a dilepton signal from hadronic background with very high efficiency. One can expect that this clean identification of dileptons can be used to measure other electromagnetic processes like for example Drell-Yan.

A

Electromagnetic form factors fits

This Appendix includes the results of the fits to the reconstructed corrected and angular distributions of $\bar{p}p \to e^+e^-$. For the correction of the reconstructed distributions, the result of simulations with high statistics and flat angular distributions which studied the acceptance of the detector have been used. Only one result for one fit is shown in each case.

The results of the fits can be seen in Table A.1 and a plot summarizing them is shown in Figure A.4. The analysis for $q^2 = 1.7\,\text{GeV/c}$, $q^2 = 10.9\,\text{GeV/c}$ and $q^2 = 13.4\,\text{GeV/c}$ is not shown because no data samples were generated using a flat distribution with these q^2 values. For these cases, the acceptance correction was calculated using a sample with the same angular distribution as the signal but high statistics, which is a very good approximation. However the results of the fits are not shown here. Moreover, an additional simulation for $q^2 = 7.6\,\text{GeV/c}$ is also shown.

q^2 (GeV/c)^2	p_{beam} [GeV/c]	Simulated	Expected	Assumption	$\mathcal{R} = |G_E|/|G_M|$	Error$_\mathcal{R}$
7.3	2.87	10^6	124491	0	1.85e-04	1.09e-01
				1	9.68e-01	3.93e-02
				3	3.10e+00	1.02e-01
7.6	2.99	10^6	103466	0	6.89e-04	2.52e-01
				1	9.97e-01	4.30e-02
				3	3.11e+00	1.09e-01
8.2	3.30	10^6	64739	0	1.93e-06	1.78e-01
				1	9.92e-01	5.57e-02
				3	3.22e+00	1.40e-01
11.0	4.85	10^6	9078	0	2.43e-01	5.60e-01
				1	1.02e+00	1.89e-01
				3	3.41e+00	3.93e-01
12.9	5.86	10^6	3204	0	3.82e-01	7.82e-01
				1	6.16e-01	5.02e-01
				3	3.25e+00	6.45e-01
13.8	6.38	10^6	1985	0	6.50e-01	7.20e-01
				1	1.26e+00	5.29e-01
				3	2.76e+00	6.92e-01
16.7	7.90	10^6	572	0	9.52e-04	2.07e+00
				1	1.07e+00	1.35e+00
				3	2.83e+00	1.75e+00

Table A.1: Results of the fits for the extraction of the ratio $\mathcal{R}$ between the EMFF
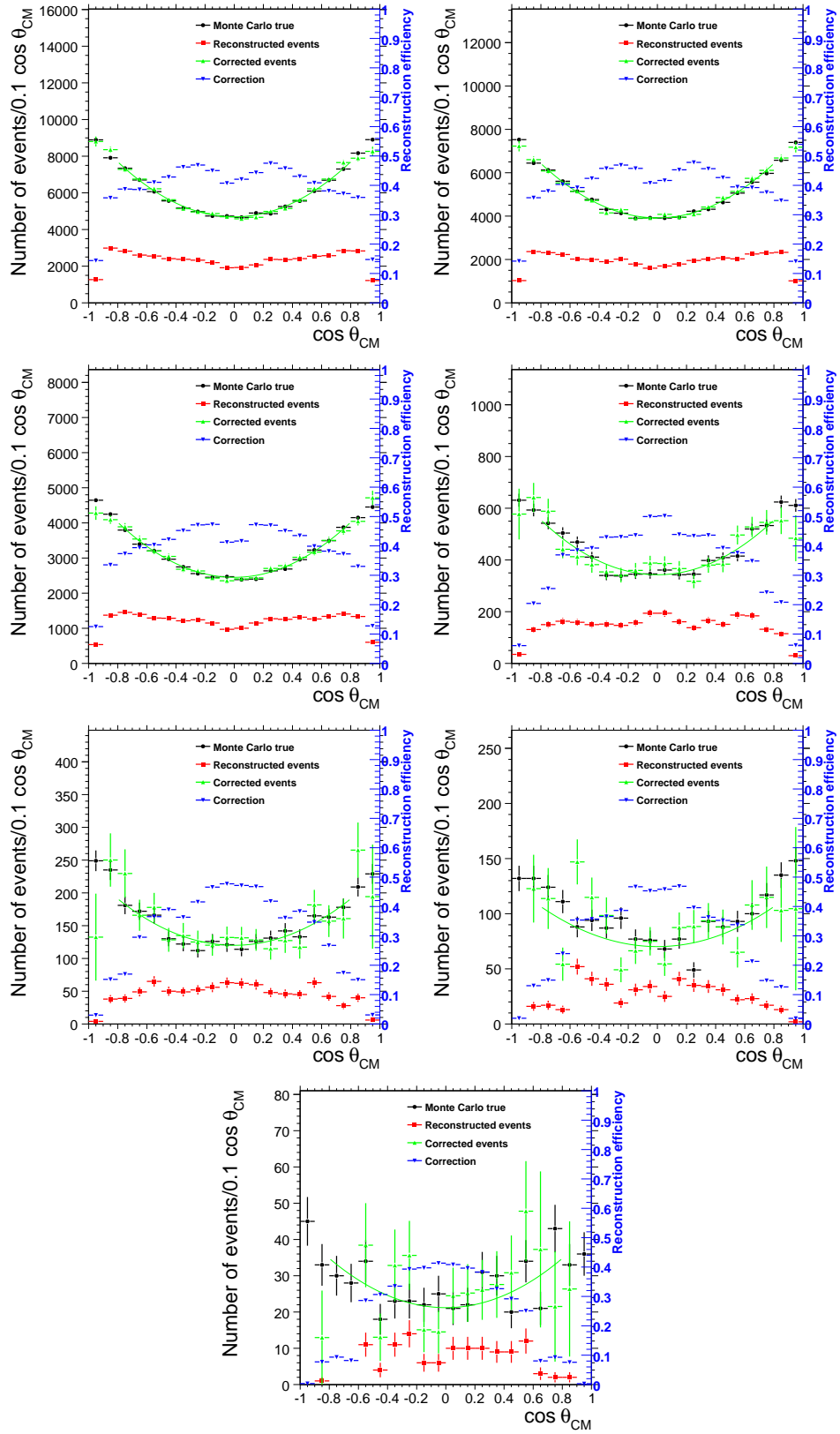
Figure A.1: Angular distribution reconstruction at different q^2 values for the assumption $|G_E| = 0$ and using isotropic distribution for the acceptance correction. From left to right and top to bottom $q^2 = 7.27, 8.21, 11.0, 12.9, 13.8, 16.7$ (GeV/c)^2.
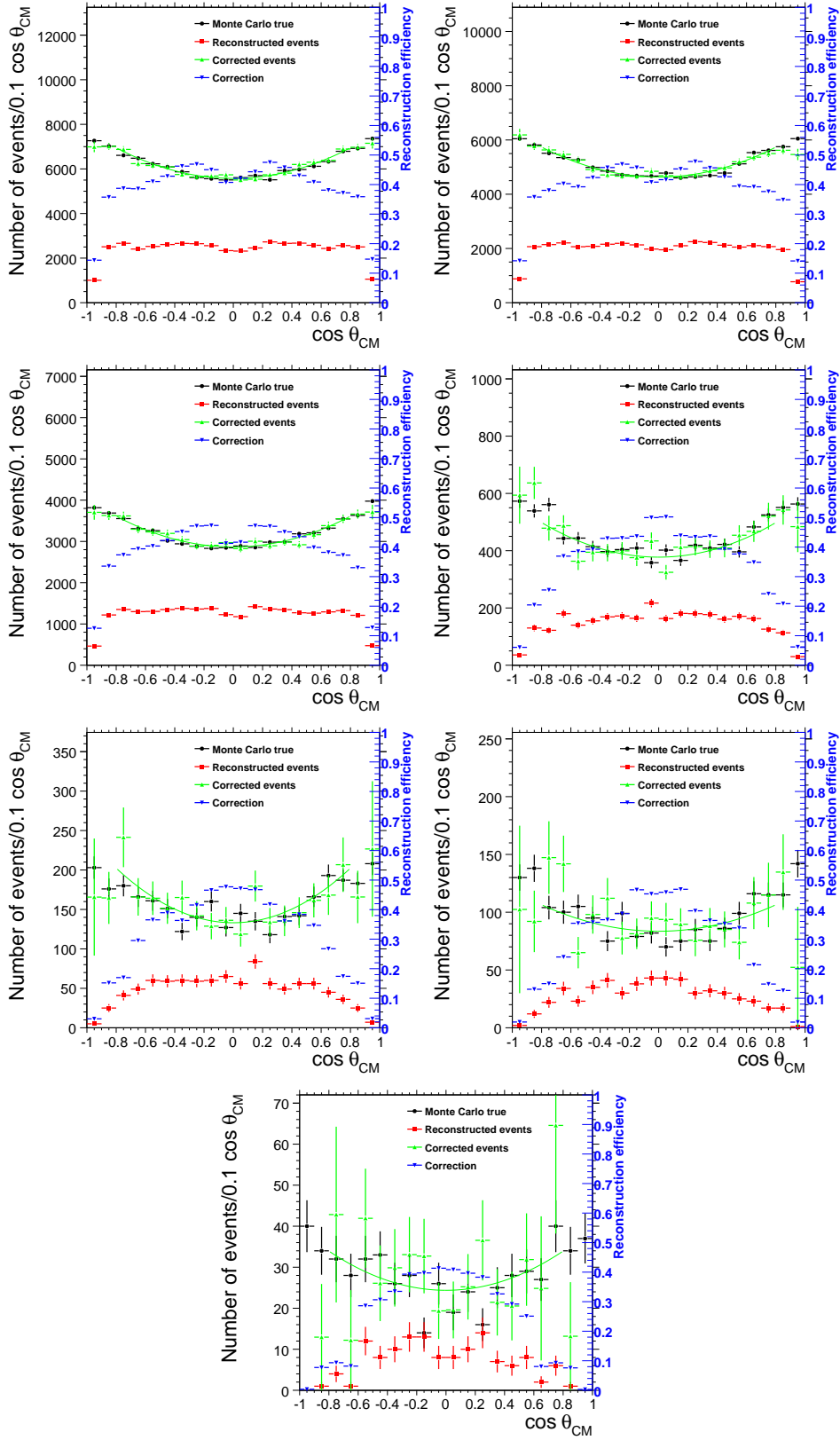
Figure A.2: Angular distribution reconstruction at different q^2 values for the assumption $|G_E| = |G_M|$ and using isotropic distribution for the acceptance correction. From left to right and top to bottom $q^2 = 7.27, 8.21, 11.0, 12.9, 13.8, 16.7 \, (\text{GeV}/c)^2$.
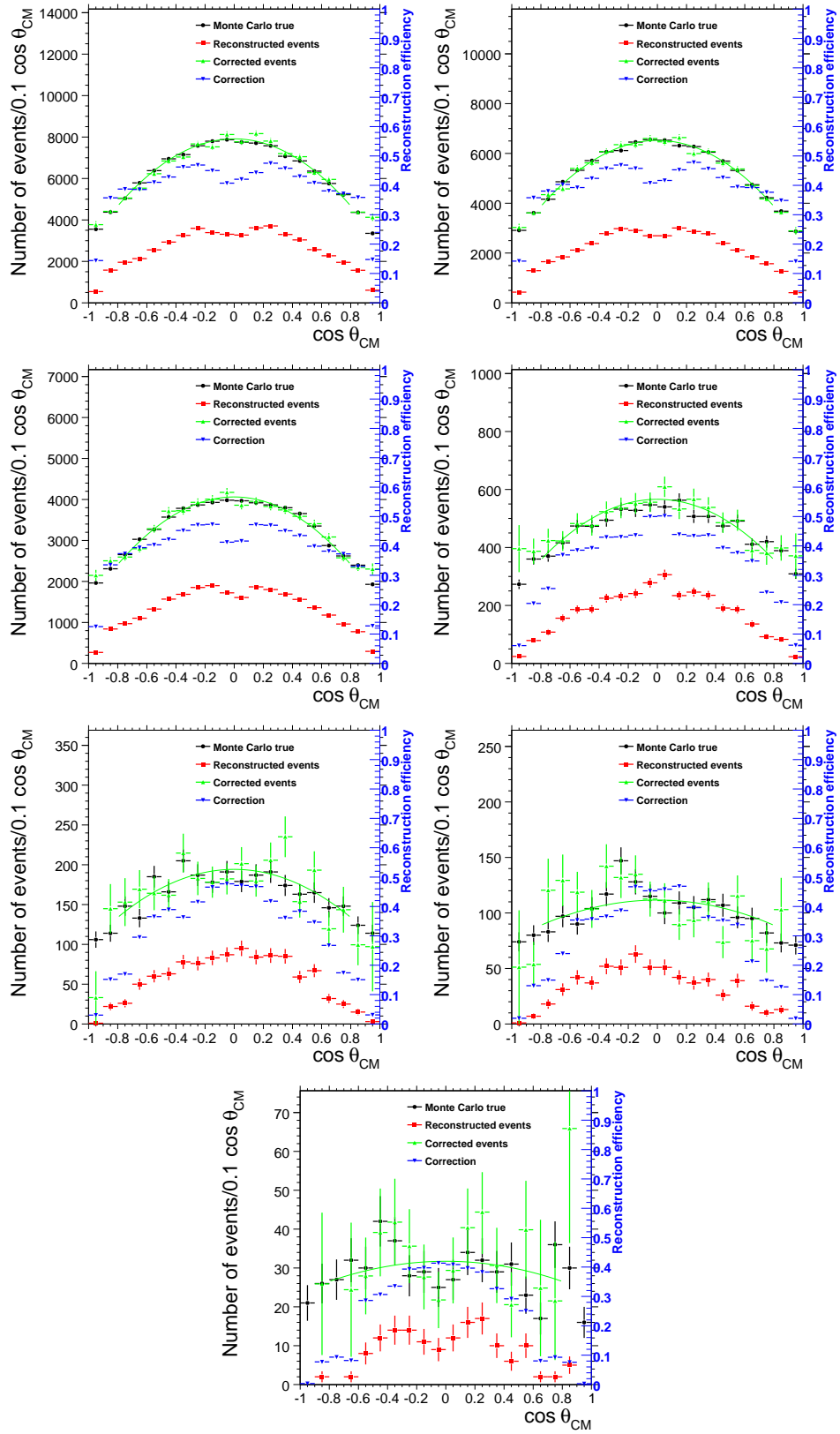
Figure A.3: Angular distribution reconstruction at different q^2 values for the assumption $|G_E| = 3 \cdot |G_M|$ and using isotropic distribution for the acceptance correction. From left to right and top to bottom $q^2 = 7.27, 8.21, 11.0, 12.9, 13.8, 16.7 \, (\text{GeV/c})^2$.
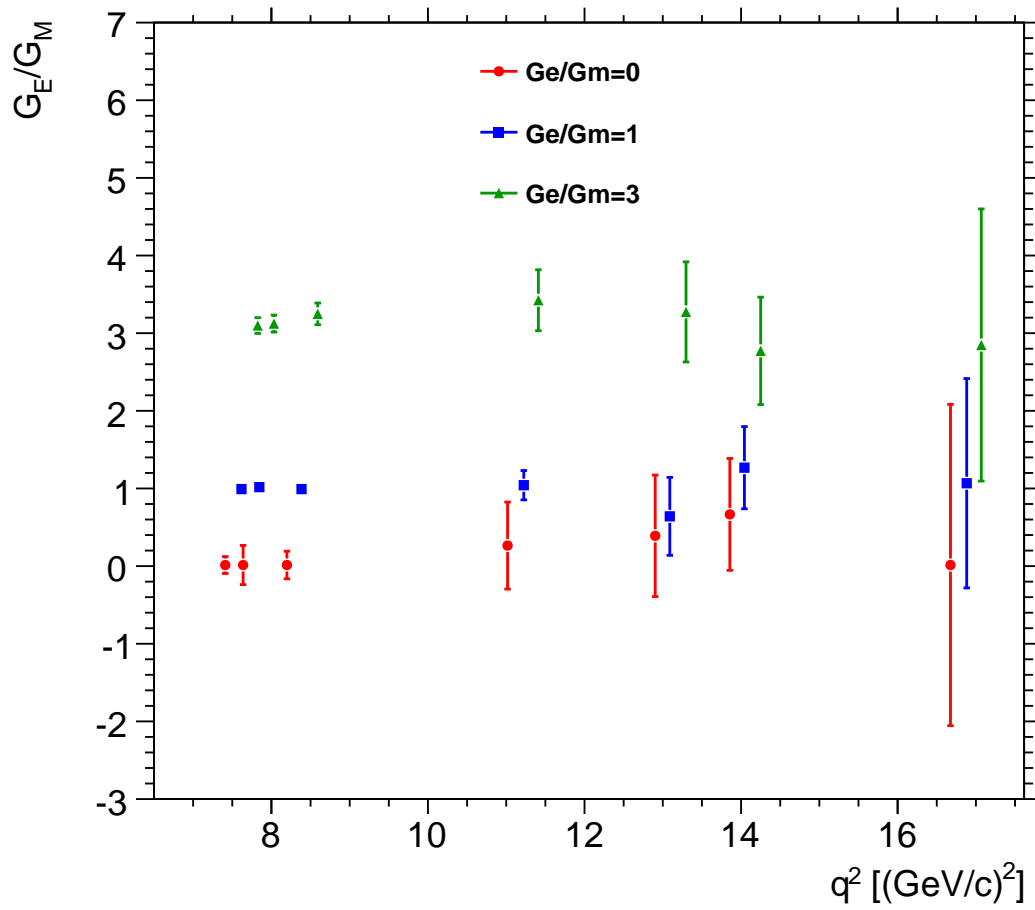
Figure A.4: Result of $\mathcal{R} = |G_E|/|G_M|$ as a function of q^2 expected from the simulations.

B

Electromagnetic calorimeter energy resolution and efficiency

This Appendix shows the results of the analysis done for the study of the BWEMC energy resolution and efficiency.

The plots show the results of the simulations done covering half a quarter of the BWEMC. The simulations were done for five different photon energies: 30 MeV, 100 MeV, 250 MeV, 500 MeV and 700 MeV.

(a)

(b)
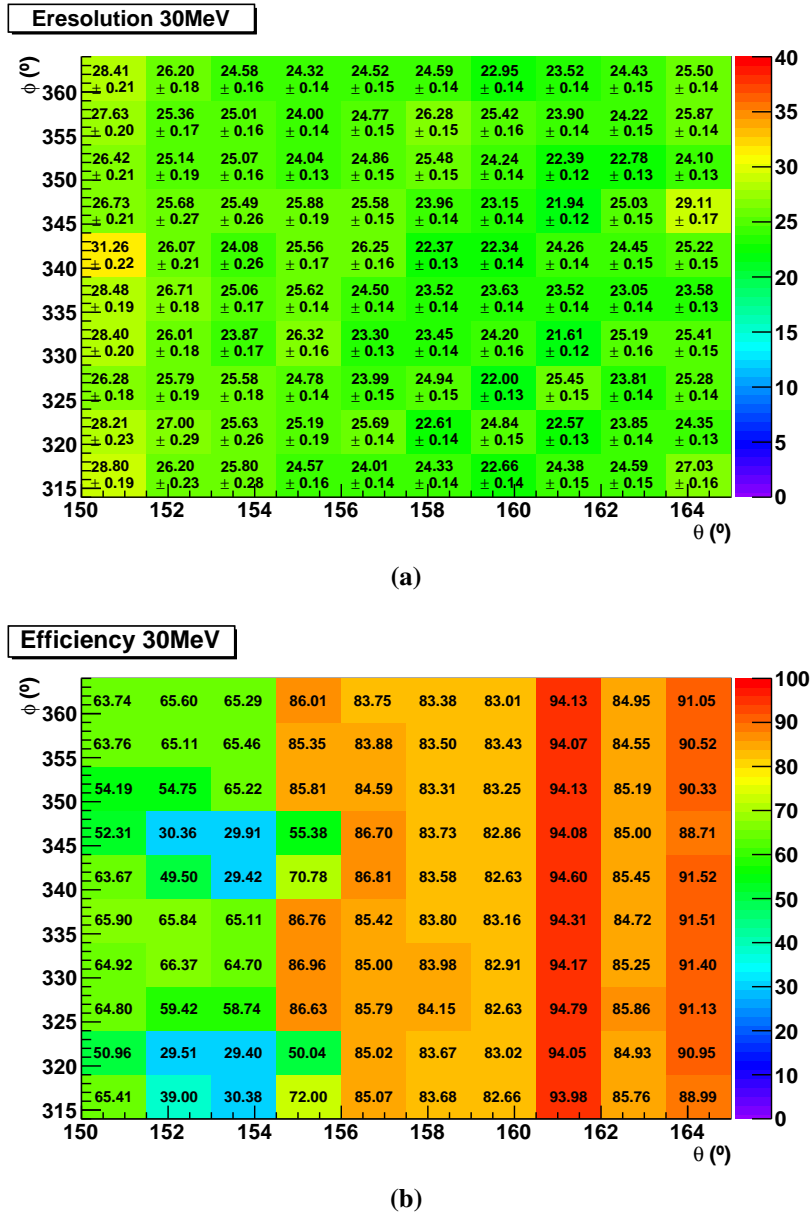
Figure B.1: Energy resolution and efficiency map for the simulation with 30 MeV photons.
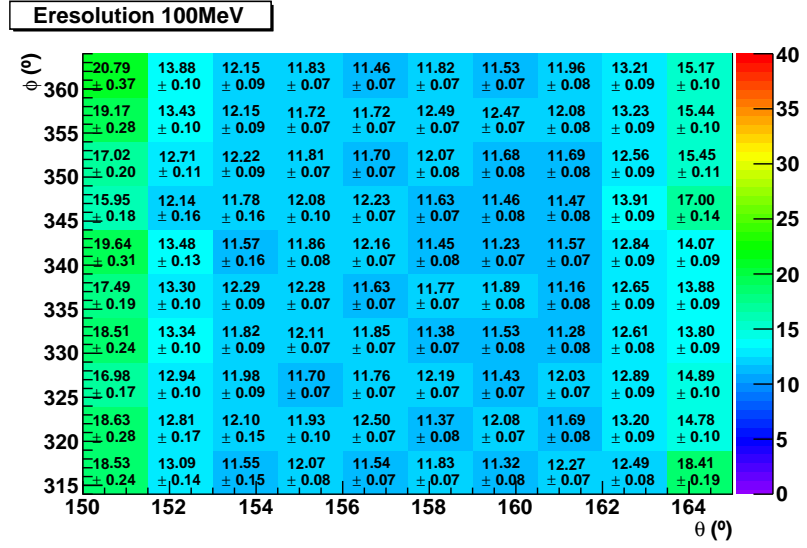
(a)
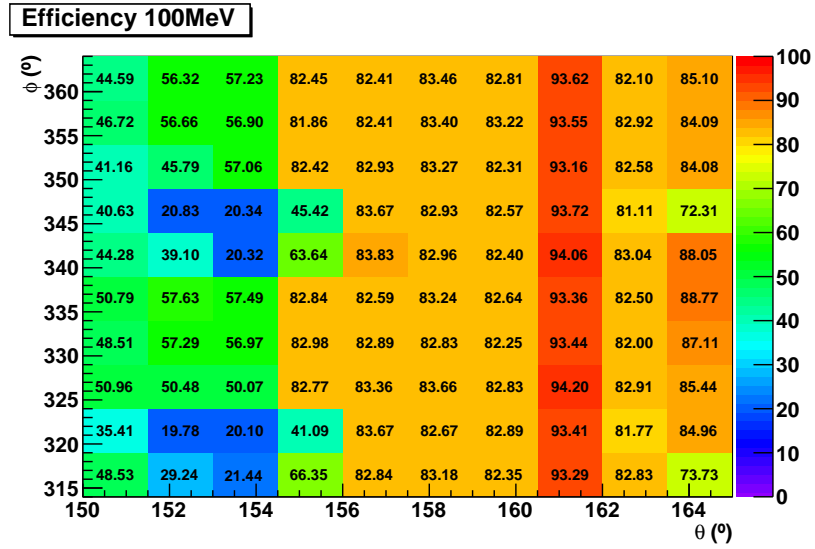
(b)

Figure B.2: Energy resolution and efficiency map for the simulation with 100 MeV photons.

(a)

(b)

Figure B.3: Energy resolution and efficiency map for the simulation with 250 MeV photons.

Eresolution 500MeV

φ (º) vs θ (º)

φ \ θ										
360	26.75 ± 3.69	9.82 ± 0.09	5.43 ± 0.04	4.76 ± 0.02	4.66 ± 0.02	4.70 ± 0.02	4.72 ± 0.02	4.94 ± 0.02	6.16 ± 0.03	9.51 ± 0.06
355	22.21 ± 1.86	8.89 ± 0.08	5.23 ± 0.04	4.69 ± 0.02	4.69 ± 0.02	5.05 ± 0.02	5.67 ± 0.03	5.18 ± 0.02	6.20 ± 0.03	10.29 ± 0.07
350	19.07 ± 0.79	7.42 ± 0.09	4.94 ± 0.04	4.63 ± 0.02	4.78 ± 0.02	5.04 ± 0.02	4.77 ± 0.02	4.88 ± 0.02	5.83 ± 0.03	10.96 ± 0.08
345	14.31 ± 0.29	5.92 ± 0.11	4.38 ± 0.06	4.37 ± 0.04	5.03 ± 0.02	4.75 ± 0.02	4.78 ± 0.02	4.74 ± 0.02	6.59 ± 0.04	10.36 ± 0.07
340	37.96 ± 7.05	9.77 ± 0.13	4.44 ± 0.07	4.55 ± 0.03	4.79 ± 0.02	4.68 ± 0.02	4.69 ± 0.02	4.65 ± 0.02	5.77 ± 0.03	6.96 ± 0.04
335	16.23 ± 0.41	8.17 ± 0.07	5.18 ± 0.04	4.89 ± 0.02	4.72 ± 0.02	4.70 ± 0.02	4.77 ± 0.02	4.77 ± 0.02	5.64 ± 0.03	7.46 ± 0.04
330	20.97 ± 1.18	9.07 ± 0.08	5.25 ± 0.04	4.93 ± 0.02	4.64 ± 0.02	4.68 ± 0.02	4.79 ± 0.02	4.65 ± 0.02	6.05 ± 0.03	7.72 ± 0.04
325	18.77 ± 0.59	7.79 ± 0.08	5.03 ± 0.04	4.76 ± 0.02	4.63 ± 0.02	4.79 ± 0.02	4.76 ± 0.02	4.97 ± 0.02	5.79 ± 0.03	7.27 ± 0.04
320	20.09 ± 1.25	7.23 ± 0.17	4.66 ± 0.07	4.50 ± 0.04	4.73 ± 0.02	4.71 ± 0.02	4.86 ± 0.02	4.89 ± 0.02	5.95 ± 0.03	9.02 ± 0.06
315	19.84 ± 1.00	8.31 ± 0.14	4.64 ± 0.07	4.75 ± 0.03	4.70 ± 0.02	4.78 ± 0.02	4.81 ± 0.02	5.25 ± 0.02	6.45 ± 0.03	17.69 ± 0.64

θ (º): 150, 152, 154, 156, 158, 160, 162, 164

(a)

Efficiency 500MeV

φ \ θ										
360	25.36	55.23	52.73	82.10	83.46	84.07	84.53	94.24	85.11	86.93
355	30.10	54.10	52.10	82.07	83.63	85.17	85.20	93.92	85.12	84.13
350	30.69	40.54	51.32	81.90	84.41	85.32	84.53	93.96	85.09	81.80
345	32.76	15.03	14.21	39.45	84.54	84.39	84.29	94.29	85.75	87.08
340	25.83	35.78	13.95	60.52	84.35	84.01	84.96	94.17	86.01	90.11
335	42.90	54.92	52.15	82.96	83.68	84.02	85.47	94.48	85.93	88.62
330	34.96	55.53	52.07	83.12	83.39	85.03	85.35	94.25	85.60	88.57
325	40.38	46.88	44.67	82.86	83.07	85.31	84.75	94.52	85.47	90.57
320	24.59	14.44	14.24	34.92	84.40	84.44	85.75	94.50	85.53	87.63
315	35.91	23.30	14.97	63.99	84.13	84.88	85.16	93.67	85.99	52.29

θ (º): 150, 152, 154, 156, 158, 160, 162, 164

(b)

Figure B.4: Energy resolution and efficiency map for the simulation with 500 MeV photons.

(a)

(b)

Figure B.5: Energy resolution and efficiency map for the simulation with 700 MeV photons.

C

Paper publication

This Appendix includes a copy of the published article in **The European Physical Journal A 44, 373-384 (2010)**, which includes part of the work done in the framework of the present Thesis.

Content deleted due to copyright

Content deleted due to copyright

Content deleted due to copyright

Content deleted due to copyright

Content deleted due to copyright

Content deleted due to copyright

Content deleted due to copyright

Content deleted due to copyright

Content deleted due to copyright

Content deleted due to copyright

List of Figures

145

146

List of Tables

List of acronymes

AOD analysis object cata

BWEMC backward endcap of the electromagnetic calorimeter

CAD computer aided design

CM center of mass

DCH drift chambers

DIRC detector for internally reflected Cherenkov light

DVCS deep virtual Compton scattering

EMC electromagnetic calorimeter

EMFF electromagnetic form factors

ESD event summary data

FAIR Facility for Antiproton and Ion Research

FS forward spectrometer

FSEMC electromagnetic calorimeter in the forward spectrometer

FWEMC forward endcap of the electromagnetic calorimeter

FWHM full width at half maximum

GEM gas electron multiplier

GPD general parton distributions

HESR High Energy Storage Ring

HL high luminosity

HR high resolution

LAAPD large area avalanche photodiodes

MCP PMT micro-channel plate multiplier detectors

MLP multilayer perceptron

MUO muon counters

MVD micro vertex detector

OPE one-photon exchange

P̅ANDA antiP̅roton ANnihilations at DArmstadt

PID particle identification

QCD quantum chromodynamics

QED quantum electrodynamics

RICH ring imaging Cherenkov counter

STT straw tube tracker

TDA transition distribution amplitudes

TS target spectrometer

TSEMC electromagnetic calorimeter in the target spectrometer

TOF time-of-flight

VMD vector meson dominance

VPT vacuum photo-triodes

VPTT vacuum photo-tetrodes

XML extensible markup language

Bibliography

[1] M. Andreotti *et al.*, "Measurements of the magnetic form-factor of the proton for timelike momentum transfers," *Phys.Lett.*, vol. B559, pp. 20–25, 2003.

[2] G. Bardin *et al.*, "Determination of the electric and magnetic form-factors of the proton in the timelike region," *Nucl.Phys.*, vol. B411, pp. 3–32, 1994.

[3] B. Pire and L. Szymanowski, "Hadron annihilation into two photons and backward VCS in the scaling regime of QCD," *Phys.Rev.*, vol. D71, p. 111501, 2005.

[4] M. F. M. Lutz *et al.*, "Physics Performance Report for PANDA: Strong Interaction Studies with Antiprotons," tech. rep., PANDA Collaboration, 2009.

[5] M. Sudol *et al.*, "Feasibility studies of the time-like proton electromagnetic form factor measurements with PANDA at FAIR," *Eur. Phys. J.*, vol. A44, pp. 373–384, 2010.

[6] I. Esterman, R. Frisch, and O. Stern, "Magnetic moment of the proton," *Nature*, vol. 132, pp. 169–170, 1933.

[7] R. Hofstadter, "Electron scattering and nuclear structure," *Rev.Mod.Phys.*, vol. 28, pp. 214–254, 1956.

[8] R. W. Mcallister and R. Hofstadter, "Elastic scattering of 188 MeV electrons from the proton and the alpha particle," *Phys.Rev.*, vol. 102, pp. 851–856, 1956.

[9] R. Hofstadter *et al.*, "Electromagnetic structure of the proton and neutron," *Rev.Mod.Phys.*, vol. 30, p. 482, 1958.

[10] R. G. Sachs, "High-Energy Behavior of Nucleon Electromagnetic Form Factors," *Phys. Rev.*, vol. 126, pp. 2256–2260, 1962.

[11] E. J. Geis, *The Electric Form Factor of the Neutron at low momentum transfers as measured at BATES large acceptance spectrometer toroid.* PhD thesis, Arizona State University, May 2007.

[12] M. N. Rosenbluth, "High Energy Elastic Scattering of Electrons on Protons," *Phys.Rev.*, vol. 79, pp. 615–619, 1950.

[13] L. N. Hand, "Electric and Magnetic Formfactor of the Nucleon," *Rev.Mod.Phys.*, vol. 35, p. 335, 1963.

[14] T. Janssens *et al.*, "Proton form factors from elastic electron-proton scattering," *Phys.Rev.*, vol. 142, pp. 922–931, 1966.

[15] D. H. Coward *et al.*, "Electron-proton elastic scattering at high momentum transfers," *Phys.Rev.Lett.*, vol. 20, pp. 292–295, 1968.

[16] J. Litt *et al.*, " Measurement of the ratio of the proton form-factors, G_E/G_M, at high momentum transfers and the question of scaling," *Phys.Lett.*, vol. B31, pp. 40–44, 1970.

[17] L. E. Price *et al.*, "Backward-angle electron-proton elastic scattering and proton electromagnetic form-factors," *Phys.Rev.*, vol. D4, pp. 45–53, 1971.

[18] C. Berger *et al.*, "Electromagnetic form factors of the proton at squared four momentum transfers between 10 and 50 fm^2," *Phys.Lett.*, vol. B35, p. 87, 1971.

[19] W. Bartel *et al.*, "Measurement of proton and neutron electromagnetic form-factors at squared four momentum transfers up to $3\,\text{GeV/c}^2$," *Nucl.Phys.*, vol. B58, pp. 429–475, 1973.

[20] K. Hanson *et al.*, "Large angle quasielastic electron-deuteron scattering," *Phys.Rev.*, vol. D8, pp. 753–778, 1973.

[21] F. Borkowski *et al.*, "Electromagnetic Form-Factors of the Proton at Low Four-Momentum Transfer," *Nucl.Phys.*, vol. B93, p. 461, 1975.

[22] A. F. Sill *et al.*, "Measurements of elastic electron-proton scattering at large momentum transfer," *Phys.Rev.*, vol. D48, pp. 29–55, 1993.

[23] G. G. Simon *et al.*, "Absolute electron Proton Cross-Sections at Low Momentum Transfer Measured with a High Pressure Gas Target System," *Nucl.Phys.*, vol. A333, pp. 381–391, 1980.

[24] L. Andivahis *et al.*, "Measurements of the electric and magnetic form-factors of the proton from $Q^2 = 1.75\,\text{GeV/c}^2$ to $8.83\,\text{GeV/c}^2$," *Phys.Rev.*, vol. D50, pp. 5491–5517, 1994.

[25] R. C. Walker *et al.*, "Measurements of the proton elastic form-factors for $1\,\text{GeV/c}^2 < \text{Q}^2 < 3\,\text{GeV/c}^2$ at SLAC," *Phys.Rev.*, vol. D49, pp. 5671–5689, 1994.

[26] M. E. Christy *et al.*, "Measurements of electron proton elastic cross-sections for $0.4 < Q^2 < 5.5$ $(\text{GeV/c})^2$," *Phys.Rev.*, vol. C70, p. 015206, 2004.

[27] I. Qattan *et al.*, "Precision Rosenbluth measurement of the proton elastic form-factors," *Phys.Rev.Lett.*, vol. 94, p. 142301, 2005.

[28] S. Boffi *et al.*, *Electromagnetic response of atomic nuclei*. Oxford Sciece Publications, 1996.

[29] A. Akhiezer and M. Rekalo, "Polarization phenomena in electron scattering by protons in the high energy region," *Sov.Phys.Dokl.*, vol. 13, p. 572, 1968.

[30] A. Akhiezer and M. Rekalo, "Polarization effects in the scattering of leptons by hadrons," *Sov.J.Part.Nucl.*, vol. 4, p. 277, 1974.

[31] O. Gayou *et al.*, "Measurement of G_{Ep}/G_{Mp} in $\vec{e}p \rightarrow e\vec{p}$ to $Q^2 = 5.6\,\text{GeV}^2$," *Phys.Rev.Lett.*, vol. 88, p. 092301, 2002.

[32] V. Punjabi *et al.*, "Proton elastic form-factor ratios to $Q^2 = 3.5\,\text{GeV2}$ by polarization transfer," *Phys.Rev.*, vol. C71, p. 055202, 2005.

[33] J. Arrington, "How well do we know the electromagnetic form-factors of the proton?," *Phys.Rev.*, vol. C68, p. 034325, 2003.

[34] P. A. M. Guichon and M. Vanderhaeghen, "How to reconcile the Rosenbluth and the polarization transfer method in the measurement of the proton form factors," *Phys. Rev. Lett.*, vol. 91, p. 142303, 2003.

[35] A. V. Afanasev *et al.*, "The Two-photon exchange contribution to elastic electron-nucleon scattering at large momentum transfer," *Phys.Rev.*, vol. D72, p. 013008, 2005.

[36] P. Blunden *et al.*, "Two-photon exchange in elastic electron-nucleon scattering," *Phys.Rev.*, vol. C72, p. 034612, 2005.

[37] C. E. Carlson and M. Vanderhaeghen, "Two-Photon Physics in Hadronic Processes," *Ann.Rev.Nucl.Part.Sci.*, vol. 57, pp. 171–204, 2007.

[38] N. Kivel and M. Vanderhaeghen, "Two-photon exchange in elastic electron-proton scattering: QCD factorization approach," *Phys.Rev.Lett.*, vol. 103, p. 092004, 2009.

155

[39] E. Tomasi-Gustafsson and G. I. Gakh, "Search for evidence of two photon contribution in elastic electron proton data," *Phys.Rev.*, vol. C72, p. 015209, 2005.

[40] A. Zichichi *et al.*, "Proton anti-proton annihilation into electrons, muons and vector bosons," *Nuovo Cim.*, vol. 24, pp. 170–180, 1962.

[41] M. P. Rekalo *et al.*, "Search for evidence of two photon exchange in new experimental high momentum transfer data on electron deuteron elastic scattering," *Phys.Rev.*, vol. C60, p. 042202, 1999.

[42] S. M. Bilenky *et al.*, "The Process $\bar{p}p \to e^-e^+$ with polarized initial particles and proton form-factors in timelike region," *Z.Phys.*, vol. C59, pp. 475–480, 1993.

[43] G. I. Gakh and E. Tomasi-Gustafsson, "Polarization effects in the reaction anti-p + p → e+ + e- in presence of two-photon exchange," *Nucl.Phys.*, vol. A761, pp. 120–131, 2005.

[44] G. I. Gakh and E. Tomasi-Gustafsson, "General analysis of polarization phenomena in $e^+ + e^- \to N + \bar{N}$ for axial parametrization of two-photon exchange," *Nucl.Phys.*, vol. A771, pp. 169–183, 2006.

[45] E. Tomasi-Gustafsson and M. P. Rekalo, "Search for evidence of asymptotic regime of nucleon electromagnetic form-factors from a compared analysis in space- and time-like regions," *Phys.Lett.*, vol. B504, pp. 291–295, 2001.

[46] D. V. Shirkov and I. L. Solovtsov, "Analytic model for the QCD running coupling with universal $\bar{\alpha}_s(0)$ value," *Phys.Rev.Lett.*, vol. 79, pp. 1209–1212, 1997.

[47] R. Baldini *et al.*, "A description of the ratio between electric and magnetic proton form factors by using space-like, time-like data and dispersion relations," *Nucl.Phys.Proc.Suppl.*, vol. 162, pp. 46–52, 2006.

[48] E. Eisenhandler *et al.*, "Measurement of Differential Cross-Sections for anti-Proton-Proton Annihilation Into Charged Pion and Kaon Pairs Between 0.79 GeV/c and 2.43 GeV/c," *Nucl.Phys.*, vol. B96, p. 109, 1975.

[49] A. Berglund *et al.*, "A Study of the Reaction $\bar{p}p \to \pi^-\pi^+$ at 10 GeV/c," *Nucl.Phys.*, vol. B137, pp. 276–282, 1978.

[50] T. Buran *et al.*, "Anti-Proton-Proton Annihilation Into $\pi^+\pi^-$ and K^+K^- at 6.2 GeV/c," *Nucl.Phys.*, vol. B116, p. 51, 1976.

[51] E. Barberio, B. van Eijk, and Z. Was, "PHOTOS: A Universal Monte Carlo for QED radiative corrections in decays," *Comput.Phys.Commun.*, vol. 66, pp. 115–128, 1991.

[52] C. Baglin *et al.*, "Measurement of the $\pi^0\pi^0$ cross-section in $\bar{p}p$ annihilations at $\sqrt{s} = 3\,\text{GeV}$," *Nucl.Phys.*, vol. B368, pp. 175–189, 1992.

[53] R. S. Dulude *et al.*, "Measurement of $\bar{p}p \to \pi^0\pi^0$, $\pi^0\eta^0$ in the T and U-meson region," *Phys.Lett.*, vol. B79, p. 329, 1978.

[54] T. Armstrong *et al.*, "Two-body neutral final states produced in $\bar{p}p$ annihilations at $2.911\,\text{GeV} \leq \sqrt{s} \leq 3.686\,\text{GeV}$," *Phys.Rev.*, vol. D56, pp. 2509–2531, 1997.

[55] V. A. Matveev *et al.*, "Automodellism in the large-angle elastic scattering and structure of hadrons," *Lett.Nuovo Cim.*, vol. 7, pp. 719–723, 1973.

[56] S. J. Brodsky and G. R. Farrar, "Scaling Laws at Large Transverse Momentum," *Phys.Rev.Lett.*, vol. 31, pp. 1153–1156, 1973.

[57] J. F. Gunion *et al.*, "Large Angle Scattering and the Interchange Force," *Phys.Rev.*, vol. D8, p. 287, 1973.

[58] L. Frankfurt *et al.*, "Hard exclusive pseudoscalar meson electroproduction and spin structure of a nucleon," *Phys.Rev.*, vol. D60, p. 014010, 1999.

[59] B. Pire *et al.*, "πn transition distribution amplitudes: their symmetries and constraints from chiral dynamics," *ArXiv Physics e-prints*, June 2011. arXiv:1106.1851v1 [hep-ph].

[60] B. Pire, K. Semenov-Tian-Shansky, and L. Szymanowski, "πN transition distribution amplitudes: Their symmetries and constraints from chiral dynamics," *Phys. Rev.*, vol. D84, p. 074014, 2011.

[61] B. Pire, K. Semenov-Tian-Shansky, and L. Szymanowski, "Cross section and single transverse target spin asymmetry for backward pion electroproduction," *ArXiv Physics e-prints*, 2012. arXiv:1201.0123 [hep-ph].

[62] J. P. Lansberg *et al.*, "Production of a pion in association with a high-Q^2 dilepton pair in antiproton-proton annihilation at GSI- FAIR," *Phys. Rev.*, vol. D76, p. 111502, 2007.

[63] V. Chernyak and A. Zhitnitsky, "Asymptotic Behavior of Exclusive Processes in QCD," *Phys.Rept.*, vol. 112, p. 173, 1984.

[64] I. D. King and C. T. Sachrajda, "Nucleon Wave Functions and QCD Sum Rules," *Nucl.Phys.*, vol. B279, p. 785, 1987. Revised version.

[65] "Wissenschafliche zielsetzungen und forschungsprogramme," 2005. FAIR Project, Gesellschaft für Schwerionen (GSI), Darmstadt.

[66] www-panda.gsi.de.

[67] H. Orth, "Status of targets for $\overline{P}$ANDA." XXVIII $\overline{P}$ANDA Collaboration Meeting, GSI Darmstadt, March 2009.

[68] M. Büscher et al., "The Moscow-Jülich Frozen-Pellet Target," in *Hadron Spectroscopy* (A. Reis, C. Göbel, J. D. S. Borges, and J. Magnin, eds.), vol. 814 of *American Institute of Physics Conference Series*, pp. 614–620, Feb. 2006.

[69] C. Ekstroem et al., "Hydrogen pellet targets for circulating particle beams," *Nucl. Instrum. Meth.*, vol. A371, pp. 572–574, 1996.

[70] A. Sánchez-Lorente, *Feasibility study of performing high precision gamma spectroscopy of ΛΛ hypernuclei in the PANDA experiment*. PhD thesis, Institut für Kernphysik, Johannes Gutenberg Universität, Mainz, 2010.

[71] P. Collaboration et al., "Technical Design Report for the: PANDA Straw Tube Tracker," tech. rep., PANDA Collaboration, 2012.

[72] H. Staengle et al., "Test of a large scale prototype of the dirc, a cherenkov imaging detector based on total internal reflection for babar at pep-ii," *Nucl. Instrum. Meth.*, vol. A397, pp. 261–282, 1997.

[73] K. Mengel et al., "Detection of monochromatic photons betwen 50 mev and 790 mev with a pbwo$_4$ scintillator array," *IEEE Trans. Nucl. Sci.*, vol. 45, pp. 681–685, 1998.

[74] R. Novotny et al., "Electromagnetic calorimetry with pbwo$_4$ in the energy regime below 1 gev," *IEEE Trans. Nucl. Sci.*, vol. 47, pp. 1499–1502, 2000.

[75] M. Hoek et al., "Charged particle response of pbwo$_4$," *Nucl. Instrum. Meth.*, vol. A486, pp. 136–140, 2002.

[76] "Technical proposal." CERN/LHC 9.71.

[77] "Technical proposal," 1994. CERN/LHCC 94-38, LHCC/P1.

[78] E.Auffray et al. in *Proceedings of SCINT99*, (Moscow), 1999.

[79] P. Collaboration et al., "Technical Design Report for PANDA Electromagnetic Calorimeter (EMC)," tech. rep., PANDA Collaboration, 2008.

[80] P. Abbon *et al.*, "The COMPASS Experiment at CERN," *Nucl. Instrum. Meth.*, vol. A577, pp. 455–518, 2007.

[81] N. Akopov *et al.*, "The HERMES dual-radiator ring imaging Cherenkov detector," *Nucl.Instrum.Meth.*, vol. A479, pp. 511–530, 2002.

[82] P. Abbon, M. Alexeev, H. Angerer, G. Baum, R. Birsa, *et al.*, "The experience of building and operating COMPASS RICH-1," *Nucl.Instrum.Meth.*, vol. A639, pp. 15–19, 2011.

[83] G. Atoyan *et al.*, "Lead-scintillator electromagnetic calorimeter with wavelength shifting fiber readout," *Nucl.Instrum.Meth.*, vol. A320, no. 1-2, pp. 144 – 154, 1992.

[84] G. David *et al.*, "Performance of the phenix em calorimeter," tech. rep., PHENIX Tech. Note 236, 1996.

[85] A. Golutvin, "Electromagnetic calorimeter for hera-b," 1994. HERA-B Tech. Note 94-073.

[86] "Lhcb technical proposal cern lhcc 98-4, lhcc/p4," 1998.

[87] I.-H. Chiang *et al.*, "Kopio - a search for $k^0 \rightarrow \pi^0 \nu\nu$," 1999. KOPIO Proposal.

[88] H. Morii, "Kopio experiment," 2004. Talk at NP04 Workshop at J-PARC.

[89] G. Atoyan *et al.*, "Test beam study of the kopio shashlyk calorimeter prototype," in *Proceedings of "CALOR 2004"*, May 2004.

[90] D. Lange, "The EvtGen particle decay simulation package," *Nucl.Instrum.Meth.*, vol. A462, pp. 152–155, 2001.

[91] J. Allison *et al.*, "Geant4 developments and applications," *IEEE Transactions on Nuclear Science*, vol. 53, p. 270, 2006.

[92] S. Agostinelli *et al.*, "Geant4: A simulation toolkit," *Nucl. Instrum. Meth.*, vol. A506, pp. 250–303, 2003.

[93] W. Erni *et al.*, "Technical design report for the panda electromagnetic calorimeter," tech. rep., PANDA Collaboration, 2008.

[94] D. Brown, E. Charles, and D. Roberts, "The babar track fitting algorithm, proc. computing in high energy physics conference," in *Proc. Computing in High Energy Physics Conference*, (Padova), 2000.

[95] B. Aubert *et al.*, "The babar detector," *Nucl. Instrum. Meth.*, vol. A479, pp. 1–116, 2002.

[96] P. Strother, *Design and application of the reconstruction software for the BaBar calorimeter*. PhD thesis, University of London and Imperial College, UK, 1998.

[97] von F. and Zernike, "Beugungstheorie des schneidenver-fahrens und seiner verbesserten form, der phasenkontrastmethode," *Physica*, vol. 1, no. 7-12, pp. 689 – 704, 1934.

[98] B. Kopf, *Untersuchung der photoinduzierten Reaktionen $\gamma p \to p\pi^0\pi^0$ und $\gamma p \to p\pi^0\eta$ an einem Flüsig-Wasserstoff-Target*. PhD thesis, Fakultät Mathematik und Naturwissenschaften der Techsnichschen Universität Dresden, 2002.

[99] T. Würschig, "Implementation of a dedicated routing concept for the updated mvd model." $\overline{P}$ANDA Collaboration Meeting, GSI Darmstadt, December 2009.

[100] R. Sobie, "Study of the $\tau^- \to \pi^-\pi^+\pi^-\pi^0\nu\tau$ and $\tau^- \to \pi^-\pi^-\pi^+\eta\nu\tau$ decays using the BaBar detector," *Nucl. Phys. Proc. Suppl.*, vol. 169, pp. 44–49, 2007.

[101] B. Aubert *et al.*, "A Study of $e^+e^- \to p\bar{p}$ using initial state radiation with BABAR," *Phys.Rev.*, vol. D73, p. 012005, 2006.

[102] D. Marchand *et al.*, "Time-like observables: differential cross section and angular asymmetry." HAL:in2p3-00374971, IPNO-DR-08-03.

[103] F. Iachello *et al.*, "Semiphenomenological fits to nucleon electromagnetic form-factors," *Phys.Lett.*, vol. B43, pp. 191–196, 1973.

[104] E. L. Lomon, "Effect of recent R_p and R_n measurements on extended Gari-Krümpelmann model fits to nucleon electromagnetic form-factors," *Phys.Rev.*, vol. C66, p. 045501, 2002.

[105] E. Tomasi-Gustafsson *et al.*, "Nucleon electromagnetic form-factors and polarization observables in space-like and time-like regions," *Eur.Phys.J.*, vol. A24, pp. 419–430, 2005.

[106] A. Antonelli *et al.*, "The first measurement of the neutron electromagnetic form-factors in the timelike region," *Nucl.Phys.*, vol. B517, pp. 3–35, 1998.

[107] M. Ambrogiani *et al.*, "Measurements of the magnetic form factor of the proton in the timelike region at large momentum transfer," *Phys. Rev.*, vol. D60, p. 032002, 1999. [Phys.Rev.D60:032002,1999].

[108] B. Delcourt *et al.*, "Study of the reaction $e^+e^- \to p\bar{p}$ in the total energy range 1925 MeV - 2180 MeV," *Phys.Lett.*, vol. B86, p. 395, 1979.

[109] D. Bisello *et al.*, "A measurement of $e^+e^- \to \bar{p}p$ for $1975\,\text{MeV} \leq \sqrt{s} \leq 2250\,\text{MeV}$," *Nucl.Phys.*, vol. B224, p. 379, 1983.

[110] M. Ablikim *et al.*, "Measurement of the cross section for $e^+e^- \to p\bar{p}$ at center-of-mass energies from $2.0\,\text{GeV}$ to $3.07\,\text{GeV}$," *Phys. Lett.*, vol. B630, pp. 14–20, 2005.

[111] T. Pedlar *et al.*, "Precision measurements of the timelike electromagnetic form-factors of pion, kaon, and proton," *Phys.Rev.Lett.*, vol. 95, p. 261803, 2005.

[112] T. Ullrich and Z. Xu, "Treatment of Errors in Efficiency Calculations," *ArXiv Physics e-prints*, Jan. 2007. arXiv:physics/0701199v1 [physics.data-an].